UNIVERSITY OF OKLAHOMA

GRADUATE COLLEGE

ROLE OF UPPER-LEVEL WIND SHEAR ON THE STRUCTURE AND MAINTENANCE OF DERECHO-PRODUCING CONVECTIVE SYSTEMS

A Dissertation

SUBMITTED TO THE GRADUATE FACULTY

in partial fulfillment of the requirements for the

degree of

DOCTOR OF PHILOSOPHY

By

MICHAEL CHARLES CONIGLIO
Norman, Oklahoma
2004

Downloaded from SHAREOK. Persistent Handle URL: https://hdl.handle.net/11244/1231

UMI Number: 3270679

INFORMATION TO USERS

The quality of this reproduction is dependent upon the quality of the copy submitted. Broken or indistinct print, colored or poor quality illustrations and photographs, print bleed-through, substandard margins, and improper alignment can adversely affect reproduction.

In the unlikely event that the author did not send a complete manuscript and there are missing pages, these will be noted. Also, if unauthorized copyright material had to be removed, a note will indicate the deletion.

UMI®

UMI Microform 3270679

Copyright 2007 by ProQuest Information and Learning Company.

All rights reserved. This microform edition is protected against unauthorized copying under Title 17, United States Code.

ProQuest Information and Learning Company
300 North Zeeb Road
P.O. Box 1346
Ann Arbor, MI 48106-1346

© Copyright by MICHAEL CHARLES CONIGLIO 2004
All Rights Reserved.

ROLE OF UPPER-LEVEL WIND SHEAR ON THE STRUCTURE AND MAINTENANCE OF DERECHO-PRODUCING CONVECTIVE SYSTEMS

A Dissertation APPROVED FOR THE SCHOOL OF METEOROLOGY

BY

David J. Stensrud

Michael B. Richman

Alan Shapiro

Frederick H. Carr

Lance F. Bosart

Ramkumar N. Parthasarathy

ACKNOWLEDGEMENTS

I'm very fortunate that I've been able to work in the Norman community the last four years. In particular, it's been a great experience working at NSSL/SPC and I thank everyone for making it an environment so conducive to learning. I learned a lot from Bob Johns about forecasting and derechos. It's always worthwhile and fun talking to Bob about derechos and listening to his experiences as a forecaster. I thank Lou Wicker for guiding me through his code and for sharing his valuable thoughts and experiences. Victor Homar is very accommodating and helped me learn Vis5D very quickly. I may not have finished in the summer of 2004 without him! My spirits have been raised many times by the encouragement and kind words from Chuck Doswell. Finally, I thank Harold Brooks for chipping in with Dave Stensrud to fund my new computer so that I could finish on time!

I want to recognize the staff of the School of Meteorology (Celia, Marcia and Nancy). Celia was the first person I met when I first visited Oklahoma seven years ago and I couldn't have been introduced to OU by a better person.

The OU faculty and my committee members (Dave Stensrud, Mike Richman, Alan Shapiro, Fred Carr, Kumar Parthasarathy, and Lance Bosart of SUNY Albany) deserve recognition for being very accommodating. I've benefited greatly from their enthusiasm. I am especially grateful to Lance for his understanding and support of my transfer back to OU and for agreeing to remain on my committee. He always provides remarkably prompt and constructive criticism when asked. I appreciate how he's made me feel like I never left Albany.

I especially want to thank Dave for his support and guidance over the past seven years. I'm lucky to have had him as an adviser. On the professional side, his knowledge and skill has been invaluable. He's taught me how to be more concise, efficient and a better communicator without controlling my growth as a scientist. As a friend, Dave was very supportive during my father-in-law's passing a few years ago and during my unusual string of illnesses over the past year. He made sure I understood the importance of placing my work on the backburner during those difficult times and, for that, I'm very grateful.

I want to thank my family and friends for their many words of encouragement. I can't forget about my dog Frostie! She was wonderful at taking my stress away. I miss her very much.

Most of all, I want to thank my wife Melissa for all of her patience and support. It would take another dissertation to explain all the ways she has helped me get through the last several years. I'll sum it up by saying that she never let me forget the value of friendship and love. I love her dearly. I know her father is proud of us both.

CONTENTS

List of Tables vii

List of Figures viii

List of Acronyms xiv

List of Symbols xvi

Abstract xvii

1. Introduction 1
1.1 Motivation 1
1.2 Objectives 5

2. Background 7
2.1 Effects of thunderstorm downdrafts 7
2.1.1 Precipitation effects on downdrafts 8
2.2 Observed characteristics of organized convective systems 10
2.2.1 Conceptual models of MCSs 10
2.2.2 Characteristics of convectively-produced windstorms . 13
2.2.3 Characteristics of derechos 14
2.2.4 Derecho environments 17
2.3 Conceptual models 19
2.3.1 Squall line simulations in 2-D 19
2.3.2 Squall line simulations in 3-D 23
2.3.3 Density current models 26
2.4 Discrepancies between observations and idealized models 30
2.5 Summary 32

3. Data Set and Analysis of Large-Scale Environments 33
3.1 Derecho criteria 33
3.2 Analyzing large-scale environments 35
3.2.1 Analysis method 36
3.3 Results 38
3.3.1 Upstream trough pattern 40
3.3.2 Ridge pattern 43
3.3.3 Zonal pattern 46
3.4 Discussion 49

4. Analysis of Proximity Soundings 53
4.1 Identification of proximity soundings 54
4.1.1 Grouping the soundings by derecho lifecycle 55
4.1.2 Grouping the soundings by synoptic-scale forcing 56
4.2 Results 57

4.2.1 Lifecycle stratification 57
4.2.2 Forcing stratification 62
4.2.3 Comparison to simulations 66
4.3 Discussion 69

5. Numerical Simulations **70**
5.1 Numerical model 70
5.2 Configuration of the 2-D dry simulations 72
5.2.1 Trajectory calculations 74
5.3 Configuration of the 2-D and 3-D simulations 76
5.4 Results 81
5.4.1 2-D dry simulations 81
5.4.1.1 Parcel Analyses 88
5.4.2 2-D moist simulations 95
5.4.3 3-D simulations 106
5.4.3.1 System maintenance 107
5.4.3.2 System size 117
5.4.3.3 System structure 121
5.5 Discussion 123
5.6 Application of results 125

6. Summary and Discussion **128**
6.1 Summary and discussion of observational analysis 129
6.2 Summary and discussion of numerical simulations 131

References 135

Appendix 146

LIST OF TABLES

Table 2.1. Criteria used to identify derecho events in JH87 15

Table 4.1. Mean 0-1-, 0-2.5-, 0-5-, and 5-10-km shear vector magnitudes (m s^{-1}) for the lifecycle stratification (beginning, mature, decay) and the forcing stratification (strong, moderate, weak). Shaded cells in the lifecycle stratification indicate that the sample mean is statistically different than the sample mean for the decay soundings at the 95% confidence level. Shaded cells in the forcing stratification indicate that the sample mean is statistically different than the sample mean for the weak-forcing soundings at the 95% confidence level 58

LIST OF FIGURES

Fig. 2.1. Conceptual model of a squall line viewed in a vertical cross section in a plane parallel to its motion (from Houze et al. 1989) 11

Fig. 2.2. The classic conceptual model of the evolution of a bow echo from a linear echo, to a bow echo, into a comma echo with a cyclonically rotating head. This model recognizes the possibility for tornadoes along the cyclonic shear side of the downburst (from Fujita 1978) 13

Fig. 2.3. Left panel: An idealized sketch of the warm season midlatitude synoptic scale pattern associated with especially long-lived progressive derechos. The line B-M-E represents the beginning, middle, and end points of the derecho. The thin lines depict the sea-level pressure field in the vicinity of quasi-stationary frontal boundary. Broad arrows denote the low-level jet (LJ) and the upper-tropospheric polar jet (PJ). Right panel: Idealized sketch of a midlatitude synoptic situation favorable for the development of serial derechos (the "dynamic" pattern). The upper-tropospheric subtropical jet is labeled SJ (from Johns 1993) 18

Fig. 2.4. Four stages in the development of an idealized bow echo developing in a strongly sheared, large-CAPE environment. The updraft current is denoted by the thick double lines, with the rear-inflow current in (c) and (d) denoted by the thick, dashed vector. The shading denotes the surface cold pool. The thin, circular arrows depict the most significant sources of horizontal vorticity, which is either baroclinically generated by the cold pool or is inherent in the ambient shear. Regions of heavier rainfall are indicated by the more sparsely or densely packed vertical lines, respectively. The scalloped line denotes the outline of the cloud (from W93) 24

Fig. 2.5. Solutions from the hydrodynamical model of Shapiro (1992). The profiles in the upper-most panels represent changes in the magnitude of the wind (m s^{-1}) with height in a reference frame fixed with the density current barrier (shaded in black in the middle panels). Values of the streamfunction and the direction of the flow also is shown in the middle panels and the lower panels show vertical velocity (every 2 m s^{-1}) (adapted from Shapiro 1992)..... 27

Fig. 3.1. The yearly distribution of derechos in the data set 35

Fig. 3.2. (a) The mean 500-mb geopotential height (ϕ, contours every 60 m) and wind (flag = 25 m s^{-1}, full barb = 5 m s^{-1}) for four clusters within the upstream-trough pattern. (b) As in (a), except for the 850-mb temperature (T, solid contours every 2 K) and specific humidity (q, dashed contours every 1 g kg^{-1} starting at 8 g kg^{-1}). (c) As in (a), except for the 250-mb wind speed (|V|, solid contours every 5 m s^{-1}, starting at 25 m s^{-1}) and divergence of the wind (Div (V), dashed contours every 0.25 x 10^{-5} s^{-1}). The horizontal and vertical dimension of each grid is 2600 km by 2400 km, respectively. The **X** denotes the position of the DCS at the analysis time. The number in the upper-right corner of each grid denotes the number of analyses in each composite
(cluster)..... 39

Fig. 3.3. The total number of derecho major axes that occur in 200 km by 200 km squares for (a) the 91 cases in the upstream-trough pattern, (b) the 46 cases in the ridge pattern, and (c) the 28 cases in the zonal pattern. Contours are drawn every 3 events in (a), every 2 events in (b), and every 1 event in (c) 41

Fig. 3.4. The total number of derechos occurring during each month for each of the three main patterns. The counts are given in the table below the figure..... 42

Fig. 3.5. As in Fig. 3.2, except for the ridge pattern..... 44

Fig. 3.6. As in Fig. 3.2, except for the zonal pattern 47

Fig. 3.7. The 500-mb geopotential height and wind (as in Fig. 6) for the 8 cases that comprise cluster 1 in the upstream-trough pattern. The **X** denotes the approximate location of the DCS at the analysis time and the arrow depicts the approximate track of the derecho major axis. The date and time (UTC) of each analysis (in YYMMDDHH format) is displayed in the lower right of each panel 48

Fig. 3.8. Examples of 500-mb geopotential heights and winds from hybrid patterns. (a) An example of an upstream-trough/zonal pattern hybrid. (b) An example of an upstream-trough/ridge pattern hybrid. (c) An example of an unclassifiable hybrid pattern. The approximate track of the derecho major axis is depicted by the arrow. The date and time (UTC) of each analysis (in YYMMDDHH format) is displayed in the lower right of each panel. 50

Fig. 3.9. Histograms of the (a) 500-hPa height near the location of derecho initiation, (b) the direction of propagation of the derecho, and (c) the 500-hPa wind speed near the location of derecho initiation, as determined from the Reanalysis data, for the cases that comprise the three main patterns and the 60 cases that are not classified into these main patterns (others)..... 51

Fig. 4.1. The distribution of the mean 500-mb Q-vector divergence (scaled by 10^{16} kPa m^{-2} s^{-1}) versus day associated with the 91 beginning and mature proximity soundings. The thresholds for defining the forcing stratification are shown by the dashed lines 57

Fig. 4.2. The cumulative frequency distribution of CAPE (J kg^{-1}) for the beginning, mature, and decay soundings. The sample means for the beginning ($\bar{x}_B$), mature ($\bar{x}_M$), and the decay ($\bar{x}_D$) soundings, and their 95% confidence intervals (in parentheses), are shown in the upper left corner. $\bar{x}_D$ is significantly different than both $\bar{x}_M$ and $\bar{x}_B$ at the 95% confidence level..... 58

Fig. 4.3. Vertical profiles of (a) median RH and (b) θ_e for the beginning, mature, and decay sondings. The beginning and mature RH profiles are statistically different at the 95% confidence level between 0.75 and 3 km. There are no statistically significant differences in the θ_e profiles..... 59

Fig. 4.4. Mean hodographs for the beginning, mature, and decay soundings. Prior to averaging, the wind components (u,v) in each sounding are represented in a coordinate system with the tip of the mean MCS motion vector (u_s,v_s) at the origin. The mean winds are calculated every 0.5 km above ground level (AGL), are plotted every 1 km AGL, and are labeled every 3 km AGL. Mean shear values related to the mean hodographs are given in Table 4.1 61

Fig. 4.5. The cumulative frequency distribution of CAPE (J kg^{-1}) for the strong, moderate, and weak-forcing soundings. The sample means for the strong ($\bar{x}_S$), moderate ($\bar{x}_{MD}$), and the weak ($\bar{x}_W$) forcing soundings, and their 95% confidence intervals (in parentheses), are in the upper left corner. $\bar{x}_S$ is significantly different than both $\bar{x}_{MD}$ and $\bar{x}_W$ at the 95% confidence level..... 63

Fig. 4.6. As in Fig. 4.3, except for the strong, moderate, and weak forcing soundings. The strong and weak forcing profiles are statistically different at the 95% confidence level between the surface and 1.25 km. The strong forcing θ_e profile is significantly different from the moderate and weak forcing θ_e profiles at the 95% confidence level at all vertical levels (0-6 km) 64

Fig. 4.7. As in Fig. 4.4, except for the strong, moderate, and weak forcing soundings. Mean shear values are given in Table 4.1 65

Fig. 4.8. Scatterplots of (a) 0-2.5 km, (b) 0-5 km, and (c) 5-10 km shear vector magnitudes (m s^{-1}) versus CAPE (J kg^{-1}) for those soundings in which the convective structure of the DCS is identified (see legend at top of figure). Results from Weisman's (1993) numerical simulations of convective systems also are shown in (a) and (b) (see his Fig. 24). The letters represent the convective structure of the simulated systems as defined by Weisman (1993) (see text for details) 68

Fig. 5.1. Initial U profiles for the 2-D dry simulations..... 74

Fig. 5.2. Initial sounding used in the 2-D moist simulations 76

Fig. 5.3. Initial U profiles used for the moist simulations. The values of bulk shear in all the profiles (listed on the figure) correspond to the median values derived from the set of weakly forced soundings. The profile that contains the values of shear closest to the median shear in the observations contains 20 m s^{-1} of 0-5 km shear and 15 m s^{-1} of 5-10 km shear 77

Fig. 5.4. The initial sounding used in the 3-D simulations (thick lines) compared to the Weisman and Klemp (1982) sounding (thin lines). The values of CAPE, lifting condensation level (LCL) and the maximum difference in θ_e between low and mid levels ($\Delta\theta_e$) in the profiles (listed on the figure) correspond approximately to the median values derived from the weakly forced soundings (see text for details) 78

Fig. 5.5. The evolution of the gust front speed for the simulations with 0, 10, 20, and 30 m s^{-1} of shear in the 5-10 km layer 81

Fig. 5.6. The evolution of the density-current-head height for the 0, 10, 20, and 30 m s^{-1} shear simulations. The head height is estimated by finding the maximum height of the -1.0 K isotherm behind the gust front 82

Fig. 5.7. The evolution of the maximum vertical velocity for the simulations with 0, 10, 20, and 30 m s^{-1} of shear in the 5-10 km layer 83

Fig. 5.8. Time-mean (1.0-1.5 h) values of perturbation potential temperature (contours every 0.5 K starting at -0.25 K), vertical motion (contours every 2 m s^{-1} starting at 2 m s^{-1}) and perturbation pressure (contours every 0.1 h Pa with negative contours dashed) for the case with no upper-level shear. Only a 20 km by 12 km portion of the domain is shown with the gust front centered at 15 km 84

Fig. 5.9. As in Fig. 5.8, but for the case with 10 m s^{-1} of upper-level shear with regions of relative high (H) and low (L) pressure noted 86

Fig. 5.10. As in Fig. 5.8, but for the case with 20 m s^{-1} of upper-level shear 87

Fig. 5.11. The distribution of the maximum displacement of low-level (0-2 km) parcels (m) for various values of 5-10 km shear. Thin solid lines enclose the maximum and minimum values among the 21 trajectories, thin dashed lines enclose the 25th and 75th percentiles, and the thick solid line is the median 89

Fig. 5.12. The median of the maximum displacements of air parcels among the 21 trajectory calculations that begin in the 0-1 km layer for various values of 5-10 km shear..... 89

Fig. 5.13. The median of the maximum displacements of air parcels among the 21 trajectory calculations that begin in the 1-2 km layer for various values of 5-10 km shear..... 90

Fig. 5.14. Illustration of parcel paths in the lowest 2 km starting at 2100 s (thick solid lines) for the (a) 0 m s^{-1}, (b) 10 m s^{-1} and (c) 20 m s^{-1} shear cases. The parcel paths end at 4200 s in (a), 4500 s in (b) and at 5400 s in (c). The perturbation potential temperature (dashed lines, contoured as in Fig. 5.8) and vertical motion (thick grey lines, contoured as in Fig. 5.8) also is shown at these times 91

Fig. 5.15. Vertical motion (m s^{-1}) along the parcel paths for parcels starting at (a) 375 m and (b) 1625 m among the 0, 10, 20 and 30 m s^{-1} shear cases. The values are only calculated up until the point the parcel leaves the region of forced upward motion 92

Fig. 5.16. The evolution of the maximum vertical velocity for the 0, 15, and 30 m s^{-1} 2-D moist simulations 95

Fig. 5.17. The evolution of the domain-integrated rainwater for the 0, 15, and 30 m s^{-1} 2-D moist simulations 96

Fig. 5.18. The evolution of the minimum buoyancy acceleration (m s^{-2}) for the 0, 15, and 30 m s^{-1} 2-D moist simulations 97

Fig. 5.19. The evolution of the domain-integrated rainwater for the 0, 15, and 30 m s^{-1} 2-D moist simulations 98

Fig. 5.20. Time-mean (2-3 h) values of negative buoyancy (contours every 0.03 m s^{-2} starting at -0.02 m s^{-2}), upward vertical motion (contours every 1 m s^{-1} starting at 2 m s^{-1}) and rainwater mixing ratio (contours every 0.5 g kg^{-1} starting at 1 g kg^{-1}) for the case with no shear in the 5-10 km layer. Only a 50 km by 12 km portion of the domain is shown with the gust front centered at 40 km 99

Fig. 5.21. As in Fig. 5.20 but averaged for the period of 4-5 h 100

Fig. 5.22. As in Fig. 5.20 but for the case with 15 m s^{-1} of 5-10 km shear 101

Fig. 5.23. As in Fig. 5.20 but for the case with 15 m s^{-1} of 5-10 km shear averaged in the 4-5 h period 102

Fig. 5.24. Perturbation pressure (contours every 0.4 h Pa with negative values dashed) and gust-front relative winds in a 40 km cross section through the gust front averaged from (a) 2-3 h and (b) 4-5 h for the case with no shear aloft 104

Fig. 5.25. As in Fig. 5.24 but for the case with 15 m s^{-1} of 5-10 km shear 105

Fig. 5.26. Evolution of the maximum surface (125 m) wind for the 3-D simulations 108

Fig. 5.27. Evolution of the maximum vertical velocity for the 3-D simulations 109

Fig. 5.28. Evolution of the minimum vertical velocity for the 3-D simulations 109

Fig. 5.29. Evolution of the minimum buoyancy acceleration for the 3-D simulations 110

Fig. 5.30a-c. Evolution of the surface total precipitation mixing ratio (solid lines every 2 g kg^{-1} starting at 2 g kg^{-1}) that highlights the heaviest precipitation, the position of the gust front at the surface (dashed line) and the ground relative wind vectors (every 4 grid points) for a 60 km by 60 km portion of the domain at (a) 2 h, (b) 2.5 h, and (c) 3 h for the case with no upper-level shear (left panels) and the case with 15 m s^{-1} of upper-level shear (right panels) 111

Fig. 5.30 d-e (continued). Evolution of the surface total precipitation mixing ratio (solid lines every 2 g kg^{-1} starting at 2 g kg^{-1}) that highlights the heaviest precipitation, the position of the gust front at the surface (dashed line) and the ground relative wind vectors (every 4 grid points) for a 60 km by 60 km portion of the domain at (d) 3.5 h and (e) 4 h for the case with no upper-level shear (left panels) and the case with 15 m s^{-1} of upper-level shear (right panels) 112

Fig. 5.31. Evolution of the gust front speed for the three simulations 114

Fig. 5.32. The storm-relative wind profiles for the three simulations at 3.5 h 114

Fig. 5.33. Vertical cross sections taken along the center portion of the cold pool that trigger convections for the case with no upper level shear (top panel), the case with 15 m s^{-1} of upper-level shear (middle panel) and the case with 30 m s^{-1} of upper-level shear (bottom panel). Instantaneous values of negative buoyancy (dashed lines every 0.06 m s^{-2} starting at -0.02 m s^{-2}) and upward motion (grey solid lines every 2 m s^{-1} starting at 2 m s^{-1}) are shown at 4.33 h. The dark solid lines denote the 1 h paths of the trajectories starting at 3.33 h at the lowest 8 model levels (0-2 km). Trajectories are calculated with model output every 2 min 115

Fig. 5.34. Evolution of the domain-integrated rainwater for the 3-D simulations for the 0, 15 and 30 m s^{-1} simulations 116

Fig. 5.35. Horizontal cross sections of the total precipitation mixing ratio at 4 km AGL (solid lines contoured every 1 g kg^{-1} starting at 1 g kg^{-1}), the position of the gust front at the surface (dashed line), and the gust-front relative wind at 3 km AGL at every other grid point at (a) 3 h, (b) 4 h, (c) 5 h and (d) 6 h for the case with no upper-level shear. Only a 320 km by 320km portion of the domain is shown 118

Fig. 5.36. As in Fig. 5.35 but for the case with 15 m s^{-1} of 5-10 km shear 119

Fig. 5.37. As in Fig. 5.35 but for the case with 30 m s^{-1} of 5-10 km shear 120

Fig. 5.38. Evolution of the maximum surface winds for specialized simulations that vary the density of hail (r_h) from 400 kg m^{-3} to 900 kg m^{-3} and the slope-intercept parameter for hail (n_{x0}) from 4 x 10^6 m^{-4} to 4 x 10^4 m^{-4} for (a) an environment with no upper-level shear and (b) an environment with 20 m s^{-1} of upper-level shear 125

Fig. 6.1. Schematic diagram depicting the relative airflow and the evolution of the convective systems for the case with no upper-level shear (left column) and the case for 15 m s^{-1} of upper-level shear (right column) for the 1-2 h period (top row), the 2-3 h period (middle row), and the 3-4 h period (bottom row). The dashed line represents the cold pool and C_0 and C_{15} represent the cold pool motion for the no shear and 15 m s^{-1} shear cases, respectively. The darkness of the shading represents heavier precipitation rates 134

LIST OF ACRONYMS

2-D: Two-dimensional

3-D: Three-dimensional

BAMEX: Bow Echoes and Mesoscale Convective Vortex

CAPE: convective available potential energy

COMET: Cooperative Program for Operational Meteorology Education and Training

DCS: derecho-producing convective system

JH87: Johns and Hirt (1987)

LEWP: Line echo wave pattern

MCC: mesoscale convective complex

MCS: mesoscale convective system

MF: moderate forcing

NCAR: National Centers for Atmospheric Research

NCEP: National Centers for Environmental Prediction

NCDC: National Climatic Data Center

NCOMMAS: National Severe Storms Laboratory Collaborative Model for Multiscale Atmospheric Simulation

RH: relative humidity

RHS: right hand side

RIJ: Rear inflow jet

RIN: Rear inflow notch

RKW: Rotunno et al. (1988)

SF: strong forcing

SPC: Storm Prediction Center

W93: Weisman (1993)

WF: weak forcing

WR: Weisman and Rotunno (2004)

WSR-88D: Weather Surveillance Radar

LIST OF SYMBOLS

A	maximum cooling rate (K s^{-1}) in cooling function
B	buoyancy acceleration (m s^{-2})
C	vertically integrated buoyancy (m^2 s^{-2})
g	gravity acceleration (m s^{-2})
λ_0	density of hail (kg m^{-3})
n_{x0}	slope intercept for the distribution of hail (m^{-4})
p	pressure (kg m^{-1} s^{-2})
Q	Q-vector (kPa m^{-2})
r	radius of cooling (m) in cooling function
$\vec{r}$	position vector (m)
r_h	density of hail (kg m^{-3})
r_m	total hydrometeor mixing ratio (kg kg^{-1})
r_v	water vapor mixing ratio (kg kg^{-1})
ρ	dry air density (kg m^{-3})
ρ_m	moist air density (kg m^{-3})
ϕ	500–h Pa geopotential height (m)
t	time (s)
t_{obs}	normalized observation time (unitless)
T	temperature (K)
θ	potential temperature (K)
θ_e	equivalent potential temperature (K)
u	velocity component (m s^{-1}) along x-axis
u_s	velocity component (m s^{-1}) along direction of MCS motion
v	velocity component (m s^{-1}) along y-axis
$\vec{V}$	velocity vector (m s^{-1})
w	vertical velocity (m s^{-1})
$\mathbf{X}$	correlation matrix
x_c	x-component of the center of the cooling function (km)
z_c	z-component of the center of the cooling function (km)
x_r	cooling function radius in the x-direction (m)
z_r	cooling function radius in the z-direction (m)
$\bar{x}_B$	mean CAPE for the beginning soundings (m^2 s^{-2})
$\bar{x}_D$	mean CAPE for the decay soundings (m^2 s^{-2})
$\bar{x}_M$	mean CAPE for the mature soundings (m^2 s^{-2})
$\bar{x}_{MD}$	mean CAPE for the moderate forcing soundings (m^2 s^{-2})
$\bar{x}_S$	mean CAPE for the strong forcing soundings (m^2 s^{-2})
$\bar{x}_W$	mean CAPE for the weak forcing soundings (m^2 s^{-2})
z	height (m)

ABSTRACT

Common large-scale environments associated with the development of derecho-producing convective systems from a large number of events are identified using statistical clustering of the 500-mb geopotential heights as guidance. The majority of the events (72%) fall into three main patterns that include a well-defined upstream trough (40%), a ridge (20%), and a zonal, low-amplitude flow (12%), which is defined as an additional warm-season pattern that is not identified in past studies of derecho environments. Consequently, forecasters need to be aware that the environmental large-scale patterns idealized in past studies only depict a portion of the full spectrum of the possibilities associated with the development of derechos.

To further explore derecho environments, statistics of derecho proximity-sounding parameters are presented relative to the derecho lifecycle as well as relative to the forcing for upward motion for the benefit of forecasters who use ingredients-based techniques. It is found that the environments ahead of maturing derechos tend to moisten at low-levels while remaining relatively dry aloft. In addition, derechos tend to decay as they move into environments with less instability and smaller deep-layer shear. Low-level shear (instability) is found to be significantly higher (lower) for the more strongly forced events, while the low-level storm relative inflow tends to be much deeper for the more weakly forced events. Furthermore, discrepancies are found in both low-level and deep-tropospheric shear parameters between observations and the shear profiles considered favorable for strong, long-lived convective systems in idealized simulations.

To explore the role of upper-level shear in derecho environments, a set of two-dimensional simulations of density currents within a dry, neutrally stable environment are

used to examine the ability of a cold pool to lift environmental air within a vertically sheared flow. The results confirm that the addition of upper-level shear to a wind profile with weak to moderate low-level shear increases the vertical displacement of low-level parcels despite a decrease in the vertical velocity along the cold pool interface, as suggested by previous studies. Parcels that are elevated above the surface (1-2 km) overturn and are responsible for the deep lifting in the deep-shear environments. This deep overturning caused by the upper-level shear helps to maintain the tilt of the convective systems in more complex two-dimensional and three dimensional simulations. The overturning also is shown to greatly increase the size of the convective systems in the three-dimensional simulations by facilitating the initiation and maintenance of convective cells along the cold pool. When combined with estimates of the cold pool motion and the storm-relative hodograph, these results may best be used for the prediction of the demise of strong, linear mesoscale convective systems (MCSs) and may provide a conceptual model for the persistence of strong MCSs above a surface nocturnal inversion in situations that are not forced by a low-level jet.

Chapter 1: Introduction

Convective storms can produce a variety of hazardous weather. While tornadoes and flash floods are usually responsible for the majority of casualties, fatalities, and economic losses every year, damaging nontornadic wind gusts can also contribute significantly to these losses (Kunkel et al. 1999). This study examines a particularly important subset of severe convective windstorms known as derechos (pronounced day-ray'-chos)[1], which are thought to account for much of the damage owing to nontornadic convective winds (often called "straight-line" winds) (Wakimoto 2001).

According to their definition by Johns and Hirt (1987; hereafter JH87), derechos emanate from a variety of convective structures, including those that are classified as circular mesoscale convective complexes (MCCs, Maddox 1980), general mesoscale convective systems (MCSs, Zipser 1982) or as more elongated linear systems that are grouped into the rather broad category of squall lines (Parker and Johnson 2000). Although they occur most frequently during the summer months across the Midwestern U.S., derechos have been observed during all months of the year and in most locales east of the Rocky Mountains (JH87, Bentley and Mote 1998, Coniglio and Stensrud 2004).

1.1. Motivation

The identification of radar-reflectivity patterns associated with severe-wind producing convection (Fujita 1959, Nolan 1959, Hamilton 1970, Fujita 1978, Johns and Doswell 1992, Przybylinski 1995, Miller and Johns 2000) has greatly assisted forecasters in

[1] The term derecho was originally termed by Hinrichs (1888) with the intent of distinguishing wind damage produced by ordinary thunderstorm winds from those produced by tornadoes.

warning the public on the potential for damaging winds over the last few decades. However, at greater lead times (> 3 h), derechos remain a challenging forecast problem.

An important part of the forecast process involves the identification of important aspects of the environment that gives birth to and sustains the convective phenomenon in question. As detailed in Chapter 2, much of our current knowledge on derecho environments stems from the study of JH87, whose work was restricted to warm-season events. Illustrations of the large-scale flow patterns associated with derechos are even more limited and are related mostly to the severe, long-track variety (Johns et al. 1990 examine 14 such cases, which are idealized into two patterns in Johns 1993). Evans and Doswell (2001) extend the work on derecho environments by examining proximity soundings from 67 derechos from all times of the year. However, they focus their attention on the cold pool and low-level shear/storm-relative wind characteristics and do not present features of the hodographs or of the vertical distribution of moisture in the profiles. They also suggest that additional patterns to those discussed in Johns (1993) exist, but do not expand upon the structure or frequency of these patterns.

Another important part of the forecast process involves an understanding of the physical connection between the observed environments and the resultant behavior of the convection; a problem which has led researchers to employ convection-resolving numerical models within a horizontally homogeneous environment. Despite the obvious restrictions of imposing and maintaining a horizontally uniform base state, studies of this nature have had some success in physically understanding how the storm responds to changes in the environment, particularly with supercell thunderstorms (Weisman and Klemp 1982, Rotunno and Klemp 1985, Brooks et al. 1994, Wicker 1996, Gilmore and

Wicker 1998).

A common characteristic of derecho-producing convective systems (DCSs) is that the most intense convection nearly always obtains a linear organization along the leading edge of the system, often as a single *bow echo* (Fujita 1978) or with smaller embedded bow echoes, during most of the DCS lifetime (JH87, Przybylinski 1995). In relation to linear MCSs in general, a large amount of idealized modeling work focuses on the interaction between the cold pool of air generated by the thunderstorm and the environmental low-level vertical wind shear (summarized in Chapter 2). The balance between the baroclinically-generated vorticity along the cold pool leading edge and the ambient low-level shear within the depth of the cold pool is deemed to be a primary factor controlling the linear MCSs in these numerical simulations. Weisman and Rotunno (2004) (WR hereafter) modify this original theory (Rotunno et al. 1988; RKW hereafter) by suggesting that shear above the depth of the cold pool can also be important in the same manner through action at a distance (Davies-Jones 2002) and the interaction with decaying rain cells, but shear above 5 km is detrimental to the overall strength and maintenance of the convective system.

Weisman (1992), Weisman (1993) (W93 hereafter) and WR apply the RKW concepts to understanding simulated convective systems that have features often observed with DCSs. W93 uses these simulations to identify favorable environmental wind shear parameters. It is shown that, for a convectively unstable and relatively moist troposphere, at least moderate low-level shear (> 15 m s^{-1} over the lowest 2.5 or 5 km) is needed in order for the model to produce structures that resemble observed DCSs. From one simulation with the shear layer extended up to 10 km, WR also conclude that these

structures are particularly favored if shear is confined to 2.5 km and is at least 20 m s^{-1} in magnitude, with no shear aloft, a result also supported by the recent simulations presented in Weisman and Trapp (2003).

In comparison, the study of observed derecho environments by JH87 suggests a *mean* value of surface-700 h Pa shear of around 15 m s^{-1} for the more weakly forced events. Evans and Doswell (2001) show that the majority of the distribution of low-level shear falls below the minimum shear required to produce long-lived bow echoes in the idealized simulations of W93. Therefore, while the past idealized simulations are able to reproduce many observed features of DCSs, the parameter space examined in the simulations of strong, long-lived convective systems appears to differ somewhat from the parameter space of observed DCSs. WR recently suggest that the 0-5 km shear in relation to the cold pool strength better corresponds to the strength and structure of the simulated convective systems, but the physical reasons for this modification are only briefly hypothesized.

It is recognized that many convective systems may be sustained by processes other than those contained in convection/idealized environment interactions (Fritsch and Forbes 2001). It is known that DCSs usually initiate in the vicinity of a low-level thermal boundary and near a maximum in low-level warm advection, which is often a main source of the vertical wind shear. Less is known about how the related background forcing for upward motion and/or circulation features affects the overall maintenance of the system. Additionally, gravity waves (Schmidt and Cotton 1990) and embedded convective-scale circulations (Bernardet and Cotton 1998) that interact with stable layers may play a primary role in some cases. A reasonably accurate, yet manageable set of

numerical simulations that represent these type of events would require some type of representation of the background forcing superimposed on the homogeneous environment (Crook and Moncrieff 1988) or from other designs (Schmidt and Cotton 1990, Coniglio and Stensrud 2001). While these types of events justifiably await future study, the current study focuses on events that are assumed to be well-represented by idealized numerical models; those that occur within relatively benign synoptic-scale forcing for upward motion within well-mixed boundary layers.

Motivated by the detailed observational analysis presented in Chapters 3 and 4, this study hypothesizes that it is possible to describe characteristics of convective system maintenance and structure in a context different than that given by W93 and WR. In particular, this study examines the hypotheses based in the work of Shapiro (1992), Moncrieff and Liu (1999) and Coniglio and Stensrud (2001) that upper-level shear is an important factor in the structure and maintenance of strong, long-lived convective systems.

1.2. Objectives

While the above-mentioned studies reveal many aspects of derecho environments, there has yet to be a comprehensive study documenting the spectrum of large-scale environmental flow patterns associated with derechos. Therefore, the first goal of this study is to examine this spectrum and to identify, if any, the preferred large-scale patterns from a large data set of derecho events from all times of the year. Emphasis is placed on more clearly defining and expanding on the patterns identified in past literature, primarily for the benefit of forecasters who often use pattern recognition techniques.

The second goal of this study is to examine derecho environments with the use of proximity soundings. As mentioned by Johns (1993), "there has not been a thorough investigation into the nature of hodographs associated with bow echo situations". This problem is only partially examined by Evans and Doswell (2001) since they concentrate on the associated low-level shear vector magnitudes and storm-relative wind speeds and do not provide any estimation of the observed convective structures. Therefore, the examination of DCS environments with the use of proximity soundings in this study will benefit ingredients-based forecasting techniques and provide an observational baseline for the numerical modeling experiments.

The third goal is to explain the importance of the wind shear above the cold pool (identified in the observational portion of this study) by producing a set of both two dimensional (2-D) and three-dimensional (3-D) numerical simulations. How these simulations compare to the observations and to past idealized simulations also will be documented.

This research is important because it is believed that the behavior of convective systems can be interpreted differently than what is presented in W93 and WR in light of the observational evidence[2]. Improved forecasting methods and understanding of strong convective systems will be accomplished by documenting the environments that favor derechos and by identifying physical mechanisms that can maintain convective systems within environments that have not been emphasized in these past modeling studies.

[2] Favorable wind shear and instability parameters suggested by W93 are currently being taught to National Weather Service forecasters as part of the Cooperative Program for Operational Meteorology Education and Training (COMET) modules and were used by forecasters in support of the Bow Echoes and Mesoscale Convective Vortex (BAMEX) field program.

Chapter 2: Background

The analysis and interpretation of derecho environments is a primary focus of this study. This chapter begins with a overview of organized convective systems and then reviews the observational literature related to severe-wind producting convective systems.

Much of the research covered later in this study makes reference to the research of W93 and WR. Coniglio and Stensrud (2001) suggest that alternative perspectives on squall line behavior from other studies also may be applicable to strong convective systems. This Chapter reviews these subsets of squall line research and concludes with a synthesis of the past literature that motivates the goals of this study.

2.1. Effects of thunderstorm downdrafts

The factors that influence the strength of downdrafts within thunderstorms can be examined in a Lagrangian framework with the anelastic form of the vertical momentum equation,

$$\frac{dw}{dt} = -\frac{1}{\rho}\frac{\partial p'}{\partial z} + B \tag{2.1}$$

where the buoyancy, B, is defined as

$$B \equiv -g\frac{\rho_m'}{\rho_0} = -g\left(\frac{T'}{T_0} - \frac{p'}{p_0} + 0.61r_v' - r_h\right). \tag{2.2}$$

where ρ_m is the density of a moist sample of air, r_v is the water vapor mixing ratio, r_m is the total hydrometeor mixing ratio, and the other symbols have their usual meteorological association. Equation 2.1 says that, to a close approximation, the vertical acceleration of air parcels are controlled by vertical perturbation pressure gradients (term 1 on RHS) and

the combined effects of buoyancy (B) from temperature perturbations, pressure perturbations, perturbations in water vapor mixing ratio, and the total hydrometeor mixing ratio (term 4 on the RHS of eq. 2.2), where the perturbations (represented by primes) are in relation to a dry, hydrostatic reference state (represented by the 0 subscript). One of the many findings of the Thunderstorm Project (Byers and Braham 1949) is the close association of downdrafts, cold surface temperature anomalies, and rainfall. Decades of later research generally conclude that negative buoyancy associated with the evaporation and sublimation of precipitation is the dominant mechanism that induces downward air parcel accelerations (Wakimoto 2001).

2.1.1. Precipitation effects on downdrafts

Many factors continually influence the amount of cooling due to evaporation and sublimation of condensate. In general, evaporative cooling is enhanced by larger lapse rates, higher rainfall intensity, and small raindrop size distributions (Hookings 1965, Kamburova and Ludlum 1966). Lapse rates close to dry-adiabatic are especially important to maintaining downdrafts since parcels often do not approximate pseudo-moist adiabatic descent, particularly for lighter rainfall rates and larger drop sizes (Kamburova and Ludlum 1966, Gilmore and Wicker 1998).

The mixing of condensate with unsaturated air, and the resultant evaporation/sublimation, is thought to be an efficient mechanism to initiate downdrafts (Heymsfield et al. 1978, Knupp 1988, Carpenter et al. 1998). Consequently, lower environmental relative humidity (RH) or equivalent potential temperature (θ_e) in the entrainment region corresponds to the greater potential for initiating downdrafts by entrainment (Hookings 1965), usually from an *up-down* branch that is dynamically forced

upward from low-levels ahead of the storm, or a *midlevel* branch which enters the downdraft from above the boundary layer, either from the rear or front of the storm (Knupp 1987, Knupp 1989).

For maintaining downdrafts, Srivastava (1985) and Proctor (1989) find that downward parcel acceleration increases with *increasing* environmental RH along the parcel descent. This is because the higher moisture content leads to larger virtual temperature differences between the environment and the parcel than there otherwise would be in a drier environment. Entrainment of dry air along the parcel descent can be detrimental to maintaining downdrafts because the condensate may evaporate too soon and allow for dry-adiabatic compressional warming over a substantial depth. This is qualitatively supported by observations of environments supporting wet microbursts, in which θ_e-differences between low and midlevels are usually $\geq 20°C$ (Atkins and Wakimoto 1991). Therefore, it is suggested that entrainment of dry air helps to *initiate* downdrafts while moist low level air helps to *maintain* the downdrafts, although the quantitative contributions of each process remain unanswered.

Despite lower latent cooling for ice particles compared to liquid, Srivastava (1987), Proctor (1989), and Straka and Anderson (1993) find that ice particles can be very important in the initiation of downdrafts since ice can melt completely in a fall of a few kilometers, whereas raindrops of the same sizes can not evaporate completely under similar environmental RH values. The addition of frozen condensate has a more significant effect under stable lapse rates than a downdraft with only liquid water due to the additional cooling from melting and loading of the frozen particles over deeper layers (Wakimoto and Bringi 1988, Hjelmfelt et al. 1989, Straka and Anderson 1993).

Multiparameter radar measurements confirm the importance of radar-reflectivity cores of higher water contents in more statically stable environments, including the presence of hail shafts within descending precipitation cores (Wilson and Wakimoto 2001).

2.2 Observed characteristics of organized convective systems

A result of convection growing in size and becoming collocated with other cells is the collection of downdrafts and the horizontal spreading of the cooled air at the surface. This air often organizes into the "cold pool" associated with the convective system. The leading edge of the cold pool, termed the "gust front" (Goff 1976, Wakimoto 1982) can attain the characteristics of simple density currents (Benjamin 1968, Seitter 1986, Xu 1992), which can provide a proxy for the motion of cold pools. While cold pool motion is governed by many factors, including ambient wind speed and shear (Seitter 1986, Xu 1992, Chen 1995, Corfidi 2003), vertical momentum transfer (LeMone et al. 1984, Yang and Houze 1996, Trier et al. 1998), and terrain characteristics (Bosart and Sanders 1981), it is largely a response to the hydrostatically induced horizontal pressure gradient between the cooled air and the undisturbed environment. The existence of an organized convectively-generated cold pool that attains steady characteristics on timescales of at least a few hours and length scales greater than 100 km is central in the definition of mesoscale convective systems (MCSs) (Maddox 1980, Zipser 1982) and has been shown to be important to their dynamics.

2.2.1 Conceptual models of MCSs

The descriptions of MCSs given by Maddox (1980), Zipser (1982), and interpreted by Parker and Johnson (2000) and Fritsch and Forbes (2001) suggest that MCSs can include both circular convective systems (as viewed by satellite) and the more linear and

elongated systems, or "squall lines". Although the true spectrum of organized convective modes is likely continuous (Fritsch and Forbes 2001), a common characteristic of MCSs, especially the more robust variety, is the tendency for the strongest convection to become quasi-linear along the leading edge of the system. Observed as a distinct mode of precipitating convection for many years (Fujita 1955), convective systems of this type were originally conceptualized as a steady 2-D cell that allows for an efficient decoupling of the ascending updraft from the descending rain-cooled air (Ludlam 1963, Newton 1966). Upon a synthesis of many later years of detailed observations, Houze et al. (1989) conceptualizes the mature stages of a class of squall lines containing a convective zone

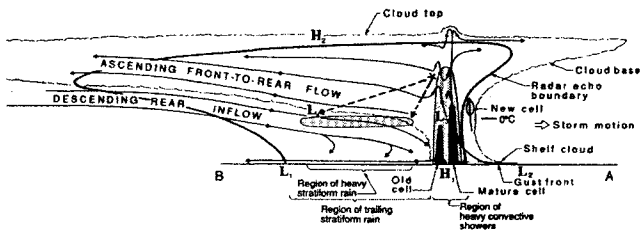


Fig. 2.1. Conceptual model of a squall line viewed in a vertical cross section in a plane parallel to its motion (from Houze et al. 1989).

with localized convective updrafts and downdrafts in various stages of their lifetimes (Fig 2.1) along the gust front and a stratiform precipitation region. They also describe a mesoscale descending rear-to-front flow that develops beneath the anvil cloud at the back edge of the stratiform rain region and may reach the surface and augment the cold pool. Smull and Houze (1987) postulate that the rear-inflow is a response to a midlevel mesoscale low perturbation pressure center that develops from the combined effects of latent heat release aloft in the saturated ascending air and the latent cooling below. Similar hydrostatically induced pressure mimima may be produced within and immediately behind the convective cores (LeMone 1983). Smull and Houze (1987) demonstrate the association of this rear-inflow-jet (RIJ) with relatively low values of θ_e,

which suggests that importance of the evaporation of rain and/or the sublimation and melting of frozen condensate (Stensrud et al. 1991, Yang and Houze 1995) in the initiation of RIJs. RIJs can attain relative speeds of 15 m s^{-1} as modeled by Weisman (1992) and Yang and Houze (1995), and as observed by Smull and Houze (1987) and Klimowski (1994), and may persist for several hours after the decay of the convective line.

The rear-inflow branch is often tied to a well-defined mesoscale cyclonic vortex that can develop within the stratiform rain region on the north end of the line and can give the system an asymmetric appearance in radar reflectivity (Houze et al. 1989). This vortex is thought to develop from a variety of ways, including the convergence of relative vorticity by the mesoscale downdraft air (Brandes and Ziegler, 1993), the mesoscale convergence of air acting on the existing absolute vorticity (Skamarock et al. 1994), the tilting/twisting of ambient vorticity (Houze et al., 1989), and/or the hydrostatic response to the core of latent heating within the system (Davis and Weismain 1994). Understanding the relative influences of these effects on organized convective systems remains a difficult observational problem and is one of the questions addressed by the BAMEX field project (Davis et al. 2004).

Parker and Johnson (2000), in a study of 88 linear MCSs, reveals that the classic trailing stratiform squall line model presented in Fig. 2.1 only comprises approximately 60% of the cases, indicating the complexity of line-oriented convection. Other modes include a "leading" stratiform one where the hydrometeors from decaying convective cells advect *forward* relative to the leading convective line (20%). They also observe the flow advecting the anvil along the line in cases they called "parallel" stratiform cases

(20%).

2.2.2 Characteristics of convectively-produced windstorms

The conceptual models described above represent general features common to a variety of MCSs. Many decades of observations have revealed additional features that are common among the types of organized convective systems that produce severe surface winds. Nolan (1959) and Hamilton (1970) recognized the existence of mesoscale wave patterns within linear MCSs, in which portions of the line accelerate in the direction

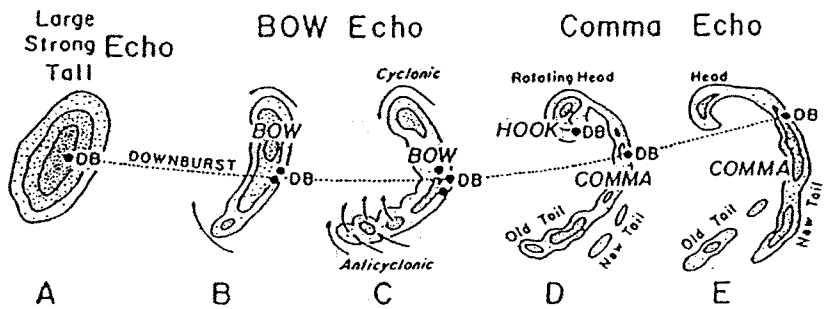


Fig. 2.2. The classic conceptual model of the evolution of a bow echo from a linear echo, to a bow echo, into a comma echo with a cyclonically rotating head. This model recognizes the possibility for tornadoes along the cyclonic shear side of the downburst (from Fujita 1978).

of the storm movement, producing a "line-echo wave pattern" (LEWP). From many years of detailed observational work, Fujita (1978) shows that long swaths of damaging surface winds often are found in the vicinity of the apex of a *bow echo* on radar reflectivity (Fig. 2.2). The bowing of the convective cell is thought to reflect the forward advancement of strong, diverging outflow winds at the surface. Weisman (2001) notes that many of Fujita's conjectures have been verified with Doppler radar studies, including his idea that bow echoes often are associated with strong rear-inflow and that tornadoes associated with bow echoes are usually found north of a cyclonically rotating head (Fig. 2.2). Weisman (2001) also notes that the most severe bow echoes typically range in size from 40 to 120 km and have lifetimes of several hours, but can occur on a wider range of

space and time scales. Although Fujita's conceptual model is based on the transition of a single cell into a bow echo, this evolution is thought to be present to some extent within bow echoes of all sizes and lifetimes (Weisman 2001). Smull and Houze (1987) and Jorgensen and Smull (1993) illustrate a common occurrence of rear-inflow branches that originate at heights of 4-6 km and can produce significant mesoscale downdrafts and a bow-shaped MCS on length scales of 100-200 km.

Przybylinski (1995) stresses that channels of weak echo, often called rear-inflow notches (RINs), commonly occur behind the leading edge of the convection at various scales and are proposed to be associated with evaporation in the descending RIJ or the downbursts. The flow may reach to the lower regions of the convective region where the RIJ combines with the convective-scale downdrafts to enhance the strength of the outflow winds (Wakimoto 2001). Regions where the RIJ is locally enhanced can distort the echo into smaller bows, as observed by Burgess and Smull (1990), Przybylinski (1995), Knupp (1996), and Funk et al. (1999).

The typical development of bow echoes is documented by Klimowski et al. (2000) and the significance of bow-echo structures is confirmed by Klimowski et al. (2003) who find that among a set of 198 organized convective storm types in the northern Plains region that occurred in a 4-year period, 86% (56 out of 65) of the bow-echo structures produced severe surface winds.

2.2.3. Characteristics of derechos

Building on the original description of derechos by Hinrichs (1888), JH87 define the derecho to include any family of "downburst clusters" produced by an extratropical MCS and use six criteria to identify derechos in terms amenable to the available

observations (Table 2.1). Fujita and Wakimoto (1981) define a downburst cluster as a swath of damage 10-100 km in length with embedded regions of more severe wind damage that cascade down in scale to ~100 m in length. "Families of downburst clusters" are defined as a series of downburst clusters produced by one storm system as it travels hundreds of kilometers. Although downbursts are central in this definition, severe

Table 2.1. Criteria used to identify derechos in JH87, Bentley and Mote (1998) and Coniglio and Stensrud (2004).

	JH87	**Bentley and Mote (1998)**	**Coniglio and Stensrud (2004)**
1)	There must be a concentrated area of convectively induced wind gusts greater than 26 m s^{-1} that has a major axis length of 400 km or more.	Same as JH87	Same as JH87
2)	The wind reports must have chronological progression.	Same as JH87	Same as JH87
3)	No more than 3 h can elapse between successive wind reports.	No more than 2 h can elapse between successive wind reports.	No more than 2.5 h can elapse between successive wind reports.
4)	There must be at least three reports of either F1 damage or wind gusts greater than 33 m s^{-1} separated by at least 64 km during the MCS stage of the event.	Not used	Low-end: Not used Moderate: Same as JH87 High-end: There must be at least three reports of either wind gusts greater than 38 m s^{-1} or comparable damage (see text), at least two of which must occur during the MCS stage of the event.
5)	The associated MCS must have spatial and temporal continuity.	The associated MCS must have spatial and temporal continuity with no more than 2° of latitude and longitude separating successive wind reports.	The associated MCS must have spatial and temporal continuity and each report must be within 200 km of the other reports within a wind-gust swath.
6)	Multiple swaths of damage must be part of the same MCS as indicated by the available radar data.	Multiple swaths of damage must be part of the same MCS as seen by temporally mapping the wind reports of each event.	Same as JH87

wind gusts often occur with the passage of the gust front, as a result of its fast translational speed, the turbulence in the density-current "head" region, downward

transfer of horizontal momentum, or from the hydrostatically induced surface pressure gradient. It is difficult to diagnose the separate contributions of the gust front and the individual downbursts to the wind gust swath and a general relationship of these contributions to derechos remains unknown (Wakimoto 2001).

Recent studies have used deviations from the criteria listed in Table 2.1 (Bentley and Mote 1998, Evans and Doswell 2001). While some of these changes can impact the interpretation of the derecho climatology (Bentley and Mote 2000, Coniglio and Stensrud 2004), the changes used in this study (see Chapter 3) do not change substantially the physical interpretation of the DCS as defined by JH87 (Coniglio and Stensrud 2004).

Many types of extratropical MCSs can produce derechos. However, through a study of 70 warm season (May-August) cases, JH87 show that most DCSs are composed of a quasi-linear, nearly continuous collection of strong convective cells along the leading edge of the system and that the downbursts and strong surface winds are usually associated with LEWPs and/or bow echoes in the leading convection. Bow echoes are often observed on a variety of length scales within a DCS (10-300 km) and several can be present simultaneously during a single event (JH87, Johns and Doswell 1992, Przybylinski 1995, Weisman 2001). MCSs that contain a small number (1-3) of bow echoes oriented at a large angle to the mean wind direction produce *progressive* derechos, which often move faster than the mean troposphere wind speed, suggesting that propagation is a significant component to the motion of DCSs (Corfidi 2003), but also may suggest gravity waves processes in more stable low-level environments (Schmidt and Cotton 1990). Progressive derechos often develop from a gathering of isolated cells that grow upscale into multicell clusters and eventually into highly organized MCSs, but

can sometimes develop from a single isolated supercell (Przybylinski 1995, Klimowski et al. 2003). More elongated squall lines, sometimes with several individual bow-shaped convective elements that move rapidly along the line in the direction of the mean wind, produce *serial* derechos (JH87). Additionally, embedded supercells and/or convective-scale cyclonic vortices often are embedded within the main system and may not be associated with identifiable bow-echo circulations. In some cases, these vortices are associated directly with the most severe wind damage (Schmidt and Cotton 1989, Przybylinski 1995, Bernardet and Cotton 1998, Spoden et al. 1998, Funk et al. 1999, Martinelli et al. 2000, Miller and Johns 2000).

2.2.4 Derecho Environments

Much of our current knowledge on DCS environments stems from the study of JH87, whose work was restricted to warm-season (and mostly progressive) derechos. West to northwesterly mid-level flow usually overlays a low-level quasi-stationary thermal boundary that is either tied to synoptic flows or to cold outflows from prior convection. The DCSs that occur in association with relatively weak short-wave troughs generally move at a small angle to this boundary from the cold side to the warm side. The strong trough cases tend to initiate north of a quasi-stationary boundary and then develop southward along or just ahead of a trailing cold front. In either case, significant low-level warm advection usually is present near the initiation of convection. Large amounts of conditional and convective instability, related to abnormally moist low-levels and relatively dry mid levels, also is found along the derecho track.

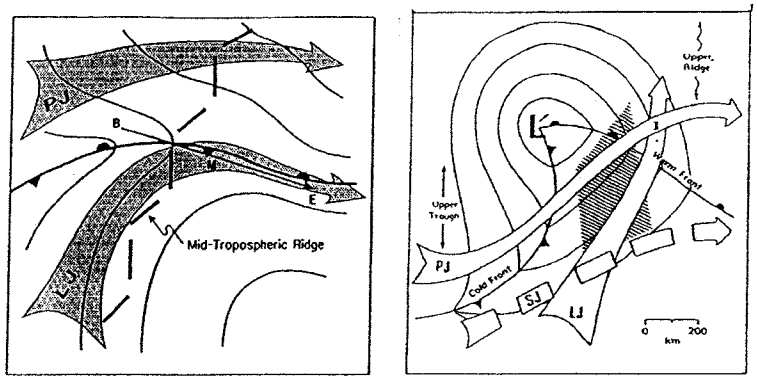


Fig. 2.3. Left panel: An idealized sketch of the warm season midlatitude synoptic scale pattern associated with especially long-lived progressive derechos. The line B-M-E represents the beginning, middle, and end points of the derecho. The thin lines depict the sea-level pressure field in the vicinity of quasi-stationary frontal boundary. Broad arrows denote the low-level jet (LJ) and the upper-tropospheric polar jet (PJ). Right panel: Idealized sketch of a midlatitude synoptic situation favorable for the development of serial derechos (the "dynamic" pattern). The upper-tropospheric subtropical jet is labeled SJ (from Johns 1993).

Depictions of the large-scale flow patterns associated with DCSs are mostly limited to the severe, long-track variety and are derived from the study of 14 such cases by Johns et al. 1990. Upon a synthesis with the results of JH87, this depiction is idealized into a "warm season" progressive pattern by Johns (1993) (Fig. 2.3). Johns (1993) also idealizes a "dynamic" pattern that is thought to occur primarily in association with serial derechos (Fig. 2.3). In general, the dynamic pattern consists of a strong, migrating low pressure system and is similar to the more "classic" pattern associated with general severe weather outbreaks, in which tornadoes and severe-wind outbreaks often occur simultaneously (JH87, Johns and Doswell 1992).

Little research had been published on the vertical profiles of derecho environments until the work of Evans and Doswell (2001). Their work illustrates that derechos occur under a wide range of environmental low-level shear and instability. Specifically, in a comprehensive analysis of the low-level shear distributions using 113 derecho proximity

soundings from 67 distinct events from all seasons, Evans and Doswell (2001) find that three-fourths of all the derechos occur with 0-2 km shear vector magnitudes less than 16 ms^{-1}. Additionally, the 0-6 km shear vector magnitudes mostly are less than 20 ms^{-1} for all cases examined. They suggest that the strength of the mean flow, and its effect on the motion of MCSs, enhances the potential for sustained severe wind gusts. They also recognize many cases that display features of both the warm season and dynamic patterns, which suggests the existence of a quasi-continuum of flow patterns with the strongly forced environment of the dynamic pattern and the benign large-scale forcing of the ridge pattern as end points. The frequency and structure of the distribution of these "intermediate" flow patterns has yet to be examined.

2.3 Conceptual models

Researchers have used a variety of analytical and numerical modeling frameworks to form general insights on the important physical mechanisms of squall lines and MCSs. While various contexts for describing squall line behavior have appeared in the literature over the last several decades, this section focuses on the class of research devoted to the response of the convective system to changes in the environmental wind shear.

2.3.1 Squall line simulations in 2-D

Many models of squall lines have emphasized the effects of low-level wind shear on the strength and structure of squall lines within an idealized numerical modeling framework, with the earliest attempts produced in 2-D. RKW notes that the earliest simulations failed to replicate a quasi-steady squall line within deep shear that contains a single updraft cell as suggested by the conceptual model of Ludlum (1963) and Newton (1966). As a potential reconciliation, Moncrieff (1978) and Lilly (1979), with the

significant benefit of computers available for the numerical simulation of squall lines, suggest that squall lines in 3-D within deep shear take on "supercell-like" circulations that allow for a long-lived, quasi-steady cells to compose the squall line. However, the observational evidence seemed to suggest that squall lines in general are not supercellular. Hane (1973) was one of the first to suggest that strong low-level shear with little or no shear aloft enhances the ability of simulated 2-D squall lines to become stronger and broader for longer time periods. He also showed the tendency for squall line cells to regenerate and decay rather than remaining at a constant strength over time.

The tendency for strong low-level shear with constant winds aloft to support the strongest and steadiest 2-D squall lines also is noted by Thorpe et al. (1982) since in environments with deep shear, no steady squall line is produced. In these cases, they interpret the steady squall line as being composed of time-dependent cells that are "superimposed turbulence" on the time-averaged flow. The smoothness of the time-averaged squall-line flow suggests several distinct flows, including an overturning updraft, a "jump" type updraft (similar to the front-to-rear flow in Fig. 2.2), a shallow downdraft, and low-level horizontal vorticity within the cold pool (representing the propagating gust front). Analytical models that have application to squall lines produced in the previous few decades are able to replicate these basic steady, time-averaged flows, the details of which are summarized in Moncrieff (1992).

The most widely referenced conceptual model for the behavior of squall lines relates to the work of RKW and Weisman et al. (1988). Using both 2-D and limited 3-D frameworks with only warm-rain processes represented in the equations, they find that the magnitude of the low-level shear normal to the convective line that balances the cold

pool circulation controls the strength and structure of long-lived squall lines. Unlike Thorpe et al. (1982), RKW emphasize the squall line steadiness as a result of the collection of ordinary cells that periodically generate and decay along the gust front, rather than the time-averaged circulation of the updrafts and downdrafts. The cold pool/shear "balance" is measured by comparing the prescribed wind speed difference perpendicular to the squall line (Δu) to estimates of the integrated negative buoyancy at some distance behind the gust front (C), which is derived from the 2-D horizontal vorticity equation using simplifying assumptions. In RKW, the wind speed is differenced over the lowest 2.5 km to approximately match the depth of the cold pool, but WR extend this depth to the lowest 5 km to account for action at a distance (Davies-Jones 2002) and, as proposed by WR, the ability of decaying rain cells above the cold pool to retrigger cells in an analogous way to the cold pool/low level shear interactions. Conditions that generate the deepest lifting and the most effective convective retriggering occur when $C \cong \Delta u$ (the "optimal" condition). For a given cold pool strength, or similarly, a given amount of baroclinically generated vorticity, values of low-level shear too large cause the convection to tilt downshear and deposit its rain into the inflow, which effectively cuts off the supply of unstable air to the updrafts. In the "suboptimal" phase, values of low-level shear too small, the overall system tilts upshear as a direct result of the overwhelming influence of the cold pool circulation.

In RKW, the suboptimal phase is proposed to signal the beginning of the squall line's decay, in which the gust front surges ahead of the updrafts. However, Fovell and Ogura (1989) find that none of their simulated squall lines demonstrate a decaying phase, even for very small wind shear. They view the suboptimal phase as one which causes the

model storm to be weaker and more clearly multicellular, but also one in which the thermodynamics can adapt to the ambient wind shear to continually regenerate convection for long periods. They show that the decaying behavior in RKW is a numerical problem in which the domain is not extended far enough away from the convection to prevent detrimental feedback to the solution, but WR argue that this problem does not influence the dependence of the squall line strength and structure described by RKW.

The theory of RKW is adopted by Weisman (1992) to explain the development of RIJs through the importance of strong low-level shear in the inflow. The optimal balance argument of RKW generally requires a significant amount of low-level shear in the inflow to counteract the negative vorticity produced by the cold pool. One way to interpret physically the optimal configuration of a vertically-oriented updraft is the condition which minimizes the dilution of the high-θ_e air in the updraft from the potentially cold air that composes the cold pool. From an analysis of 2-D numerical simulations, Weisman (1992) argues that the maintenance of this warm plume is essential for setting up the buoyancy gradients that control the strength and orientation of the RIJ. Horizontal buoyancy gradients at the back edge of the updraft plume and the cold pool create opposing circulations that draw environmental midlevel air into the storm. The flow can accelerate as a result of perturbation low pressure associated with vertical gradients of buoyancy between the surface cold pool and the convective plume aloft, as described by Smull and Houze (1987). If the horizontal buoyancy gradients associated with the warm plume aloft are greater than those associated with the cold pool near the surface, the RIJ tends to remain elevated to the back edge of the leading convective line.

Otherwise, the RIJs descend to the surface and spread within the cold pool well behind the main convection. Weisman (1992) claims that RIJs that remain elevated to the leading edge of the system promote strong quasi-steady and long-lived squall lines through their import of positive horizontal vorticity to the leading edge of the cold pool. In this situation, the main updrafts are "propped up" along the gust front which maintains the strength of the system. Although the development of suboptimal conditions are a necessary precursor for the development of rear inflow in this conceptual model, if the *initial* low-level shear is too weak relative to the cold pool, the plumes become diluted to the point of forcing the RIJ to descend to the surface well behind the leading edge of the cold pool, which leads to a much weaker system.

2.3.2 Squall line simulations in 3-D

As an extension of the 2-D simulations presented in Weisman (1992), W93 uses 3-D numerical simulations to examine the genesis of an idealized bow echo that evolves from a splitting single cell within a larger squall line system. Due to the generalizations made by W93, this is the most widely referenced paper for researchers over the last decade that attempt to explain the structures and environments of observed DCSs. He shows that the RIJ development described in Weisman (1992) and the adoption of the RKW ideas are evident also within the 3-D structures of bow echoes (Fig. 2.4). In addition, cyclonic and anticyclonic vortices develop along the ends of the line from tilting of ambient horizontal vorticity (called "bookend" vortices) that can accelerate the rear-inflow through rotational dynamic pressure gradients. Overall, deep forced lifting is promoted by the convergence of the strong, elevated RIJ and the low-level storm-relative inflow ahead of the system and is crucial for bow echo longevity.

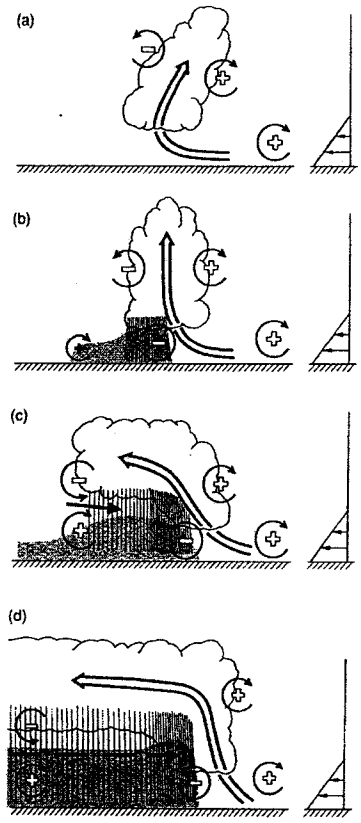


Fig. 2.4. Four stages in the development of an idealized bow echo developing in a strongly sheared, large-CAPE environment. The updraft current is denoted by the thick double lines, with the rear-inflow current in (c) and (d) denoted by the thick, dashed vector. The shading denotes the surface cold pool. The thin, circular arrows depict the most significant sources of horizontal vorticity, which is either baroclinically generated by the cold pool or is inherent in the ambient shear. Regions of heavier rainfall are indicated by the more sparsely or densely packed vertical lines, respectively. The scalloped line denotes the outline of the cloud (from W93).

Weisman and Davis (1998) and Weisman and Trapp (2003) simulate similar structures that evolve into larger-scale bow echoes with a dominant cyclonic circulation that resemble bow-echo complexes. They claim that much of the cyclonic circulation develops from the titling of negative horizontal vorticity that is generated by the system and that convergence acting on Coriolis rotation leads to the dominant cyclonic circulation. Also, they simulate smaller cyclonic vortices that form along the leading edge of the northern end of the bow echo similar to those displayed in Fig. 2.2.

Sometimes, these vortices merge with the primary cyclonic line-end vortex and can produce circulations that extend to midlevels. Trapp and Weisman (2003) suggest that these circulations may be a source for tornadic development associated with the comma head echo on the north end of the bow echo complex and may be the source of the strongest surface winds observed in severe bow echo storms.

Overall, Crook and Moncrieff (1988) and Fritsch and Forbes (2001) argue that the RKW conceptual model and its applications likely are to be most applicable to convective systems that occur in the absence of external forcing mechanisms and within a conditionally unstable lower atmosphere. Indeed, the meteorological literature contains a wealth of case studies that highlight the potential role of gravity-wave processes, dynamical forcing along frontal zones, intense short-wavelength troughs, or coupled-jet stream disturbances, in the development and maintenance of squall lines, which may diminish the importance of local-scale conditions on the overall maintenance of the system (Uccellini and Johnson 1979, Schmidt and Cotton 1990, Fankhauser et al. 1992, Funk et al. 1999, among others). Indeed, WR state that the theory of RKW applies primarily to conditions that lead to a solid line of convective cells along a significant cold pool that retains 2-D characteristics throughout its lifetime. Deeper shears or very strong low-level shears tend to allow the development of highly 3-D structures (RIJs, bow echoes, splitting and rotating individual cells) in the simulations that can complicate the results. However, using simulations with wind shear elevated above the cold pool, WR show that, for similar shear magnitudes, systems that produce the most rainfall, the largest rainfall rates, the strongest surface winds, and structures most resembling severe squall lines occur when the shear is entirely confined to low-levels, even when 3D

structures are allowed to develop. This result leads them to reiterate the primary importance of an optimal low-level shear/cold-pool balance in controlling the strength, structure, and longevity of squall lines, even if the shear is not entirely confined to the depth of the cold pool.

2.3.3 Density current models

A crucial element of the definition of an MCS is the development of a common outflow on scales of at least 100 km (Zipser 1982). Numerous researchers have shown that cold pools often behave like simple two-fluid density currents and have expanded upon the classic nonlinear, two-fluid treatment of Benjamin (1968). Application to squall lines has been inferred through examining the changes in the propagation speed, depth, and shape of an idealized density current (as a proxy for the cold pool) with changes in the environmental shear (of any depth). In particular, Xu (1992) and Xu and Moncrieff (1994) show that the vorticity-balance ideas of Rotunno et al. (1988) have little bearing on the steady propagation of density currents. This does not necessarily exclude the importance of a vorticity balance in initiating localized convection along the gust front, but it can lead to alternative viewpoints for the maintenance of the system-scale structure if the propagating current (cold pool) can initiate and maintain convection by other means (Moncrieff 1992, Xu and Moncrieff 1994).

A specific subset of density-current research provides insight as to how the system-scale structure might be maintained by the forced lifting of air over the advancing cold pool without dependence on vorticity arguments. In a model of sheared flow over a density-current impermeable barrier, Shapiro (1992) hypothesizes that increasing the shear throughout the depth of the troposphere decreases convergence and the associated

vertical velocity along the barrier owing to less mass impinging on the barrier. However, a decrease in vertical velocity does not translate into a decrease in vertical parcel displacements. Instead, air parcels that rise above the barrier may remain in the region of upward motion longer owing to weak system-relative winds in mid-levels and an overturning branch in upper-levels (depicted schematically in Fig. 2.5). It is hypothesized by Shapiro (1992) that increased residence time of air parcels leads to larger vertical parcel displacements and that these larger displacements can lead to a greater likelihood for initiating and maintaining convection.

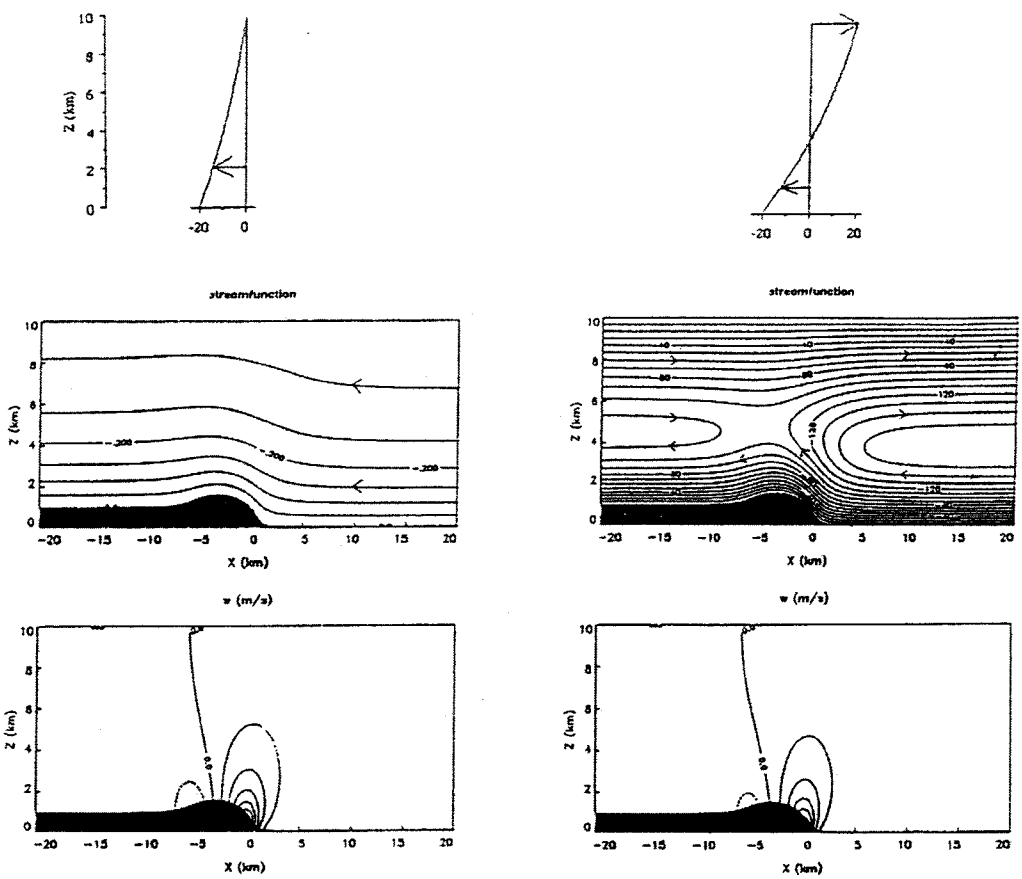


Fig. 2.5. Solutions from the hydrodynamical model of Shapiro (1992). The profiles in the upper-most panels represent changes in the magnitude of the wind (m s^{-1}) with height in a reference frame fixed with the density current barrier (shaded in black in the middle panels). Values of the streamfunction and the direction of the flow also is shown in the middle panels and the lower panels show vertical velocity (every 2 m s^{-1}) (adapted from Shapiro 1992).

Whereas the morphology of the density current is fixed in the work of Shapiro (1992), Chen (1995) and Liu and Moncrieff (1996) allow the characteristics of the current to respond to changes in the environmental wind profile. The ability to initiate and maintain convection is implied through the direct relationship between the depth of the density current "head" (the elevated region of the current along its leading edge) and the strength and depth of the horizontal convergence (and subsequent forced lifting). In a simplified 2-D framework, they show that the head of the downshear-propagating current becomes progressively deeper with shear (an approximate linear relationship), but becomes shallower when the shear exceeds a critical value. The shear magnitude that maximizes the depth of the density-current head decreases for increasing shear depth. Overall, the largest head heights and vertical motions occur for moderate shear values (4-5 m s^{-1} km^{-1}) and moderate shear depths (4 km). Shear values too large for a given depth cause the head structure to break down into multiple, shallow heads that reduce the forced lifting. This gives some support to the idea of an optimal shear profile and the importance of the low-level shear, but also suggests that the total shear (the product of the shear magnitude and the shear depth) may also be important if there are deeper wind shears and the explanation for this "optimal" condition is different physically than the RKW ideas, as implied by Garner and Thorpe (1992). These results generally are confirmed by the 2-D numerical simulations of Xue (2000), who suggests that upper-level shear plays a similar role to low-level shear in raising the head depth and increasing the frontal slope of the gust front, and thus, the convergence.

Moncrieff and Liu (1999) provide a synthesis of the results of Shapiro (1992) and Liu and Moncrieff (1996) by examining the effects of ambient wind speed, wind shear

and convergence on the ability of a density current to lift low-level environmental air. In both analytical and simplified numerical frameworks, they state that shear decreases the horizontal convergence due to less mass impinging on the downshear-propagating gravity current, but the presence of an overturning branch (that results from the positive shear in mid and upper levels) lifts boundary layer air to much higher levels. This lifting is enhanced when the lower-level wind direction opposes the direction of the mean shear vector, increases the convergence and leads to stronger, deeper vertical velocities. An overturning branch in a downshear-propagating density current implies the presence of a steering level, which anchors the incipient convection to the organized ascent along the density-current head.

There has yet to be a comprehensive treatment of how the above analyses can be modified by convective processes. It has been hypothesized that when the initial convection occurs above the head, the compensating subsidence occurs far enough ahead of the cold pool so that the head can adjust to the uninterrupted surface inflow by becoming deeper underneath the updrafts than it otherwise would with the subsidence occurring above the head (Garner and Thorpe 1992). Therefore, organized ascent associated with an overturning branch that allows convection to develop above the head may provide a positive feedback mechanism that maintains the depth of the head and promotes further convective development. Additional positive feedbacks may result from advection of the perturbation vorticity, generated on the downshear flank of the convective plume, into the background positive vorticity of the overturning branch (Garner and Thorpe 1992). Subsequently, it is reasonable to assume that this process is easier to realize with increased potential buoyant energy in the inflow layer, which

effectively reduces the convective time scale and ensures that the mature convective plumes do not drift far from their location of initiation (Garner and Thorpe 1992).

Since the above studies generally use model atmospheres that are neutrally stratified, unsaturated, free of heat sources, and constrained by 2-D flows and balance assumptions, the applicability of these models to line-type outflows governed by buoyancy forces is certainly in question. However, the consistency of the result that the forced lifting and the vertical displacement of parcels becomes deeper in the presence of deep vertical wind shear among a variety of simplified density-current frameworks provides justification to further examine these results in model frameworks similar to those used by RKW, W93, and WR.

2.4 Discrepancies in observations and idealized models

As a preliminary examination of the results from density current applications, Coniglio and Stensrud (2001) simulate a progressive derecho within a full-physics 3-D model initialized with a horizontally nonhomogeneos environment derived from a simple composite analysis of observed derecho environments. The model develops an asymmetric squall line with complex 3-D rear-inflow and embedded bow echoes along the leading line. They find that DCS-like structures can develop and persist within low-level shear profiles that have difficulty producing bow echo structures in the work of W93 and WR. Weisman and Davis (1998) and Weisman and Trapp (2003) simulate a bow-echo complex, but only for shear greater than 20 ms^{-1} over the lowest 2.5 km, which prevents the comparison of the shear required to produce this structure versus the bow echo in W93. The mean wind profile in Coniglio and Stensrud (2001) consists of about 3-4 m s^{-1} km^{-1} of shear. However, this shear is distributed over the entire depth of the

troposphere, unlike the W93 simulations, but similar to the shear profiles considered favorable for maintaining deep, forced lifting along the gust front in the models of Shapiro (1992) and Moncrieff and Liu (1999). Weisman and Rotunno (2004) extend shear layers to 10 km, but find a mixture of supercells and upshear-tilted multicellular squall lines isolated along the gust front. They stress that the characteristics of the squall lines under these conditions show little sensitivity to changes in the upper-level shear and are not as strong or as organized as the squall lines that develop in zero upper-level shear. Additionally, bow echo structures only develop in their simulations if the shear is confined to the lowest 5 km. In the simulation of Coniglio and Stensrud (2001), most of the cells were not supercellular in nature, but were more of a mix of ordinary cells and bow echoes embedded within the main convective system.

Further discrepancy comes from the fact that the observational results of Evans and Doswell (2001) are somewhat inconsistent with the parameter study of W93 who finds that shear of 15 ms^{-1} or less (over the lowest 2.5 or 5 km) support systems that can produce strong surface winds, but are described as "upshear-titled systems of rain cells tens of kilometers behind the gust front", in which "the structures described for the idealized, long-lived bow echo do not develop". W93 also finds that structures similar to the idealized bow echo require at least 2000 $m^2 s^{-2}$ of convective available potential energy (CAPE) and at least 20 m s^{-1} of low-level shear. Using finer resolution and much larger domain sizes, very similar conclusions can be made from the recent simulations presented in WR, which confirms that organized bow echoes only are produced if the shear layer is confined to the lowest 5 km. The requirement of at least 2000 $m^2 s^{-2}$ of CAPE is likely tied to the inability of idealized cloud-scale models to represent external

forcing mechanisms (e.g. from frontal circulations or jet-induced ageostrophic circulations). However, the requirement of such large values of low-level shear is not clear and is not supported by the observations.

Evans and Doswell (2001) also show little correlation between proxy measures for cold pool strength (potential temperature differences between the environment and the cold pool and values of downdraft CAPE), and the strength of the low-level shear, which further suggests a disparity between the observations and theory of RKW, which is modified to allow for deeper shears, yet reaffirmed in WR.

2.5 Summary

The above literature review highlights a disparity between observations of derecho environments and those required to simulate derecho-like structures in idealized models. This may stem from the lack of detailed knowledge of the 3-D derecho environments. Overall, this study intends to document the range and structure of the large-scale flow patterns and environmental parameters associated with the development of derechos. It will be shown that derecho environments often have substantial upper-level shear and substantially more *convective* instability than represented in the initial profile of W93 and WR, particularly for the more weakly-forced events. Using these observational results as a guideline, this study intends to test the hypotheses gathered mainly from the work of Shapiro (1992), Liu and Moncrieff (1996), and Moncrieff and Liu (1999) that the addition of shear above the cold pool to a wind profile with "suboptimal" low-level shear can enhance the ability of the cold pool to initiate and maintain convection. The ultimate goal is to provide a new conceptual model for the development and maintenance of strong convective systems under these conditions.

Chapter 3: Data Set and Analysis of Large-Scale Environments

Meeting the objectives of this study requires an appropriate blend of observational and model data. This chapter covers the methods for identifying and analyzing the derecho data set and discusses the results.

3.1 Derecho Criteria

Storm Data provided by the National Climatic Data Center (NCDC) and the Storm Prediction Center (SPC) convective wind database are examined from the years of 1980-2001 to identify derecho events. A convectively induced windstorm is considered a derecho if:

1) There is a concentrated area of wind gust (≥ 26 ms^{-1}) or wind damage reports with a major axis ≥ 400 km in length,
2) the wind reports show a near-continuous progression in a single or series of swaths with no more than 2.5 h or 200 km between concentrations of reports,
3) the parent convection is organized into an MCS and exhibits a distinct linear radar reflectivity structure, and
4) the wind reports are not associated with tropical storms or hurricanes.

Note the lack of the JH87 criterion of 3 reports of wind gusts ≥ 33 ms^{-1} (or F1 damage) separated by 64 or more km, which is also lacking from the criteria used by Bentley and Mote (1998) (see Table 2.1). This allows the inclusion of severe-wind producing MCSs that are somewhat more benign than the severe MCSs considered to be derechos in JH87. Additionally, since JH87 only considered wind reports from the bow-echo or linear stage of the MCS, systems with somewhat shorter lifetimes than those considered in JH87 are

included in this study. In addition to the available surface charts, the available Weather Surveillance Radar (WSR-88D) level II reflectivity data obtained from the National Climatic Data Center (NCDC), the WSR-88D mosaic reflectivity images at 2-km or 4-km resolution, or the archived hourly radar summary charts produced by the National Centers for Environmental Prediction (NCEP) are used to verify criterion #3. Wind reports that compose the derecho path are determined by a combination of a temporal mapping of the reports and an inspection of the radar data. Reports from isolated cells are allowed as long as those cells eventually develop into or become part of the MCS.

There are 270 derecho events that are identified using the above criteria. It is found that determining a dominant radar reflectivity structure from the archived radar summary charts is often very difficult. Considering that JH87 identify 70 events in the warm season months of 1980-1983, the assessment of the criteria in this study is very conservative and reveals the importance of the first-hand experience and logs of severe weather events from operations used by JH87. The fact that the standards of severe wind gust reporting and damage surveying has been inconsistent over the years (Johns and Evans 2000) has led to a dramatic increase in the number of wind reports over the last quarter century (Weiss et al. 2002). These factors likely cause the trend in the distribution of derecho events toward the later years in this study (Fig. 3.1).

In addition, a bias is introduced due to the highly irregular distribution of populated areas east of the Rocky Mountains. This hinders the ability to describe the true geographical distribution of events from the raw data (Johns and Evans 2000). However, the primary intent is to obtain a large data set of derecho events and not to estimate the true geographical distribution [see Coniglio and Stensrud (2004) for a discussion].

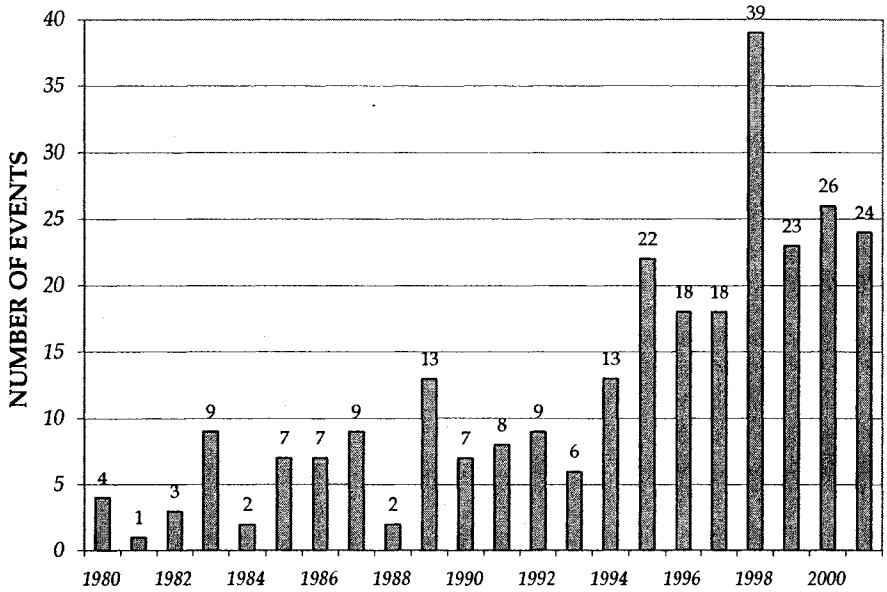


Fig. 3.1. The yearly distribution of derechos in the data set.

3.2 Analyzing Large-Scale Environments

The goal of identifying typical large-scale flow patterns is met through the examination of constant pressure analyses that represent the environment during the development of DCSs. This study uses the four-times daily analyses on 2.5° grids (valid at 0000, 0600, 1200, and 1800 UTC) from the NCEP-National Centers for Atmospheric Research (NCAR) Reanalysis data set (Kistler et al. 2001). The time of the analysis that is closest to the time of the first wind report is used to represent each case.

Since there is a wide range of durations observed among the events (5 to 30 h), the environments relative to the lifecycle of each event are preserved by defining a normalized observation time, t_{obs} (if the derecho begins at 0600 UTC and terminates at 1800 UTC, then t_{obs}=0.5 for the 1200 UTC analysis). t_{obs} must be estimated for the cases in which the derecho appears to begin (or end) over Canada or over oceanic waters. The data set is further restricted to include only those cases with $|t_{obs}| \leq 0.25$. This restriction

removes some of the shorter-lived events from the data set, but ensures that environments associated with the initiation and early-mature stages of the DCSs are represented. This procedure retains 225 out of the 270 cases.

3.2.1 Analysis Method

The first goal of this study is to determine if there are preferred large-scale flow patterns associated with the development of DCSs and, if so, the structure of the patterns. In this study, the patterns are defined first by the subjective recognition of the primary synoptic-scale feature that influences each DCS. To supplement the subjective approach, a method based on cluster analysis to the 500-hPa geopotential height field (ϕ) is used as guidance. The basic benefit of using a semi-objective technique, such as cluster analysis, is to provide an element of objectivity to determining a meaningful stratification of the data which might otherwise be overlooked in an entirely subjective technique, especially when dealing with a large data set (Wilks 1995).

In this application, grid-point values of ϕ from the representative analysis are interpolated to a Cartesian grid with its origin located at the intersection between the DCS leading edge (or initial convective cluster) and the derecho major axis. Each grid has 27 points in the east-west direction and 25 points in the north-south direction (675 total) spaced 100 km apart. An $n \times p$ data matrix, $\mathbf{X}$, is formed with the 225 cases as the n columns and the 675 grid point values of ϕ as the p rows.

Past DCS literature emphasizes the subjective recognition of flow patterns in terms of the shape and orientation of the geopotential heights (JH87, Bentley et al. 2000, Evans and Doswell 2001). A reasonable choice to quantitatively relate the 225 cases in this manner is the Pearson correlation coefficient (Wolter 1987). Application of this measure

to **X** results in an $n \times n$ symmetric matrix composed of the correlation coefficient among all of the columns of **X**.

Gong and Richman (1995) showed that non-hierarchical techniques outperformed hierarchical techniques in an application to a 40-year data set of 7-day precipitation data. However, non-hierarchical methods require the generation of "seed points", which is based on an initial assessment of the likely number of "correct" clusters among the data. In the application to 500-hPa height fields in this study, the likely range for the number of clusters that best group the data is not known through subjective knowledge and the goal is to provide a visualization of the range of flow patterns that emerge from the individual cases. Therefore, various hierarchical agglomerative clustering algorithms are then used to define groupings (clusters) of the cases based on **X**. This study uses several algorithms that are frequently applied to geophysical data (Gong and Richman 1995), including three variations of the "average linkage" technique and the "minimum variance" method (Ward's method) (Degaetano 1996). There are many objective rules that can help the user in determining the number of clusters (Degaetano 1996). Despite that, none is accepted as foolproof or superior under a range of applications, hence some subjectivity is introduced. In this study, the algorithm is stopped before it combines clusters that have clear distinctions based upon a visual inspection of the associated members. This is justified since the field of ϕ and its spatial variability tends to be smooth, and thus, it is unlikely that any true number of clusters exists (Dagaetano 1996). Accordingly, there are a number of potentially meaningful solutions that depend on the level of similarity desired in the solution (Fovell and Fovell 1993) that are limited by the scale of the analyses.

Among the set of analyses, clustering is tested first using the correlation measure to help identify the distinct patterns. This measure removes the mean and variance of each case, which allows cases from different seasons to be classified into the same pattern. Hence, the composite maps based on this output represent significantly smoothed patterns with an unnecessarily large variance among the members of each composite.

To improve the illustration of the variability within the patterns through composite maps, it is desirable to find analyses that are similar in terms of both their mean and variance. In order to reduce the variance in 500-hPa height magnitudes within each cluster, and thus to create a more meaningful composite, clustering using the Euclidean distance measure is applied to the analyses in each pattern. Euclidean distance is frequently used as a dissimilarity measure (Gong and Richman 1995), which results in an $n \times n$ symmetric matrix composed of the root of the sum of squared differences among all of the columns of **X**. This helps to identify the cases with similar grid-averaged ϕ and the gradient of ϕ across the grids, which are then separated into clusters within each pattern. In this application, this two-tiered approach, which groups the analyses into patterns based on the shape of the 500-hPa heights fields followed by the generation of clusters within each pattern based on both the shape and magnitude and gradient of the 500-hPa heights, ultimately improves the ability to visualize the patterns, and the variability within them, over what is possible from a single stratification of the data set.

3.3 Results

Results suggest that a wide spectrum of flow patterns is associated with the development and early evolution of DCSs. However, the majority of the events (72%) fall into three main patterns that include a well-defined upstream trough (40%), a ridge

(20%), and a zonal, low-amplitude flow (12%). The variability within each pattern is visualized through the composite maps generated from averaging the analyses that compose the clusters within each of the three main patterns (Figs. 3.2, 3.5 and 3.6). The

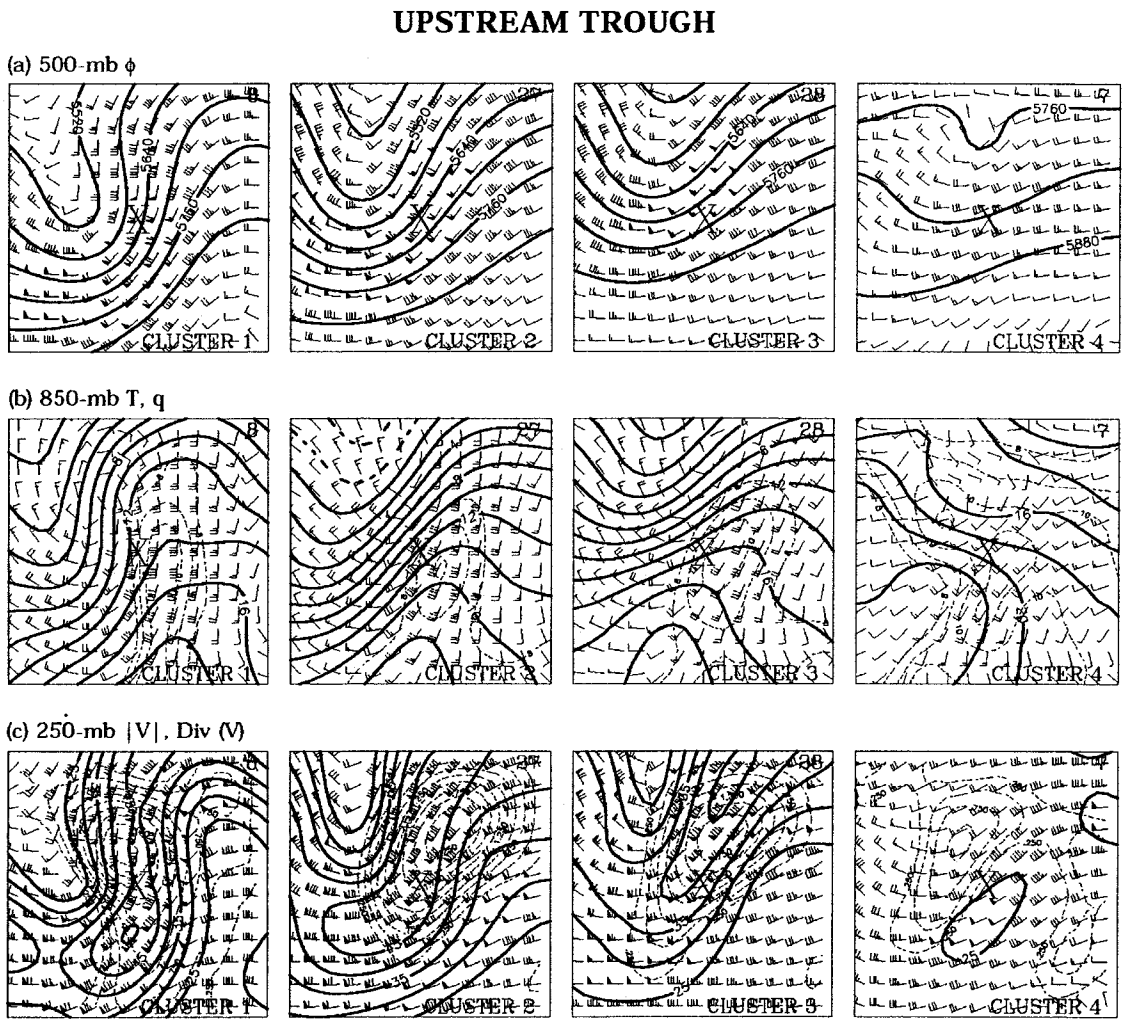


Fig. 3.2. (a) The mean 500-mb geopotential height (ϕ, contours every 60 m) and wind (flag = 25 m s^{-1}, full barb = 5 m s^{-1}) for four clusters within the upstream-trough pattern. (b) As in (a), except for the 850-mb temperature (T, solid contours every 2 K) and specific humidity (q, dashed contours every 1 g kg^{-1} starting at 8 g kg^{-1}). (c) As in (a), except for the 250-mb wind speed (|V|, solid contours every 5 m s^{-1}, starting at 25 m s^{-1}) and divergence of the wind (Div (V), dashed contours every 0.25 x 10^{-5} s^{-1}). The horizontal and vertical dimension of each grid is 2600 km by 2400 km, respectively. The X denotes the position of the DCS at the analysis time. The number in the upper-right corner of each grid denotes the number of analyses in each composite (cluster).

remaining cases (28%) exhibit either large-scale hybrid patterns that are combinations of the three main patterns or unclassifiable patterns (according to the three main classifications). The section below focuses on the characteristics of the three main patterns.

3.3.1 Upstream-trough pattern

The upstream-trough pattern is formed from 91 cases (40.4%) that have a well-defined mobile upstream trough as the primary influence on the development of the DCS (Fig. 3.2). The *large-scale* estimate of the mean mid-level differential vorticity advection is found to be 4 to 6 times larger for the upstream-trough events than for the ridge and zonal-flow events (mesoscale shortwave troughs embedded within the larger scale flow may provide significant forcing in the zonal and ridge patterns, but this cannot be determined from the relatively coarse Reanalysis data). Accordingly, these events best match Johns' (1993) strong large-scale forcing/dynamic pattern and mostly exhibit characteristics of serial derechos. The upstream-trough events occur most frequently along the Gulf Coast states, with a secondary activity corridor from the mid-Mississippi valley region through the lower Ohio valley (Fig. 3.3). The upstream-trough events occur throughout the year, with the majority of events residing in the colder months (Fig. 3.4). Notice that while many events occur in May, many of these events occur in the first half of May under "cold-season"-like conditions. This shows that while the dynamic pattern (and the serial derecho) is not rare during the warm season (20% occur in June-August) it is typically a cold-season pattern.

Four main clusters are identified that include 70 out of the 91 events (77%) from the upstream-trough pattern. The first upstream-trough cluster illustrates a very high-

amplitude trough west of the DCS location (cluster 1 in Fig. 3.2a). Clusters 2 and 3 in Fig. 3.2a illustrate two additional upstream-trough clusters that are distinguished by progressively higher mean heights, a lessening of the mean trough amplitude and a

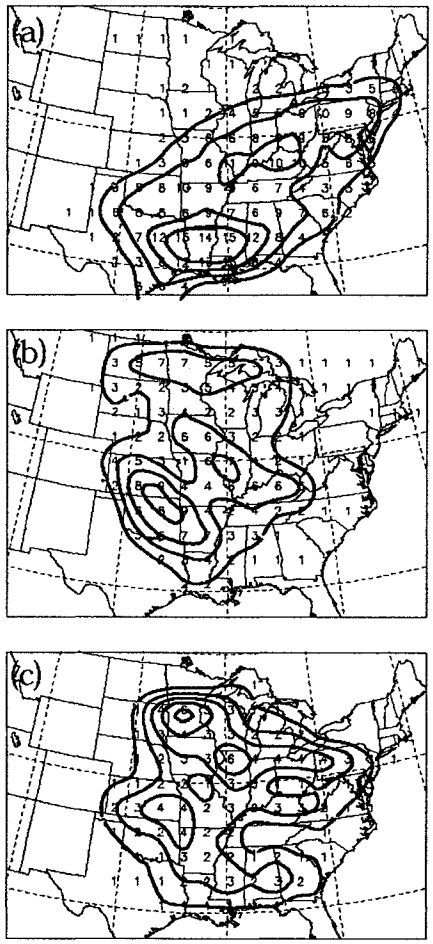
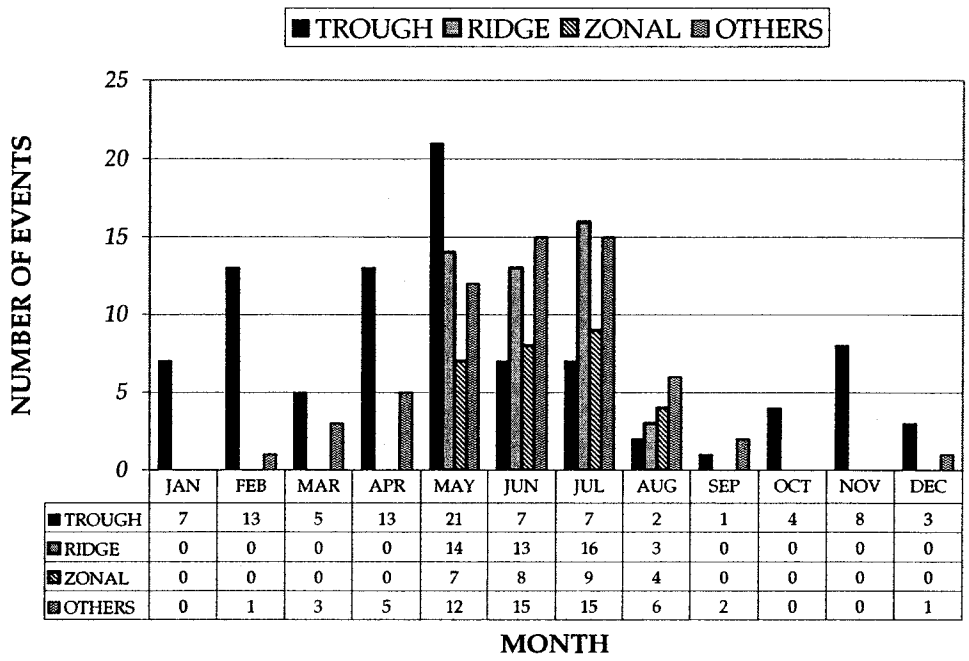


Fig. 3.3. The total number of derecho major axes that occur in 200 km by 200 km squares for (a) the 91 cases in the upstream-trough pattern, (b) the 46 cases in the ridge pattern, and (c) the 28 cases in the zonal pattern. Contours are drawn every 3 events in (a), every 2 events in (b), and every 1 event in (c).

decrease in the 500-hPa wind speed. These two clusters illustrate the most common type of upstream-trough event (see Duke and Rogash 1992 and Funk et al. 1999 for examples). The remaining cluster is formed from 7 warm-season upstream-trough events, with a seasonally strong, positively tilted trough propagating through a mean

westerly flow. Notice that within each cluster, the mean 500-hPa winds are strongest near the DCS location, indicating that the DCS often develops in the vicinity of a mid-level jet propagating around the base of the trough.



	JAN	FEB	MAR	APR	MAY	JUN	JUL	AUG	SEP	OCT	NOV	DEC
TROUGH	7	13	5	13	21	7	7	2	1	4	8	3
RIDGE	0	0	0	0	14	13	16	3	0	0	0	0
ZONAL	0	0	0	0	7	8	9	4	0	0	0	0
OTHERS	0	1	3	5	12	15	15	6	2	0	0	1

Fig. 3.4. The total number of derechos occurring during each month for each of the three main patterns. The counts are given in the table below the figure.

A southerly wind maximum is found ahead of a large-scale thermal boundary at 850-hPa in the upstream-trough pattern (Fig. 3.2b). Low-level cyclogenesis is well underway in many of the colder-season events (mostly clusters 1 and 2), as the warm advection is maximized to the north and east of the DCS location. A well-defined 850-hPa moisture axis lies along the axis of maximum wind ahead of the thermal boundary, which suggests that large-scale moisture transport occurs for many hours prior to development in these cases. In addition, the mean low-level jet axis is oriented at a relatively small angle to the mean mid- and upper-level jet, which is characteristic of a

pattern that may discriminate derecho occurrences from tornado outbreaks (Johns 1993). A thermal ridge becomes more evident to the southwest of the DCS location as the mean trough decreases in amplitude. This is especially apparent in cluster 4 in which the thermal boundary appears to now be oriented from west-northwest to east-southeast, with the maximum of warm advection returning to the location of DCS development. Cluster 4 shows a moisture axis extending from the south, as in clusters 1-3, but also shows a secondary axis extending east along the thermal boundary.

The left exit region of a strong upper-level jet, and the associated divergence, often is located near the DCS location in cluster 1 (Fig. 3.2c). This also is found for cluster 2, with a broad region of upper-level divergence near the DCS location that can be associated with either the polar jet or the subtropical jet. Combined with the strong south-southwesterly flow and the mean frontal position at 850 hPa (Fig. 3.2b), this provides a favorable environment for the coupling of upper-level and lower-level jets, which has long been identified as a contributor to severe weather outbreaks (Uccellini and Johnson 1979). The increasing influence of the polar jet is seen for cluster 3 as the mean jet has shifted to the northeast, although the subtropical jet is still present in a few of these cases. The 250-hPa jet is considerably weaker for the cases in cluster 4 and does not show a preferred location, although the mean pattern still displays a broad region of divergence just upstream of the DCS development region.

3.3.2 Ridge pattern

The ridge pattern is formed from 46 events (20.4%) that are influenced by the anticyclonic flow around a ridge at 500-hPa (Fig. 3.5). These cases best match Johns' (1993) warm-season pattern and all exhibit characteristics of progressive derechos. The

ridge pattern events occur in three distinguishable regions; one stretching northwest to southeast across the southern Great Plains, one stretching west-northwest to east-southeast from Iowa to Kentucky, and another stretching west to east from the northern

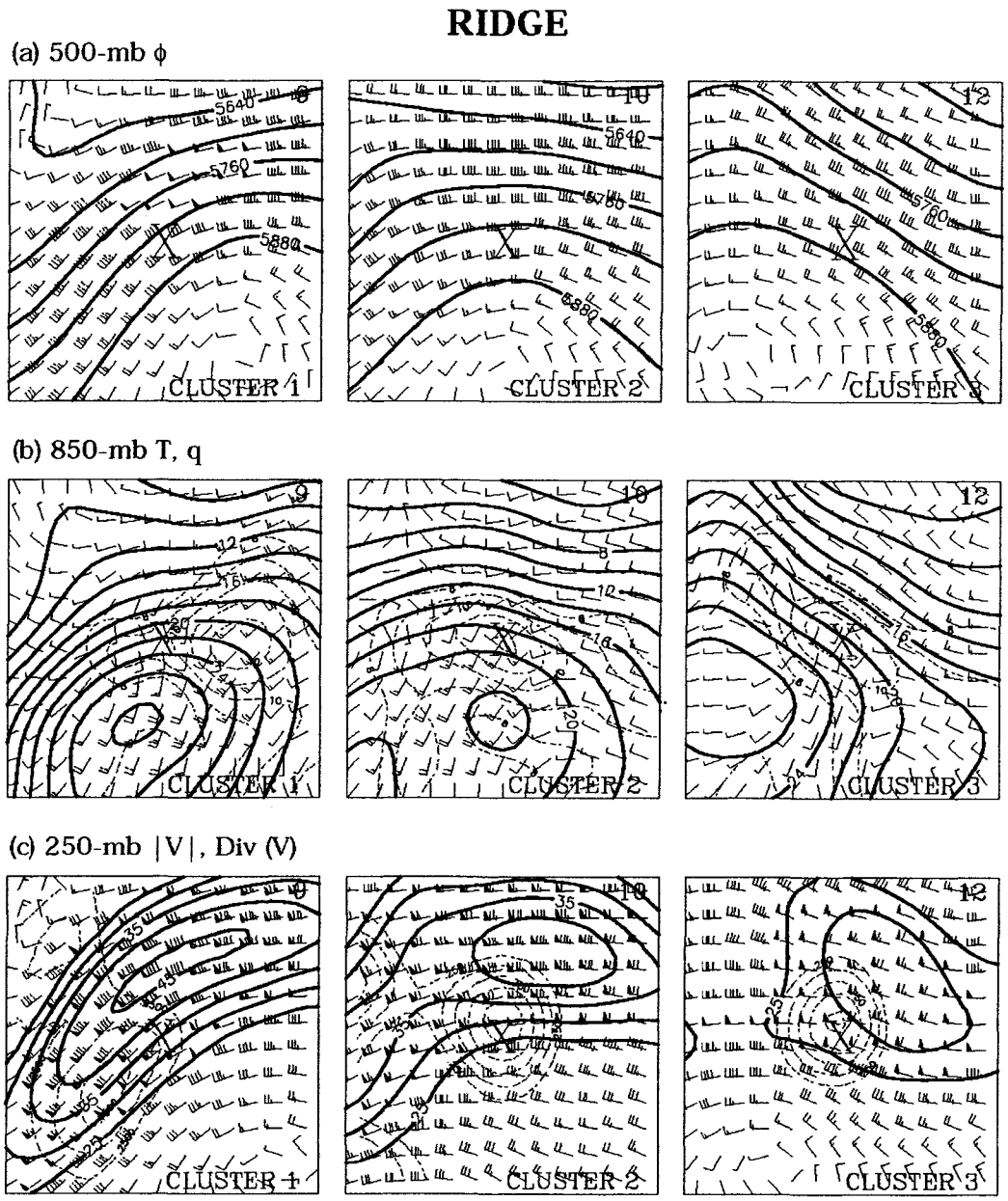


Fig. 3.5. As in Fig. 3.2, except for the ridge pattern.

Plains to the western Great Lakes region (Fig. 3.3b). The 46 ridge events all occur during the warm-season (Fig. 3.4).

Three main clusters are identified in the ridge pattern that include 31 out of the 46 cases (67%). The first cluster contains 9 events that develop upstream of the ridge axis. The mean pattern displays a short-wave trough in the process of breaking down the northern extent of the strong ridge. This produces a mean 20-25 m s^{-1} 500-hPa jet just to the north of the DCS location (Fig. 3.5a). All of the cases in this cluster develop in the northern Plains region (not shown) and are long-lived events. An example is the particularly destructive derecho event on 4-5 July 1999 that developed in South Dakota and decayed many hours later off the coast of Maine (Miller and Johns 2000). The second cluster identifies 10 events that develop near the axis of a flat ridge with a weakly confluent zonal flow to the north (cluster 2 in Fig. 3.5a) (see Evans and Corfidi 2000 for an example). The mean 500-hPa wind speed is weakest for this cluster, with values of 15-18 m s^{-1} near the location of DCS development. The third cluster identifies 12 events that develop downstream of a high-amplitude ridge within mean 500-hPa northwesterly flow of 16-20 m s^{-1} (see Miller et al. 2002 for an example). Many of these cases display a weak, short-wave trough digging southeast downstream of the ridge, which produces stronger flow in the vicinity of and the northeast of the DCS location.

The patterns of 850-hPa temperature for the ridge pattern (Fig. 3.5b) qualitatively resemble their associated pattern of 500-hPa heights, with a thermal boundary oriented parallel to the mean mid-level flow. This is a sign that the mid-level large-scale flow often is equivalent barotropic (Bluestein 1993) and suggests that the large-scale forcing often is provided through low-level warm advection. As identified by Johns et al. (1990),

a common thread to these events is that the warm advection becomes progressively weaker downstream. An axis of 850-hPa moisture along the thermal boundary near and downstream (relative to the mid-level flow) of the DCS location is clearly evident in this pattern, which is another important feature originally identified by JH87 and Johns et al. (1990).

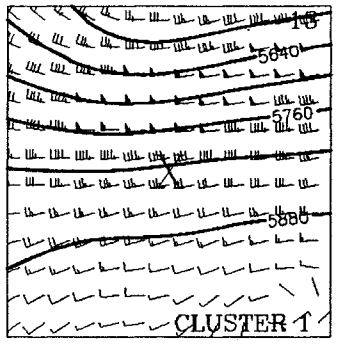
An interesting finding is that the right-entrance region of a strong polar jet is usually located near the DCS for the cases within this pattern. In addition, a comparison of Figs. 3.5a and 3.5c shows that the mean wind speed increases by as much as 20-25 m s^{-1} from 500 to 250 hPa near the location of DCS development. Although the mesoscale details are beyond the scope of this paper, these two factors produce a favorable scenario for the development of ageostrophic, thermally direct circulations related to jet-stream disturbances (Bluestein 1993). It is likely that these jet stream circulations augment the forcing provided by low-level warm advection in many of the events. The jet is strongest for the cases in cluster 1, with 250-hPa wind speeds as high as 40-45 m s^{-1} just to the north of the DCS location. The prevalence of the right-entrance region of the jet also is evident in clusters 2 and 3, with the maximum of divergence almost exactly co-located with the location of DCS development.

3.3.3 Zonal pattern

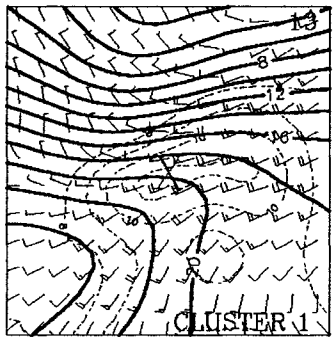
The zonal pattern contains 28 events (12.4%), mostly progressive derechos, that identify an additional warm-season pattern that has not been emphasized in previous literature (Fig. 3.6) (see Spoden et al. 1996 for an example). The zonal flow events tend to occur most frequently from the upper Midwest through the lower Great Lakes region, but also occur in the eastern Plains and the Gulf Coast states (Fig. 3.3c).

ZONAL

(a) 500-mb ϕ



(b) 850-mb T, q



(c) 250-mb |V|, Div (V)

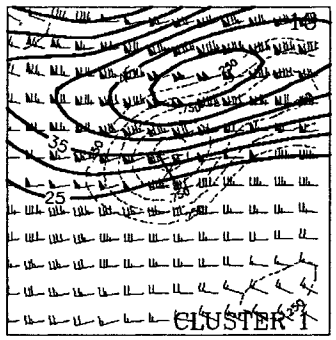


Fig. 3.6. As in Fig. 3.2, except for the zonal pattern.

The composite maps from a cluster of 13 events show a strong mean midlevel flow of 25-30 m s^{-1} just to the north of the DCS location (Fig. 3.6a). Despite the lack of an identifiable mid-level trough in the mean flow, a trough axis is evident at 850-hPa in the wind field, which extends southwest to northeast upstream of the DCS location (Fig. 3.6b). A mean southwesterly 850-hPa flow of approximately 10 m s^{-1} extends ahead of

this trough and lies along a thermal ridge axis to the south and west. A strong east-west oriented thermal boundary lies near and to the north of the DCS location, with a zone of warm advection and an axis of moisture that stretches near and downstream of the DCS

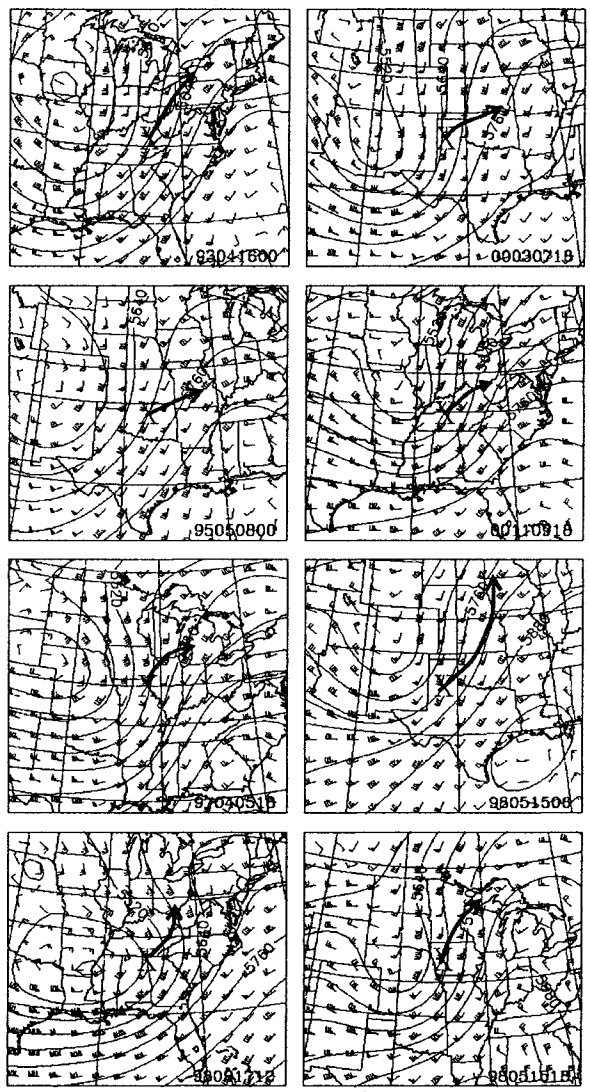


Fig. 3.7. The 500-mb geopotential height and wind (as in Fig. 6) for the 8 cases that comprise cluster 1 in the upstream-trough pattern. The **X** denotes the approximate location of the DCS at the analysis time and the arrow depicts the approximate track of the derecho major axis. The date and time (UTC) of each analysis (in YYMMDDHH format) is displayed in the lower right of each panel.

location. As in many of the ridge cases, an unseasonably strong 250-hPa jet (shown with a mean speed > 50 m s^{-1}) lies to the north of the DCS location and places the

development region in its associated divergence. As in the ridge pattern, this suggests the frequent existence of jet streaks propagating through the mean flow and the possibility of ageostrophic thermally direct circulations that aid in the development of the systems.

3.4 Discussion

It should be emphasized that the individual cases within each cluster necessarily display a degree of variability on scales resolved by the Reanalysis data that is inherent in the choice of detail allowed in the clusters. As an example, the individual analyses that comprise cluster 1 of the upstream-trough pattern are shown in Fig. 3.7. These analyses display similarities in terms of the direction and speed of the mid-level flow, as well as the mean pattern and magnitude of the heights, but show some variability in the shape and position of the trough. This is in addition to mesoscale details that are often superimposed on the main flow (Przybylinski 1995, Bosart et al. 1998, Klimowski et al. 2000, Miller and Johns 2000), but are not considered in this analysis.

Forecasters should also be made aware that large-scale hybrid patterns and some unclassifiable patterns account for the remaining 28% of the events. The hybrids combine various characteristics of the three main patterns and mainly occur in the warm season (three examples are shown in Fig. 3.8). The variability inherent in the patterns and the tendency for the spectrum to show a continuum of flow types is suggested in Fig. 3.9, which shows histograms of attributes among the three main flow types and the other flow patterns. The tendency for the "hybrid" cases to fall between the dynamic and ridge patterns is displayed best in the 500-hPa heights (Fig. 3.9a), but is represented to some degree in the derecho mean direction of propagation (Fig. 3.9b), and in the 500-hPa wind speeds (Fig. 3.9c). The distribution of these attributes among the zonal flow pattern tend

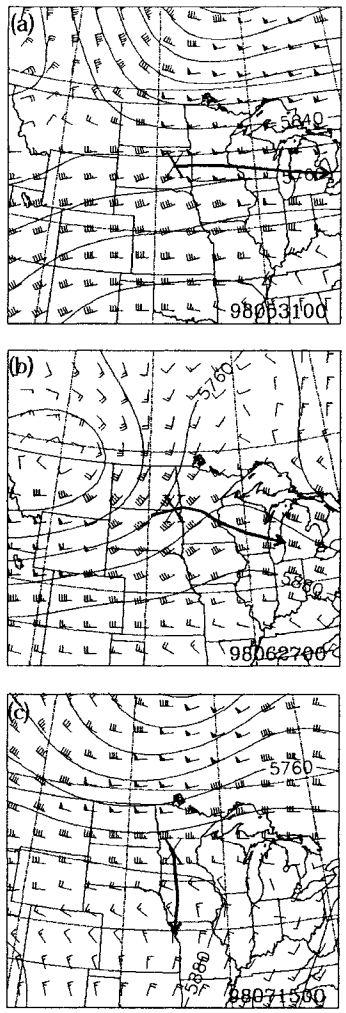


Fig. 3.8. Examples of 500-mb geopotential heights and winds from hybrid patterns. (a) An example of an upstream-trough/zonal pattern hybrid. (b) An example of an upstream-trough/ridge pattern hybrid. (c) An example of an unclassifiable hybrid pattern. The approximate track of the derecho major axis is depicted by the arrow. The date and time (UTC) of each analysis (in YYMMDDHH format) is displayed in the lower right of each panel.

to be similar to those for the ridge pattern, which is a reflection of their occurrence almost entirely in the warm-season. The existence of these other patterns and the variability within each pattern shows that the idealized dynamic and warm-season patterns discussed by Johns (1993) only depict a portion of the full spectrum of the possibilities of large-scale flow patterns associated with the development of DCSs.

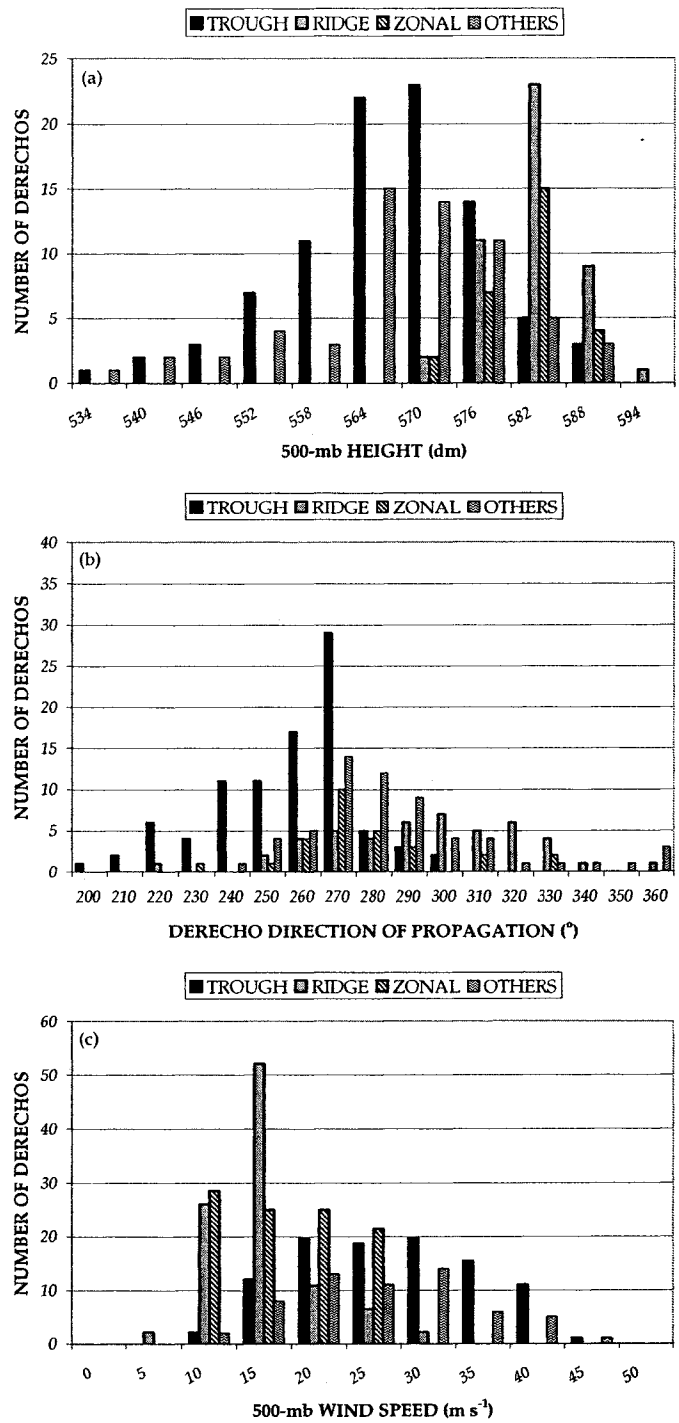


Fig. 3.9. Histograms of the (a) 500-hPa height near the location of derecho initiation, (b) the direction of propagation of the derecho, and (c) the 500-hPa wind speed near the location of derecho initiation, as determined from the Reanalysis data, for the cases that comprise the three main patterns and the 60 cases that are not classified into these main patterns (others).

It is believed that the documentation of the continuous nature of the flow patterns shown above lessens the importance of pattern recognition techniques in the forecasting of derechos. Additionally, it is beyond the scope of this paper to describe how often these patterns appear without DCS formation, which is an important ingredient in the use of pattern recognition. However, since 72% of the cases tend to show characteristics of only three broad, large-scale flow regimes, forecasters should be attuned to the potential physical mechanisms and the *multiscale* features that exist within these baseline large-scale patterns (e.g. the location of the right-entrance region of an upper-level jet streak or the location of the maximum in 850-hPa). An important supplement to this forecast process is the identification of ingredients that are associated with the development of the phenomenon in question (Johns and Doswell 1992). Thus, Chapter 4 explores the vertical structures of DCS environments using soundings, which seeks to identify environmental parameters associated with derechos.

Chapter 4: Analysis of Proximity Soundings

Chapter 3 builds on the literature that documents the large-scale flow patterns and features related to the development of derechos. This chapter describes the development of a proximity sounding data set and builds upon the work of Evans and Doswell (2001). The results detail the vertical distribution of the sounding parameters related to the large-scale patterns described in Chapter 3 and compare the results to past idealized numerical simulations. These observational results help fill the gap in our knowledge about derecho environments and provide a firm basis for conducting numerical simulations of DCSs.

4.1 Identification of proximity soundings

To build on the work of Evans and Doswell (2001) and to provide guidance for defining a representative vertical profile for initializing a numerical model, characteristics of derecho environments are determined from the National Weather Service radiosonde observations. Despite the problems of assuming that the radiosonde samples the pertinent environment (Brooks et al. 1994, Klimowski et al. 2003), the operational radiosonde data continues to provide the best source of simultaneous thermodynamic and kinematic measurements of the vertical structure of the entire troposphere that span several decades. This study focuses on CAPE and the vertical distributions of moisture and wind shear over the entire depth of the troposphere, which has not been examined in previous studies.

In this study, soundings that are within 300 km of the DCS leading edge in the downshear environment., no more than 80 km "north" of the derecho major axis and no more than 200 km "south" of the derecho major axis are considered candidates for

proximity soundings[1]. To remove soundings that have a significant chance of being contaminated, soundings that are too close to the convection (< 20 km) are not retained based on the simulations of Weisman et al. (1998) who shows that the initial condition may be significantly modified close to the convection. The wind components in the soundings are plotted in a coordinate system relative to the DCS motion such that the u and v components correspond to the direction parallel and normal to the derecho direction of propagation, respectively. Additionally, soundings that are obviously contaminated by convection are removed using hourly radar and surface data as guidance. Soundings that show an "onion" profile characteristic of the wake region on an MCS (Zipser 1982), that show deep saturated layers with lapse rates close to moist-adiabatic, or show rapidly increasing moisture content and potential temperature in upper levels (indicating a potential rise through convective cloudiness) are some of the signs that the sounding is contaminated. Soundings that sample convective outflows or drylines in low levels, but appear uncontaminated otherwise, also are discarded. Finally, only soundings that have mandatory and significant level wind data up to at least 10 km are retained. Out of the 230 candidates for proximity soundings, this procedure eliminates 62 soundings, which leaves 168 proximity soundings that approximate the environmental conditions in the DCS inflow environment.

4.1.1 Grouping the soundings by the derecho lifecycle

As in Evans and Doswell (2001), the soundings are first grouped relative to the phase of the derecho lifecycle to determine the differences in the initiation, mature, and decay environments. Similar to the methodology outlined in chapter 3 for the

[1] These are arbitrary guidelines that attempt to ensure that inflowing air reaches the convection no more than a few hours after it is sampled by the radiosonde.

normalization of the flow patterns, the sounding times are normalized relative to the duration of the event to help preserve consistent beginning, mature, and decay environments from case to case. If $t_{obs} \leq 0$, it is defined as a "beginning" sounding, signifying the developing stage of the derecho. If $0.0 < t_{obs} \leq 0.5$, it is defined as "mature" sounding, and if $t_{obs} > 0.5$ it is defined as a "decay" sounding. This method identifies 38 beginning, 52 mature and 78 decay soundings.

4.1.2 Grouping the soundings by synoptic-scale forcing

One of the benefits of grouping the soundings by some measure of the large-scale forcing for upward motion is to differentiate between serial (typically strong forcing) and progressive (typically weak or moderate forcing) derecho environments, which can help identify the relative importance of the physical mechanisms between the two types of events. In addition, this grouping helps to define the derecho environments that can be best represented in idealized numerical models.

The classification of derecho environments in the literature has typically been subjective and based on arbitrary criteria. JH87 uses a threshold 12-h, 500-mb height fall prior to derecho initiation to discriminate the strong trough from the weak trough events. This leads to the definition of the "warm season" and "dynamic" patterns outlined in Johns (1993) (Fig. 2.3). In addition to these patterns, Evans and Doswell (2001) subjectively define a "hybrid" pattern that displays attributes of both patterns. In this study, the soundings are grouped according to large-scale forcing using a semi-objective method. Instead of the 500-mb trough amplitude, this study uses the 500-mb Q-vector divergence field ($\nabla \bullet \mathbf{Q}$) as identified in the 2.5° grids produced by the NCEP/NCAR Reanalysis data set (Kistler et al. 2001). Q-vectors and their divergence provide a

convenient and accurate method of quickly diagnosing the large-scale forcing for upward motion on constant pressure surfaces (Bluestein 1993). There are several events that appear to have weak 500-mb troughs based on their amplitudes but have notable forcing for upward motion at the same level (possibly resulting from shear-vorticity advection that is not easily identifiable by trough amplitude). Likewise, not all 500-mb troughs that appear to have significant amplitude produce significant upward motion at 500-mb near the derecho initiation (at least on scales resolvable by the Reanalysis data set). The events with $\nabla \bullet \mathbf{Q}$ minima within 500 km of the derecho initiation point (the origin of the grid) $\leq -10 \times 10^{-16}$ kPa m^{-2} s^{-1} are defined as "strong forcing" events. The events with $\nabla \bullet \mathbf{Q}$ minima $\geq -5 \times 10^{-16}$ kPa m^{-2} s^{-1} are defined as "weak forcing" events. Those cases in between are defined as "moderate forcing" events. Using this method, the number of observations defined as weak, moderate, and strong forcing events is 37, 27, and 27, respectively (only the 91 beginning and mature soundings are used in this grouping since it will be shown that the decay soundings contain many statistically significant differences).

Although the above thresholds for $\nabla \bullet \mathbf{Q}$ are entirely arbitrary, it is found that these values provide groupings that are consistent with a subjective assessment of the large-scale forcing. This is supported by the fact that all of the 37 weak-forcing soundings are confined to the months of May-Aug. while only 9 of the 27 strong-forcing soundings occur during these months (Fig. 4.1). All but three of the moderate-forcing soundings occur in the warm season.

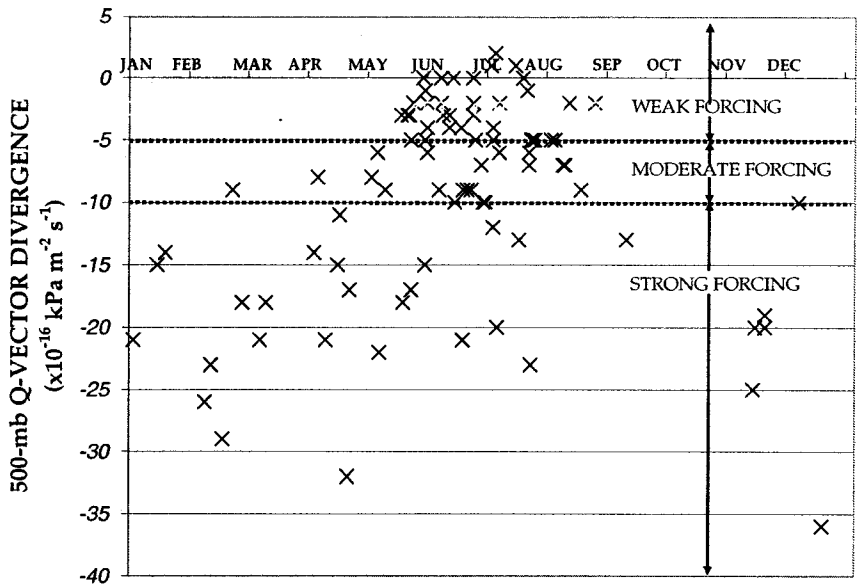


Fig. 4.1. The distribution of the mean 500-mb Q-vector divergence (scaled by 10^{16} kPa m^{-2} s^{-1}) versus day associated with the 91 beginning and mature proximity soundings. The thresholds for defining the forcing stratification are shown by the dashed lines.

4.2 Results

4.2.1 lifecycle stratification

The most statistically significant difference[2] in the CAPE distributions is between the beginning and decay soundings (Fig. 4.2). The mean CAPE drops from 2742 J kg^{-1} for the beginning soundings to 1451 J kg^{-1} for the decay soundings. Also notice that 90% of the beginning soundings have CAPE above 1000 J kg^{-1}, whereas 40% of the decay soundings have CAPE below 1000 J kg^{-1}. Large amounts of instability are frequently found in the initial environments as nearly 50% of the beginning soundings have CAPE above 2500 J kg^{-1}. This suggests that a decrease in instability is potentially a significant factor in the demise of DCSs.

[2] Differences between the various subsets are tested for statistical significance using a two-tailed student's t-test based on the sample means and standard deviations (Wilks 1995). Differences are considered significant if the chance that the two sample means originate from different distributions is ≥ 95%. The autocorrelation of the parameters has been tested and is found to be minimal, which gives confidence in allowing for the number of degrees of freedom = sample size. When appropriate, the estimate of the probability that the true population means are the same (p-value) is given in the text.

Past studies identify the environmental RH profile as a potentially significant factor in the development and maintenance of strong downdrafts within thunderstorms. Low environmental RH in midlevels aids the initiation of downdrafts by precipitation phase changes (Hookings 1965, Gilmore and Wicker 1998). However, Srivastava (1985) and Proctor (1989) suggest that higher environmental RH in the underlying layer of parcel descent supports the maintenance of strong downdrafts. Given a sufficiently steep lapse rate, the higher moisture content increases the virtual temperature of the environment, which leads to larger virtual temperature differences between the environment and the parcel.

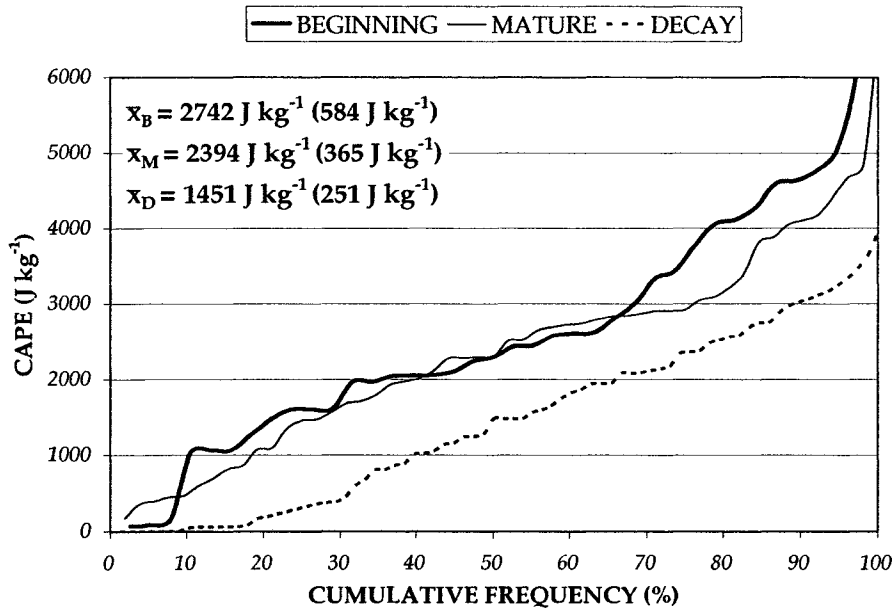


Fig. 4.2. The cumulative frequency distribution of CAPE (J kg^{-1}) for the beginning, mature, and decay soundings. The sample means for the beginning ($\bar{x}_B$), mature ($\bar{x}_M$), and the decay ($\bar{x}_D$) soundings, and their 95% confidence intervals (in parentheses), are shown in the upper left corner. $\bar{x}_D$ is significantly different than both $\bar{x}_M$ and $\bar{x}_B$ at the 95% confidence level.

The RH varies considerably during all stages of the DCS lifecycle, but insight is gained by examining the median profiles. The largest differences are between the beginning and mature soundings and are statistically significant in the 1.0-2.5-km layer. The vertical difference in median RH is largest for the mature soundings with median

values near 85% at 1 km that drop to 42% near 3.5 km (Fig. 4.3a). This suggests that DCSs tend to mature as they move into moister low-level environments, while still maintaining relatively dry conditions above 3 km. This result is in general agreement to Srivastava (1985) and Proctor (1989) and suggests that relatively dry midlevels combined with low-level moistening ahead of a developing MCS signals the increasing potential for downdraft and strong surface wind production.

Results further show that the low-levels (0-2 km) tend to dry somewhat toward decay, which reduces the vertical RH gradient and is likely a factor in the reduced CAPE for the decay soundings (Fig. 4.2). However, these differences are not large (the smallest p-value at any level below 2 km is 0.18 between the mature and decay soundings), which implies that a relatively drier low-level environment ahead of a mature DCS often does not signal its decay.

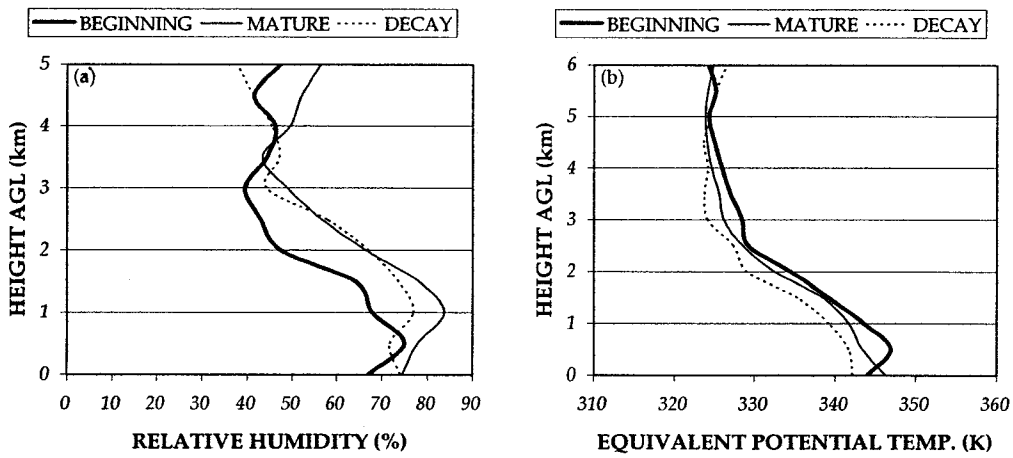


Fig. 4.3. Vertical profiles of (a) median RH and (b) θ_e for the beginning, mature, and decay sondings. The beginning and mature RH profiles are statistically different at the 95% confidence level between 0.75 and 3 km. There are no statistically significant differences in the θ_e profiles (p-values are > 0.1).

The beginning and mature soundings both display a vertical decrease in the median equivalent potential temperature (θ_e) of > 20 K (Fig. 4.3b). Overall, the vertical

decreases in θ_e appear to be even larger for DCSs than for those reported for strong downdrafts within more isolated convective cells by Atkins and Wakimoto (1991) (the next section shows that the more weakly-forced events are largely responsible for this large convective instability). Note that the low-level inversion in the median θ_e profile for the beginning soundings is related primarily to the occurrence of 1200 UTC soundings in the data set, but also represents events that develop north of a low-level thermal boundary (Fig. 4.3b). The fact that this inversion is not evident for the mature soundings indicates that the systems tend to move toward the warm sector as they mature (JH87). The low-level θ_e decreases toward decay (Fig. 4.3b), but the statistical differences are somewhat less than what is typically considered to be significant (p-values range from 0.08-0.3 depending on the specific vertical level). This suggests that low-level θ_e, along with the low-level RH, is not necessarily a useful indicator of DCS decay, which appears to be the case for MCSs in general (Gale et al. 2002).

The mean hodographs display a unidirectional shear profile ("straight-line") and significantly weaker deeper-layer shear for the decay soundings (Fig. 4.4). In many events, this decrease in deep-shear is the result of the propagation away from the mid-to-upper-level jet. The mean 0-5-km shear drops from over 20 m s^{-1} for the beginning and mature soundings to 16.6 m s^{-1} for the decay soundings (see Table 4.1). Likewise, the mean 5-10-km shear drops from 14.3 m s^{-1} for the beginning soundings to 11.6 m s^{-1} for the decay soundings. The mean low-level shear (0-1-km and 0-2.5-km) shows no significant differences in the DCS lifecycles. Gale et al. (2002) found similar results for general warm-season MCSs. This adds observational support to the conclusions of Coniglio and Stensrud (2001) that DCSs can be maintained by system-scale circulations

that are favored by deep-tropospheric shear and convergence along the gust front (Shapiro 1992, Moncrieff and Liu 1999).

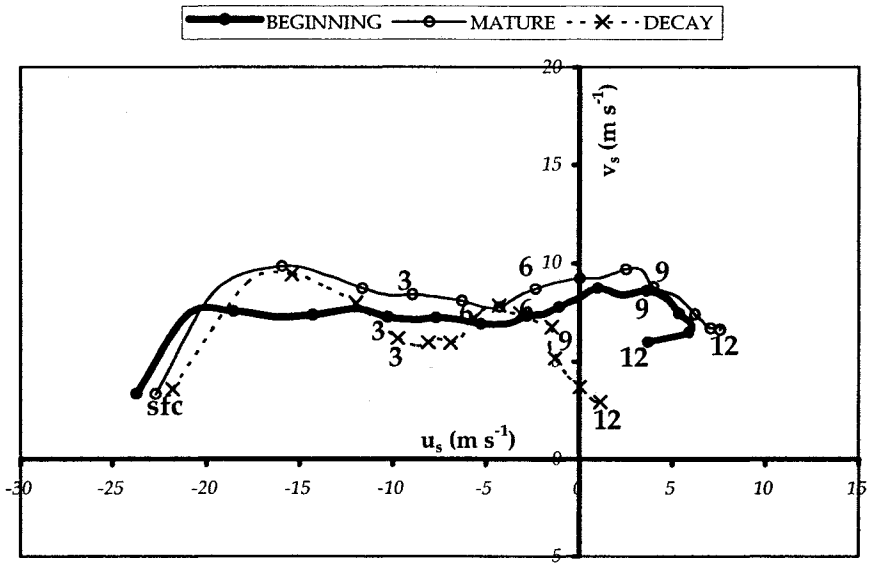


Fig. 4.4. Mean hodographs for the beginning, mature, and decay soundings. Prior to averaging, the wind components (u,v) in each sounding are represented in a coordinate system with the tip of the mean MCS motion vector (u_s,v_s) at the origin. The mean winds are calculated every 0.5 km above ground level (AGL), are plotted every 1 km AGL, and are labeled every 3 km AGL. Mean shear values related to the mean hodographs are given in Table 4.1.

It should be noted that some of the more weakly forced events do show a decrease in the low-level shear toward decay, and thus, the persistence of the overall mean low-level shear toward decay is ascribed to the strong low-level shear observed for the strongly-forced soundings (shown in the next section). Similarly, examination of Fig. 4.4 suggests that the low-level storm-relative inflow appears to persist toward decay. However, the length of the hodograph for the beginning and mature soundings is ascribed to the strong low-level winds observed in the strongly forced soundings (also shown in the next section). The storm-relative inflow does show a decrease toward decay for the more weakly forced events (not shown). However, the sample sizes are insufficient to

break down each lifecycle classification by forcing regime and thus, the significance of these details can not be determined with the current data set.

Table 4.1. Mean 0-1-, 0-2.5-, 0-5-, and 5-10-km shear vector magnitudes (m s^{-1}) for the lifecycle stratification (beginning, mature, decay) and the forcing stratification (strong, moderate, weak). Shaded cells in the lifecycle stratification indicate that the sample mean is statistically different than the sample mean for the decay soundings at the 95% confidence level. Shaded cells in the forcing stratification indicate that the sample mean is statistically different than the sample mean for the weak-forcing soundings at the 95% confidence level.

	0-1 km	**0-2.5 km**	**0-5 km**	**5-10 km**
BEGINNING	8.7	14.1	20.4	14.3
MATURE	10.6	15.0	20.3	13.6
DECAY	9.9	13.2	16.6	11.6
STRONG	15.3	18.3	23.8	15.6
MODERATE	8.4	15.1	19.0	11.3
WEAK	6.8	11.4	18.8	14.4

4.2.2 Forcing stratification

The cumulative frequency distributions of CAPE (Fig. 4.5) show a distinct separation between the strong-forcing (SF) soundings and the moderate-forcing (MF) and weak-forcing (WF) soundings (again, only the soundings with $t < 0.5$ are included). All but two of the WF soundings have CAPE above 1000 J kg^{-1}, while almost 50% of the SF soundings have CAPE below this amount. Much larger values of instability is found for the WF and MF soundings with almost 50% having CAPE above 2700 J kg^{-1}. Soundings with these values of instability are rare under strong forcing, which appears to be largely due to their prevalence during the cold season, but also could be due to the tendency for high-CAPE/strong-shear environments to support supercell modes (Johns and Doswell 1992).

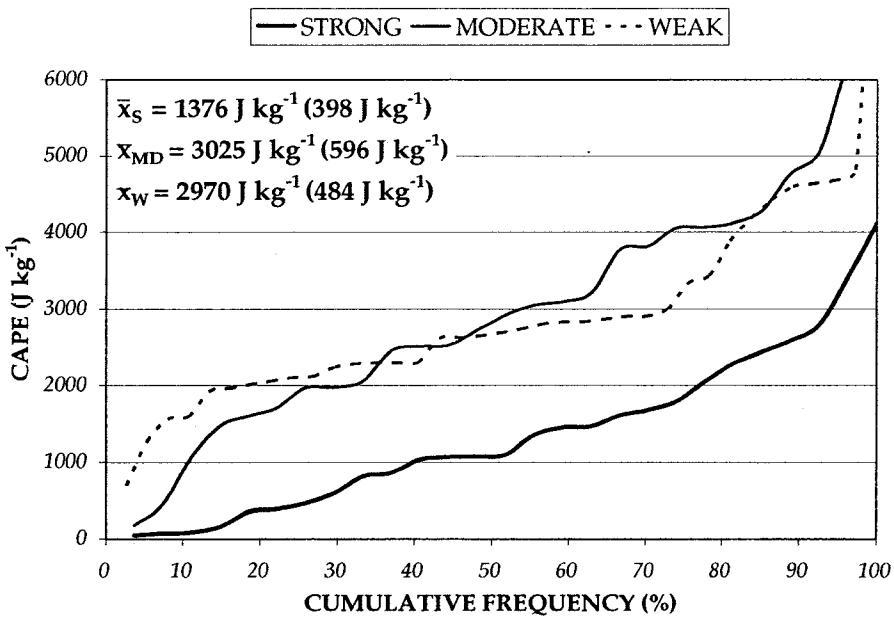


Fig. 4.5. The cumulative frequency distribution of CAPE (J kg^{-1}) for the strong, moderate, and weak-forcing soundings. The sample means for the strong ($\bar{x}_S$), moderate ($\bar{x}_{MD}$), and the weak ($\bar{x}_W$) forcing soundings, and their 95% confidence intervals (in parentheses), are shown in the upper left corner. $\bar{x}_S$ is significantly different than both $\bar{x}_{MD}$ and $\bar{x}_W$ at the 95% confidence level.

As for the examination of RH among the various DCS lifecycles, significant differences are found in the median profiles (Fig. 4.6). For the SF soundings, the median RH reaches a maximum near 90% at 0.75 km and drops to a local minimum of 38% at 4 km. As discussed previously, this large vertical RH gradient translates into a significant potential for downdraft production. It also has been recognized that a reduction in the environmental lapse rates within the downdraft layer lessens the potential for maintaining downdrafts (Hookings 1965, Srivastava 1985, Proctor 1989). Relatively small environmental lapse rates are observed for the SF soundings (compared to the MF and WF soundings), which is reflected in the smaller CAPE values (Fig. 4.5) and from the relatively small vertical decrease in median θ_e for the SF soundings (Fig. 4.6b). This suggests that the dramatic vertical RH gradient observed for the SF soundings, and the associated increased potential for downdraft production (Proctor 1989), perhaps counter a

decreased potential for downdraft production associated with the smaller lapse rates. A dramatic vertical RH gradient is, therefore, a possible reason for why derechos can occur with low CAPE.

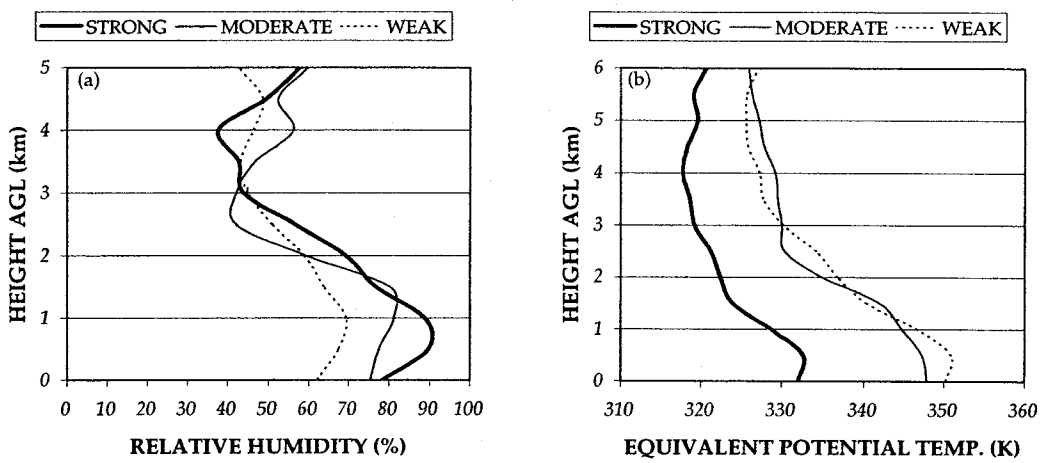


Fig. 4.6. As in Fig. 4.3, except for the strong, moderate, and weak forcing soundings. The strong and weak forcing profiles are statistically different at the 95% confidence level between the surface and 1.25 km. The strong forcing θ_e profile is significantly different from the moderate and weak forcing θ_e profiles at the 95% confidence level at all vertical levels (0-6 km).

While the vertical decrease in median RH becomes progressively smaller for the MF and WF soundings (Fig. 4.6a), the vertical decrease in θ_e becomes progressively larger, with the median profile showing a vertical decrease of ~24 K from the low to midlevels (Fig. 4.6b). This affirms that WF events tend to have large values of convective instability in the environment.

Unlike the lifecycle stratification, the most significant differences in shear are found in the low-level shear parameters (Fig. 4.7 and Table 4.1). For example, the mean 0-2.5-km shear drops from 18.3 m s^{-1} for the SF soundings to 11.4 m s^{-1} for the WF soundings (Table 4.1). The shear component normal to the DCS motion vector in the lowest 2 km (which is generally parallel to the squall line) (Fig. 4.7) contributes a significant amount

to this large mean low-level shear for the SF soundings (Table 4.1) and likely is tied to the strong low-level and upper-level jets that frequently occur in this forcing regime (Uccellini 1980) (Fig. 3.2). Mean 5-10-km shear values of 11-16 m s^{-1} with a large range of values (3 m s^{-1} - 40 m s^{-1}) show that the shear very often extends throughout the depth of the troposphere, regardless of the forcing regime.

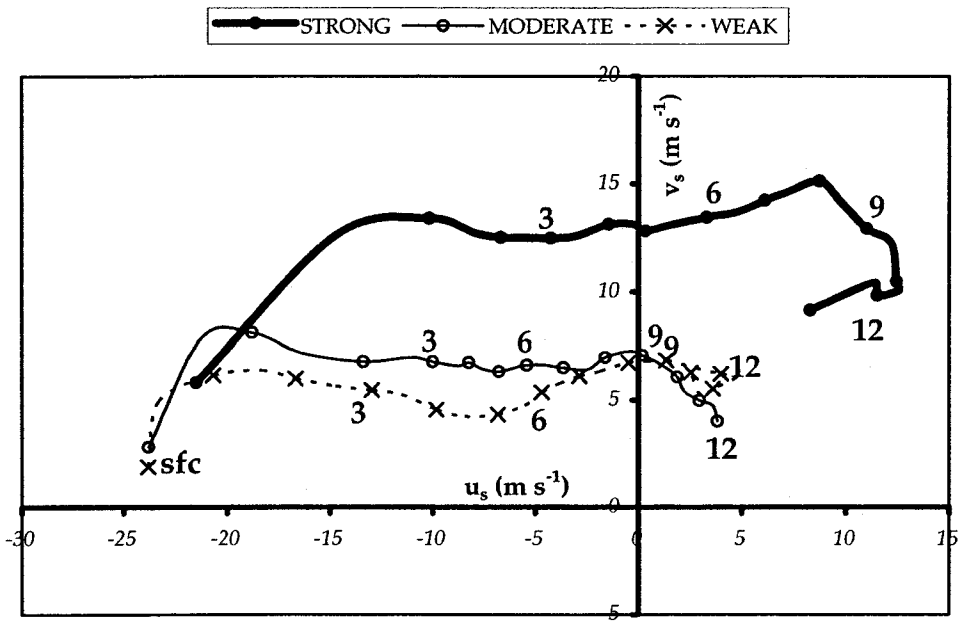


Fig. 4.7. As in Fig. 4.4, except for the strong, moderate, and weak forcing soundings. Mean shear values are given in Table 4.1.

Strong near-surface inflow is noted among all three forcing regimes. The mean 0-3 km storm relative wind speed is largest for the WF soundings with a magnitude of 19.5 m s^{-1}. This speed decreases to 18.1 m s^{-1} for the MF soundings and 16.6 m s^{-1} for the SF soundings. The variations in vertical shear results in differences in the depth and orientation of the inflow layer. For the SF soundings, the mean top of the inflow layer (u_s=0) is found near 5 km and the 0-3 km mean storm-relative wind vector is ~140°. A positive u_s above 5 km combined with a strong mean-wind component normal to the DCS

motion vector likely contributes to the parallel or leading stratiform precipitation (Parker and Johnson 2000) that is usually observed among these events.

For the MF and WF soundings, the mean top of the inflow layer increases to between 8 and 9 km. The rearward flow in midlevels likely contributes to the frequent appearance of these events as asymmetric, trailing-stratiform MCSs (Houze et al. 1989; Parker and Johnson 2000). In addition, the relative low-level inflow originates from a direction that is at a large angle (~160°) to the mean DCS motion vector. This reveals that the system ingests the high-θ_e low-level air in the downshear environment (Fig 4.7). The existence of mean 0-5-km shear of 18-20 m s^{-1} produces considerably weaker midlevel (5-7 km) storm relative flow (Fig. 4.7). This supports one of the key findings of Evans and Doswell (2001) that DCSs with weak synoptic-scale forcing tend to form in such environments that support the fast forward-propagation of the cold pool.

4.2.3 Comparison to simulations

Using a horizontally homogeneous cloud-scale numerical model, W93 produces a comprehensive set of simulations of convective systems that include structures resembling observed DCSs. One of the goals of W93 was to identify the minimum thresholds of CAPE and shear within the idealized simulations that produce these structures and to compare them to environmental conditions associated with observed severe long-lived bow echoes. The present comprehensive observational data set affords a detailed comparison of this type and is presented in light of its relevance to forecasting severe, long-lived convective systems.

W93 subjectively defines the structure of the simulated convective systems into three main categories. The first category includes systems with weak cells tens of km behind

the leading edge of the gust front, in which structures resembling strong, long-lived bow echoes do not develop (W). The second category includes strong, long-lived bow echo structures with a pronounced rear-inflow jet and cyclonic vortices along the ends of the bow (B). The third category includes strong, isolated cells, some supercells, scattered along the gust front, with no indications of larger-scale rear inflow that comprise the bow echo cases (S). A fourth intermediate category is defined (I) that contains attributes of both the weak and bow-echo cases. He finds that the well-defined bow echo simulations are generally restricted to environments with shear greater than 20 m s^{-1} and are favored if this shear is entirely confined to the lowest 2.5-km (Fig. 4.8).

To compare the present observations to these simulations, WSR-88D mosaics at 2-km or 4-km resolution or, when available, the level II WSR-88D data, are used to define a typical convective structure for each event that has a beginning or mature proximity sounding. Due to the lack of sufficient radar data for the majority of the events, it is possible to define adequately a convective structure for only 53 of these events. DCSs that contain well-defined bow echoes for at least a 1-h period and resemble the "B" simulations in W93 are identified. In addition, DCSs that show either short-lived bow echoes, or none at all, and resemble the "W" simulations from W93 also are identified. Each case also is defined as having either elongated squall line characteristics with parallel or leading stratiform precipitation or as having characteristics more typical of trailing-stratiform MCSs.

The results show that the vast majority of the soundings that sample bow-echo squall lines or bow-echo MCSs have 0-2.5-km shear outside the range of values that produce the B simulations from W93 (Fig. 4.8a). In fact, 14 out of the 20 soundings that sample

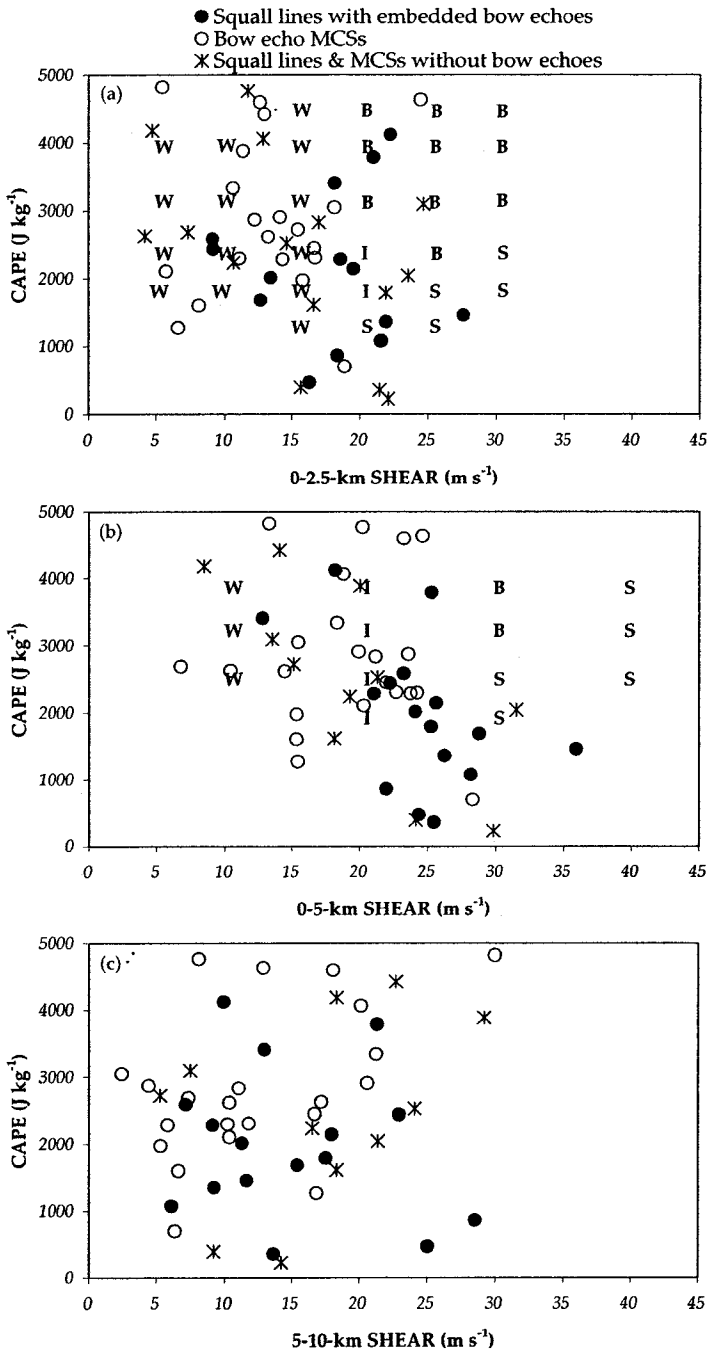


Fig. 4.8. Scatterplots of (a) 0-2.5 km, (b) 0-5 km, and (c) 5-10 km shear vector magnitudes (m s^{-1}) versus CAPE (J kg^{-1}) for those soundings in which the convective structure of the DCS is identified (see legend at top of figure). Results from Weisman's (1993) numerical simulations of convective systems also are shown in (a) and (b) (see his Fig. 24). The letters represent the convective structure of the simulated systems as defined by Weisman (1993) (see text for details).

bow-echo MCS environments (70%) have 0-2.5-km shear below 15 m s^{-1}. Most of the values from the observed bow-echo MCSs cluster around the shear environments that produce the "W" simulations (Fig. 4.8a), which typically do not represent the DCS structures observed in this study. This confirms the implication of Evans and Doswell (2001) that long-lived bow echoes can and often do occur in low-level shear less than that suggested by the W93 simulations and that *the low-level shear may not be useful in forecasting long-lived bow echo structures in many situations.* The results from section 4a, that show no significant changes in low-level shear among the three phases of the DCS lifecycle, add weight to this conclusion. It should be noted that more of the observed soundings have shear values that support at least some bow-echo structures in the simulations (the "I" simulations) when the shear layer is extended to 5 km above ground (Fig. 4.8b). Only 4 out of the 20 bow-echo MCSs have 0-5 km shear less than 15 m s^{-1}. Therefore, the presence of moderate to strong unidirectional shear in the 0-5-km layer appears to be a better predictor of the potential for severe MCS structures than the low-level shear. It should also be noted that the simulations do not represent the several observed bow-echo squall lines that occur with strong low-level shear and CAPE <1000 J kg^{-1}. These cases appear to be supported more from stronger synoptic-scale forcing that is not well represented in the idealized simulations.

4.3 Discussion

WR update their results to include simulations with shear in a layer up to 10 km deep (the W93 simulations only included shear in the lowest 5 km). The simulations that include shear above 5 km do not develop long-lived bow-echo structures (they are described as either upshear-tilted multicellular systems or systems composed of isolated

cells and/or embedded supercells). However, the mean 5-10 km shear observed among the well-defined bow-echo events is approximately 14 m s^{-1}, and is as large as 30 m s^{-1} (Fig. 4.8c). This shows that idealized numerical simulations appear to have difficulty reproducing DCS events within deep-shear environments and further emphasize some disparities between observations and the idealized models. Simulations using the CAPE, shear, and moisture values of observed DCSs and the associated non-homogeneous large-scale flow patterns identified in this study need to be produced to help reconcile these disparities in observations and idealized models and to provide improved information to forecasters. The following chapter explores a set of 2-D and 3-D numerical simulations that are used to develop alternative ideas for how strong convective systems can be maintained in suboptimal low-level shear conditions not discussed in WR.

Chapter 5: Numerical Simulations

Chapter 4 shows that strong, long-lived convective systems tend to develop and persist within environments with significantly drier mid-levels, weaker low-level wind shear, and wind shear over deeper layers; an environment that has not been highlighted in past idealized numerical simulations of convective systems. This chapter presents a way that the unidirectional shear above the cold pool through most of the depth of the troposphere can affect the strength and maintenance of the convective systems through a set of idealized numerical modeling experiments. A discussion of the results follows a description of the model configuration and the design of the experiments.

5.1 Numerical Model

The model of choice is the National Severe Storms Laboratory Collaborative Model for Multiscale Atmospheric Simulation (NCOMMAS) (Wicker and Wilhelmson 1995). NCOMMAS is designed to study convective storms at high space and time resolution and is very similar to the model developed by Klemp and Wilhelmson (1978). The differential equations describing the evolution of momentum, heat, and moisture variables are solved on an Arakawa-C grid with vertical stretching to allow higher resolution in low-levels. NCOMMAS retains the time-splitting scheme of Klemp and Wilhelmson (1978) to represent sound waves (and retain full compressibility), but improves on the combination of accuracy and stability by using a third-order Runga-Kutta time differencing scheme in combination with a fourth-order spatial discretization for the spatial variables (Wicker and Wilhelmson 2002). Subgrid-scale horizontal and vertical mixing is parameterized using a deformation-based formulation for the eddy

mixing coefficient (K_m) in the flux approximations (Wicker and Wilhelmson 1995). The only condition on the lower (and upper) boundary is that the normal velocity component decrease to zero. Lateral boundaries are open for disturbances to pass through, but a Rayleigh damper is used at the upper boundary to control the energy from spurious gravity waves. Microphysics options include the Kessler-type warm-rain parameterization and 3-class (ice, snow, graupel/hail) ice-scheme in the 3-D version of the model (Gilmore et al. 2004), which is based on the Lin et al. (1983) scheme. Coriolis forcing acts on the horizontal wind components with a constant parameter of 10^{-4} s^{-1} (see the appendix for a detailed list of the key parameters used in the simulations).

Similar to the experiments presented in W93 and WR, a horizontally homogeneous initial condition is used to represent the environment in all sets of experiments. While recent numerical simulations (Bernardet and Cotton 1998, Coniglio and Stensrud 2001, Richardson 2002) and recent specialized observations from the BAMEX field program (Davis et al. 2004) suggest the importance of substantial mesoscale variability in the environment, the goal of this study is to provide alternative simulations and interpretations within the context of the model designs presented in W93 and WR. The intent is to describe under-emphasized interpretations of MCS behavior from these class of simulations, thus the choice of retaining horizontal homogeneity.

5.2 Configuration of the 2-D dry simulations

The primary exploration into the role of mid- to upper-level shear is accomplished with the use of a dry, 2-D version of NCOMMAS initialized with neutral stability and the potential temperature set to 300 K to simulate idealized density currents in shear flow. The goal is to examine the basic dependence of lifting along a propagating density

current on the vertical wind shear above the density current depth. The domain stretches 240 km in the horizontal and 16 km the vertical and uses 961 by 65 grid points, such that $\Delta x=\Delta z=250$ m. A density current is introduced with a cooling function added to the potential temperature tendency of the form $A\left(\cos(\frac{\pi r}{2})\right)^2$, where A is a constant controlling the maximum magnitude of the cooling and $r=\sqrt{\left(\frac{(x-x_c)}{x_r}\right)^2+\left(\frac{(z-z_c)}{z_r}\right)^2}$, which controls the radius of influence of the cooling. For the dry simulations, A=-0.015 K s^{-1}, x_c=120 km, z_c=2 km, x_r=10 km, and z_r=2 km. A is held constant throughout the 5400 s simulation in order to maintain a source of cold air. As shown later, this function produces a quasi-steady propagating density current with surface θ perturbations of 6-8 K, which is typical of atmospheric cold pools (Evans and Doswell 2001).

For the entire set of 2-D dry simulations, the shear in the lowest 2.5 km is set at 12 m s^{-1} and the shear in the 2.5-5 km layer is set at 8 m s^{-1}, giving a bulk 0-5 km shear of 20 m s^{-1}. As shown in Chapter 4, these values of shear are close to the mean and median values among the groupings of derecho proximity soundings. The shear in the 5-10 km layer is then systematically varied from 0 to 30 m s^{-1} in 5 m s^{-1} increments (Fig. 5.1), which represents most of the observed range of upper-level shear (Fig. 4.8). The winds are held constant from 10 to 12 km and then decrease to a speed of 5 m s^{-1} at the top of the model (16 km) to represent the decrease in wind speeds that are typically observed above the tropopause. These simulations are designed to test the hypotheses of Shapiro (1992) that increasing the shear throughout the depth of the troposphere can increase vertical parcel displacements despite decreasing the strength of the forced updraft along

the density current, and that this process can be accomplished entirely by increasing the shear above the cold pool.

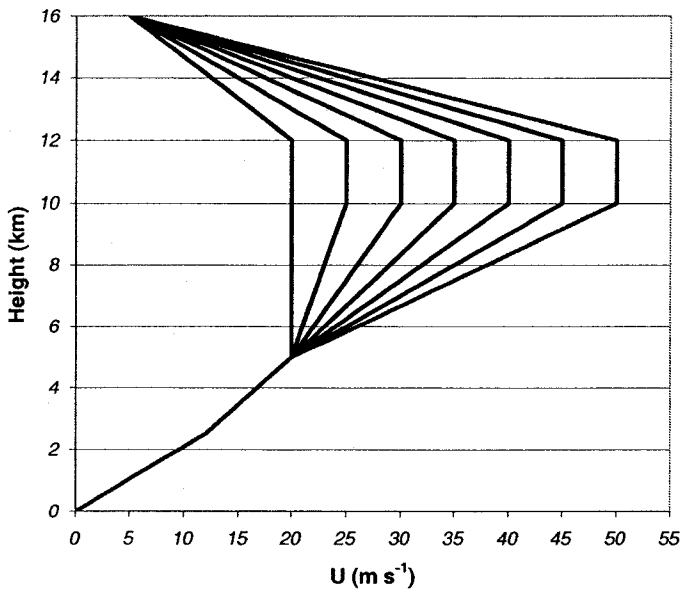


Fig. 5.1. Initial U profiles for the 2-D dry simulations.

5.2.1 Trajectory calculations

Since the cold air is introduced at a much shallower depth than the balanced depths for conservative, bounded density currents, steadiness to the density current structure is not guaranteed by the initial condition (Xue et al. 1997). Indeed, transience is shown to occur for some of the simulations, but the design ensures that the cold air remains to somewhat shallow depths that resemble atmospheric density currents. Although the bulk properties for this type of flow can be viewed from the time-averaged flow fields, as in Xue et al. (1997), the occurrence of transience leads us to calculate the vertical displacements numerically using a series of trajectory calculations rather than using the stream function for the time-averaged flow.

The forward-in-time air parcel trajectories are calculated based on the semi-Lagrangian methods outlined in Staniforth and Cote (1991) and Seibert (1993). This procedure is based on the numerical integration of the trajectory equation,

$$\frac{d\vec{r}}{dt} = \vec{V}(x,z,t) \tag{5.1}$$

where $\vec{r}$ is the position vector and $\vec{V}$ is the time-dependent velocity vector. The procedure to solve eq. (5.1) can be demonstrated in one dimension as

$$\int_t^{t+\Delta t} \frac{dx}{dt} dt = \int_t^{t+\Delta t} u(x,t)dt, \tag{5.2}$$

which, through the mean value theorem, gives the approximation,

$$x(t+\Delta t) = x(t) + \Delta t\bar{u} \tag{5.3}$$

where $\bar{u}$ is some averaged value of u in time Δt. If we let $\alpha = x(t+\Delta t) - x(t)$, the distance the fluid parcel is displaced in x in time Δt, then we can define $\bar{u} = u(x+0.5\alpha, t+0.5\Delta t)$ to be the value of u halfway along the trajectory. Eq. (5.3) then becomes

$$\alpha = \Delta t\, u(x+0.5\alpha, t+0.5\Delta t). \tag{5.4}$$

Given an initial guess for α and an approximation for $\bar{u}$, eq. (5.4) is solved iteratively at each time step, k, until $\alpha^{k+1} - \alpha^k$ is arbitrarily small. A third order Lagrange interpolating polynomial is used to interpolate in time to find $u(x,t+0.5\Delta t)$ at grid points needed for the calculation of the trajectory. Once u is interpolated in time, another third order Lagrange polynomial is used to find an approximation for $u(x+0.5\alpha, t+\Delta t)$ in space.

The solution for the displacement in the second dimension is found in an analogous manner once the 2-D interpolations are found (Press et al. 1986).

5.3 Configuration of the 2-D and 3-D moist simulations

A set of three 2-D and three 3-D simulations that include stratification and moist microphysics are produced in an attempt to show consistency between the behavior of the dry simulations and more complex simulations and for longer integration times (6 h). For the 2-D runs, Δz remains 250 m, but Δx is increased to 500 m. The domain now stretches 300 km in the x-direction giving 601 grid points. Moist processes are represented with a liquid only Kessler-type scheme (Soong and Ogura 1973, Gilmore et al. 2004).

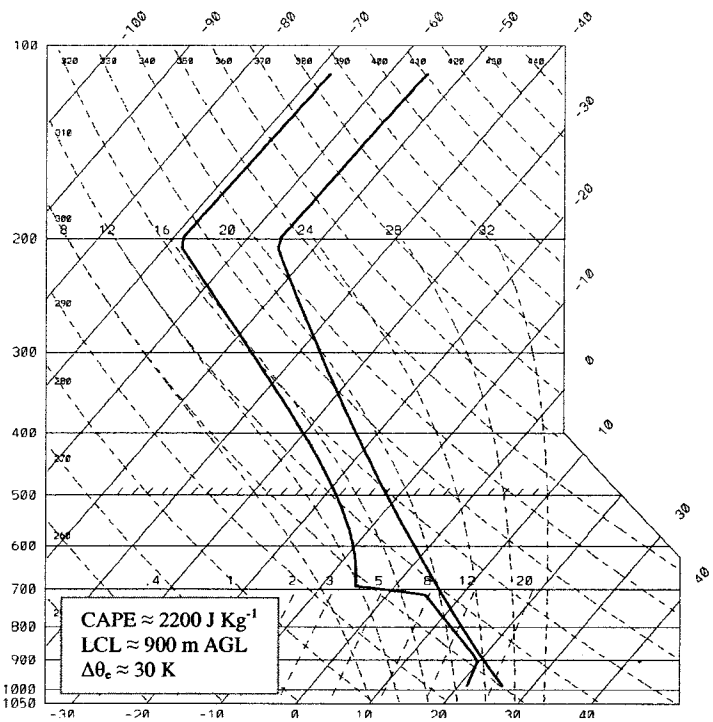


Fig. 5.2. Initial sounding used in the 2-D moist simulations.

The initial temperature and moisture profiles are similar to the Weisman and Klemp (1982) sounding, except for drier conditions above 3 km (Fig. 5.2). As for the dry runs, a cooling function is used to introduce a propagating cold pool. However, in the 2-

D moist runs the purpose of the cooling function is solely to initiate convection and, therefore, the cooling function decreases linearly to zero from 900 s to 1800 s. To test the hypotheses garnered from the dry runs, three wind profiles are used that vary the magnitudes of wind shear above a layer of 20 m s^{-1} over the lowest 5 km (Fig. 5.3). The profile that contains the values of shear closest to the median shear values in the observations contains 20 m s^{-1} of 0-5 km shear and 10-15 m s^{-1} of 5-10 km shear.

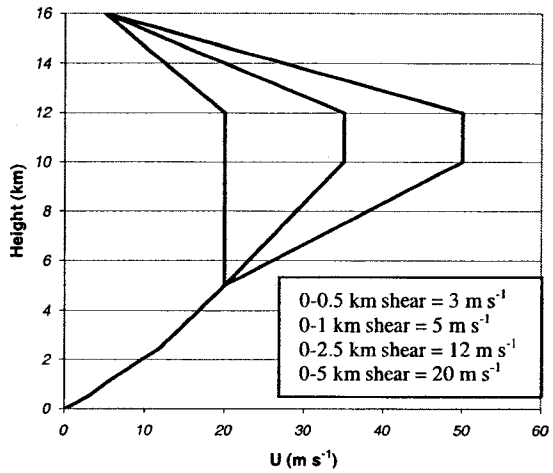


Fig. 5.3. Initial U profiles used for the moist simulations. The values of bulk shear in all the profiles (listed on the figure) correspond to the median values derived from the set of weakly forced soundings. The profiles that contains the values of shear closest to the median shear in the observations contains 20 m s^{-1} of 0-5 km shear and 10-15 m s^{-1} of 5-10 km shear.

For the 3-D runs, a 400 km by 400 km by 16 km grid is used with $\Delta x=\Delta y=2$ km. Although Bryan et al. (2003) show that interpretations of the convective system structure can be altered significantly with much higher resolution, these simulations are designed to be in the class of idealized simulations of W93 and WR, who used a grid with 1 km horizontal spacing[1]. A constant Δz of 250 m is used below 1 km and is then stretched to about 700 m at the top of the model domain at 16 km (giving 33 vertical grid points). In

[1] Weisman (1997) shows little difference in the convective structure and mean vertical flux characteristics for idealized simulations that use a horizontal grid resolution in the 1-2 km range.

an attempt to further increase the model realism, the 3-class ice scheme is used for the 3-D runs.

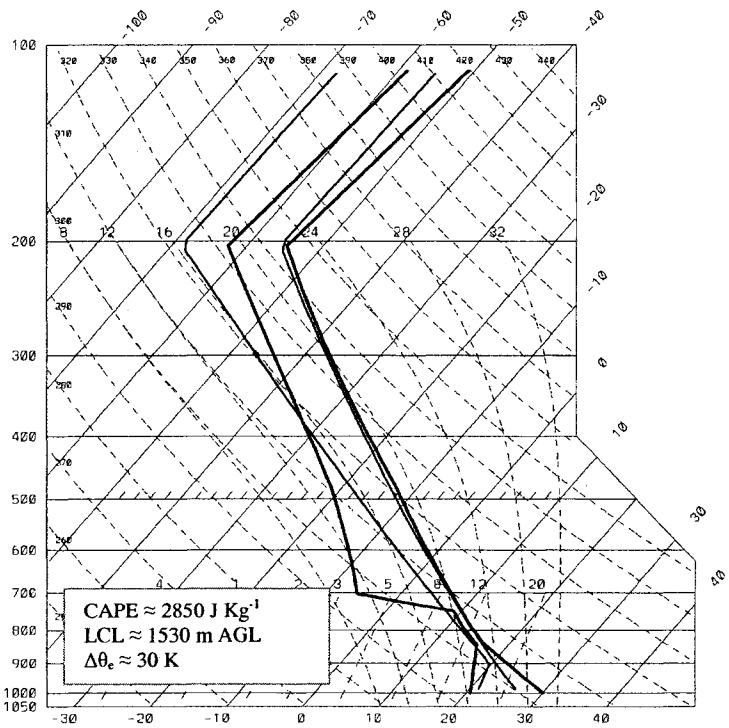


Fig. 5.4. The initial sounding used in the 3-D simulations (thick lines) compared to the Weisman and Klemp (1982) sounding (thin lines). The values of CAPE, lifting condensation level (LCL) and the maximum difference in θ_e between low and mid levels ($\Delta\theta_e$) in the profiles (listed on the figure) correspond approximately to the median values derived from the weakly forced soundings (see text for details).

A unique aspect of this study is that the observational analyses directly influence the choice of environments used for the initial conditions. Rather than use the Weisman and Klemp (1982) sounding, which appears to be too moist in mid and upper levels, an initial temperature and moisture profile is derived from a set of 28 derecho proximity soundings that were taken at either 1800 or 0000 UTC in weakly forced situations to ensure the representation of convectively-unstable conditions in low-levels (Fig. 5.4). The initial profile approximately preserves the median bulk shear in the 0-0.5, 0-1 and 0-2.5 (but distributes this shear unidirectionally). Additionally, the thermodynamic profile

approximately preserves the median values of CAPE (calculated using the most unstable 50-mb averaged parcel), lifting condensation level (LCL), and the maximum vertical difference in θ_e between low and mid levels (Fig. 5.4). The most apparent differences in this sounding and that used by Weisman and Klemp (1982) are the higher LCL and the drier conditions in mid-levels seen in the soundings based upon observations. The CAPE also is somewhat larger, but the drier mid-levels result in a much larger difference in the convective instability between the two soundings (see the appendix for a detailed list of the key parameters used to construct the initial sounding).

Since the initiation and maintenance of convection in cloud models is sensitive to the low-level moisture profile (Bryan and Fritsch 2000), a 1000 m deep layer of constant 93% RH is used in the 1000 m layer above the LCL in order to ensure the development and sustenance of the initial convection. Some researchers justify the saturation of the air above the LCL by assuming this profile represents the environment just prior to convective development that has been subject to low-level mesoscale lifting (Gilmore and Wicker 1998).

Instead of using a cooling function to initiate convection in the 3-D runs, warm potential temperature perturbations are used as in W93 and WR. A line of five uniformly-spaced elliptical thermal perturbations with a horizontal diameter of 10 km and a vertical diameter of about 1.5 km is used. The line is oriented in the y-direction and is centered at x=200 km and y=230 km. The perturbation amplitude is 2 K at the center of the thermal, with superimposed random perturbations no greater than 0.25 K, and decreases to 0 K on its outer edge. The model is integrated for 6 h to facilitate a

comprehensive comparison to observations in terms of the maintenance and mature structure of the convective systems.

The same set of four initial wind profiles used for the 2-D moist runs (Fig. 5.3) are used to produce a set of three 3-D runs. The first step in analyzing these simulations involves using several measures of system strength, including integrated rainfall and rainfall intensity, near-surface wind speeds, and maximum downdraft strength. In addition, measures of system structure, including the vertical orientation of the updrafts, the orientation of the updrafts relative to the gust front, and the structure of the simulated radar reflectivity structures, also are examined. This allows a n analysis of the basic shear dependencies of the system structures similar to what is presented in W93 and WR.

It should be noted that a direct comparison to the results of W93 and WR is problematic, largely because of the differences in the thermodynamic profile and the inclusion of ice-microphysics. The sensitivity of attributes of the simulations, particularly the characteristics of the cold outflow and precipitation distribution (Gilmore et al. 2004), likely have significant sensitivities to both of these changes and can alter substantially the interpretation of the simulated MCS strength and structure (the strength sensitivity to changes within the ice-microphysics scheme itself is illustrated briefly at the end of section 5.4). It is reiterated that the goal of this study is to provide an alternative viewpoint for the structure and maintenance of strong MCSs within the context of cloud-model simulations, but within an environment that attempts to increase the realism of past idealized simulations. While this framework allows a systematic determination of the effects of adding upper-level shear, future work will need to refine the relative

importance of the mid-level dryness and the ice-phase processes on the comparative conclusions to the past idealized simulations.

5.4 Results

5.4.1 2-D dry runs

For each case, the cooling function results in a region of negatively buoyant air that descends to the surface and spreads horizontally in both directions. The continuation of the cooling allows a density-current structure to develop by 1500 s in all of the simulations, that includes a frontal slope of 50°-60°, a reduced head in the turbulent region behind the gust front, and surface potential temperature perturbations of 6-8 K near the gust front. The convergence of the low-level inflow and the density current head produces a region of upward motion that slopes upshear in accordance with the slope of the density-current interface.

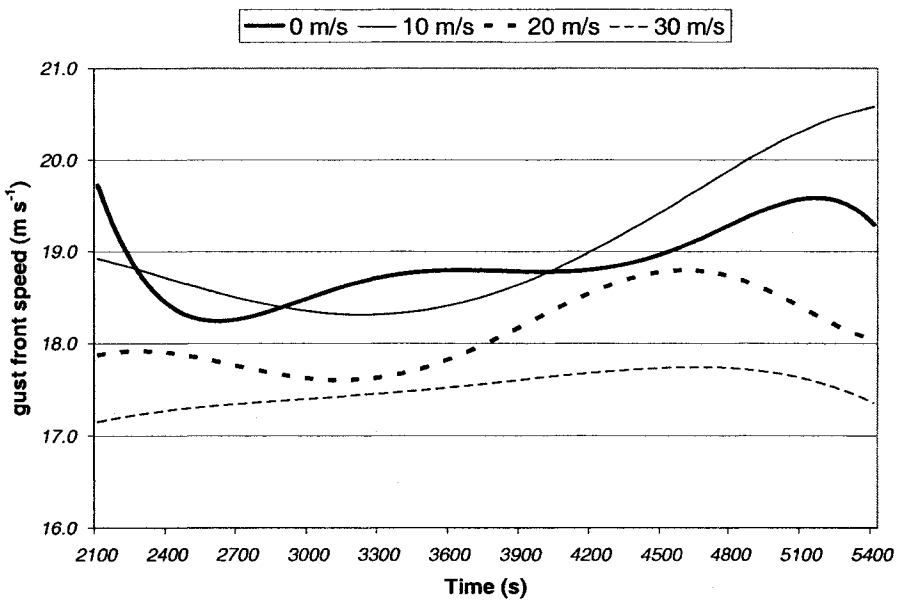


Fig. 5.5. The evolution of the gust front speed for the simulations with 0, 10, 20, and 30 m s^{-1} of shear in the 5-10 km layer.

The downshear edge of the density currents generally move at speed of 17-21 m s^{-1} among all of the simulations (Fig. 5.5). The lowered depth of the density current head for the stronger shear cases (Fig. 5.6) results in slower gust front speeds for the larger shear cases (Fig. 5.5) (Seitter 1986). The lowered depth of the current head results from a positive perturbation pressure in mid-levels; a feature that becomes important in controlling the behavior of the 2-D dry simulations as explained later.

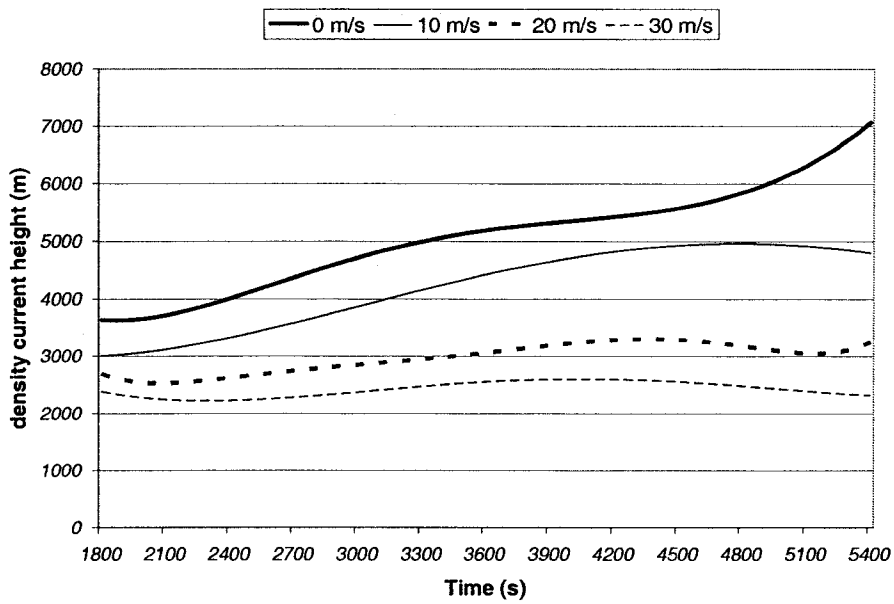


Fig. 5.6. The evolution of the density-current-head height for the 0, 10, 20, and 30 m s^{-1} shear simulations. The head height is estimated by finding the maximum height of the -1.0 K isotherm behind the gust front.

The density current head region for the cases with no upper level shear slowly increases throughout the simulation to a height of 7000 m at 5400 s (Fig. 5.6). Although this is deeper than real atmospheric density currents, this height is significantly less than those obtained by Xue (2000) for energy conserving, two-fluid steady-state density currents in which the depth can be almost 3/4ths the domain depth. In the simulations in this study, energy is lost in the interfacial layer through turbulent mixing and the depth of the cold air is specified by the depth and temperature of the cold air source, and not by

the constraints upon the flow field (Xue et al. 1997). This results in more realistic cold pool depths in terms of their relevance to organized thunderstorm outflows (Goff 1976, Wakimoto, 1982).

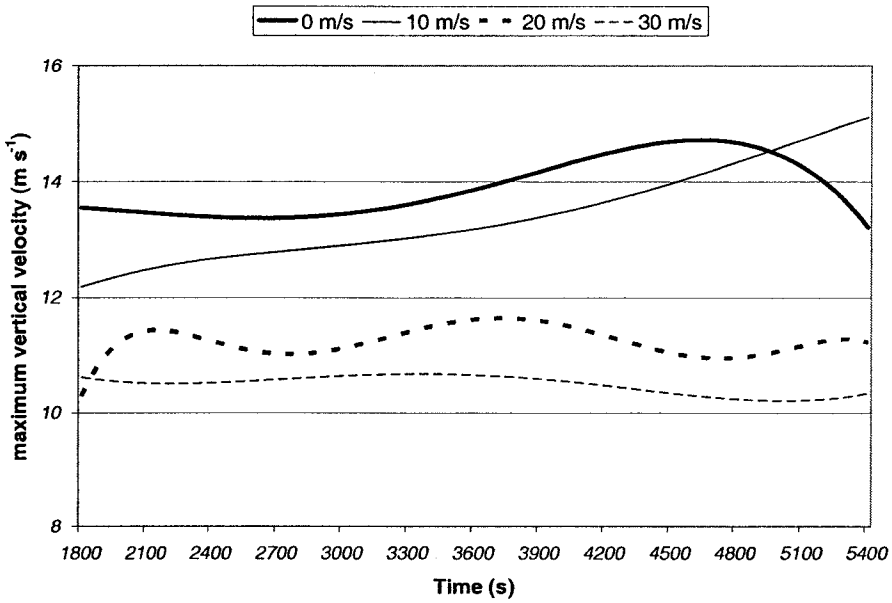


Fig. 5.7. The evolution of the maximum vertical velocity for the simulations with 0, 10, 20, and 30 m s^{-1} of shear in the 5-10 km layer.

The turbulent mixing on top of the density current plays a role in the deepening of the head region for the cases with 0-10 m s^{-1} of shear (Fig. 5.6). Upon further inspection, the shear in the lowest 5 km is found to have a significant control on the morphology of the density current head, as in many previous studies (Xu 1992, Xu and Moncrieff 1994, Chen 1995, Xue et al. 1997). In additional simulations in which the 0-5 km shear is increased to 25 and 30 m s^{-1}, the density current quickly breaks down into a complex structure. This may reflect the shallowness of the initial cold air relative to the depth of the currents required for solutions that conserve energy, vorticity, and a domain-wide pressure-momentum balance in positive low-level shear (Xue et al. 1997), but may also result from the weak to non-existent relative flow on top of the density current that allows

for the accumulation of negative horizontal vorticity along the interface, which leads to the unsteadiness of the head region (Chen 1995). This effect is related to the transition of a supercritical density current with a hydraulic jump (gust-front relative front to rear flow) (Benjamin 1968) to a subcritical current (gust-front relative rear-to-front flow) with unsteady turbulent motion along its leading edge (Xu 1992). Although the simulation with 20 m s^{-1} of shear over 0-5 km and no shear aloft is terminated at 5400 s, if the integration extended for a longer period, the head would eventually break down as in the stronger shear cases, but the head remains in a supercritical state throughout the period examined here.

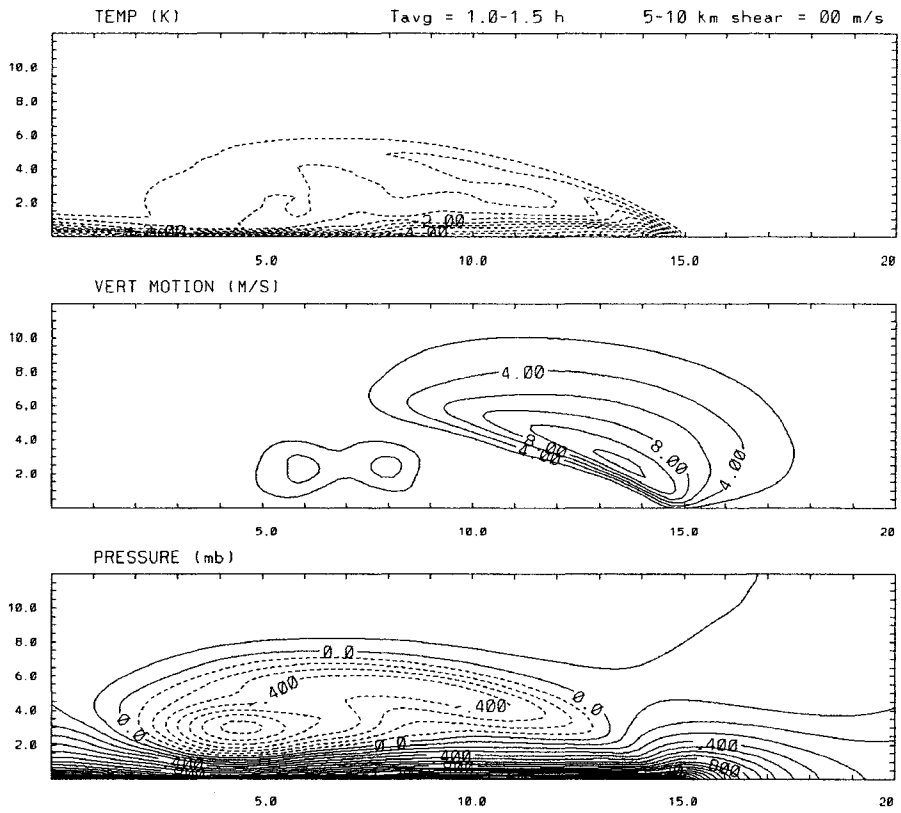


Fig. 5.8. Time-mean (1.0-1.5 h) values of perturbation potential temperature (contours every 0.5 K starting at -0.25 K), vertical motion (contours every 2 m s^{-1} starting at 2 m s^{-1}) and perturbation pressure (contours every 0.1 h Pa with negative contours dashed) for the case with no upper-level shear. Only a 20 km by 12 km portion of the domain is shown with the gust front centered at 15 km.

The structure of the simulated density currents is displayed through time-mean analyses for the period of 1.0-1.5 h for the 0, 10 and 20/5-10 km shear cases (hereafter, unless otherwise noted, these four cases are referred to by these shear values) (Figs. 5.8-5.10). The density current head for the no-shear case grows in depth and expands rearward with time in a manner that slightly reduces the slope of the density current interface through the 1.5 h simulation time. The perturbation pressure field shows well-known features of density currents, including a non-hydrostatic pressure ridge ahead of the gust front (between x=15 km and x=18 km in Fig. 5.8) resulting from the converging inflow, a broad region of near-surface high pressure resulting from the weight of the negatively buoyant air above (at all x values < 15 km below z=2 km), and lowered pressure in the region of the turbulent mixing associated with the persistent generation of negative vorticity (generally between x=3-13 km and z=2-6 km) (Droegemeier and Wilhelmson 1987).

Similar behavior is found for the case with 10 m s^{-1} of shear (Fig. 5.9), but the density current head does not become as deep (Fig. 5.6) and does not expand as far rearward with time as in the case with no upper-level shear. The slope of the density current interface is more sloped in the upper portion of the head (c.f. Figs. 5.8 and 5.9), which was found to occur for conservative, steady-state density currents in weak to moderate 3-10 km shear by Xue (2000). The expansion of the head in conjunction with a steepened slope results in an expanded region of vertical motion. The perturbation pressure field displays the same features as found for the case with no upper-level shear, but also displays a new relative high pressure above the head region related to a stagnation point in the flow (not shown), as found for fixed density current barriers by

Shapiro (1992) and for conservative, steady-state density currents by Xue (2000) for the stronger upper-level shears. This high pressure region "pushes down" the density current head (Fig. 5.6) and restricts the rearward expansion of the head region for the cases with positive upper-level shear.

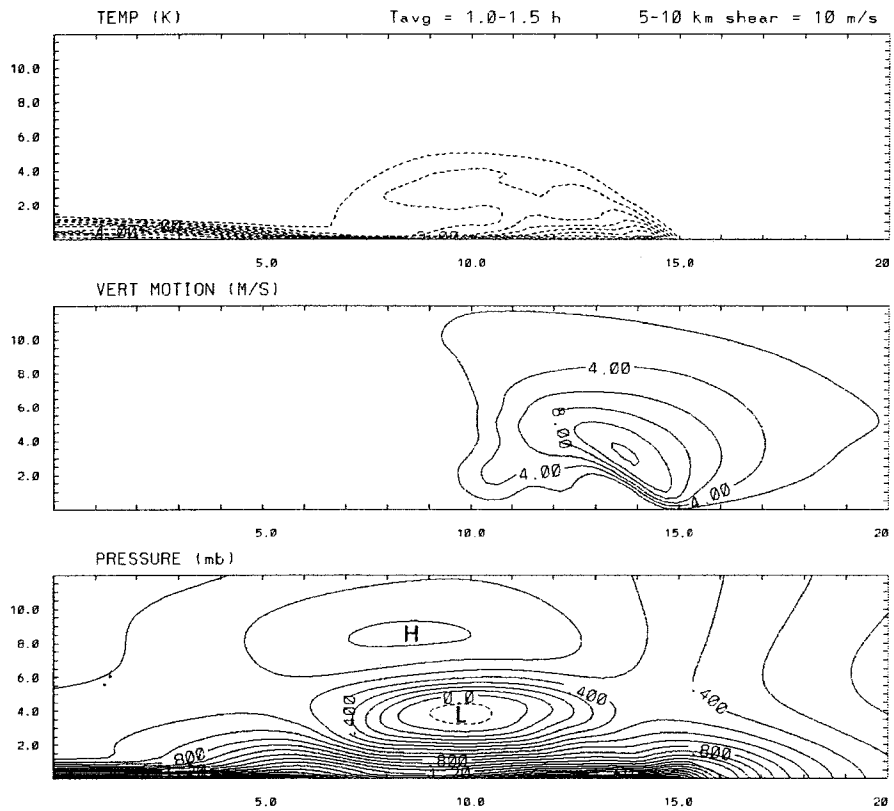


Fig. 5.9. As in Fig. 5.8, but for the case with 10 m s^{-1} of upper-level shear with regions of relative high (H) and low (L) pressure noted.

As the 5-10 km shear is increased to 20 m s^{-1}, the perturbation high pressure region in upper levels becomes more pronounced (Fig. 5.10). The result is a further lowering of the density current head region (Fig. 5.6) and an overall increased steadiness to the flow. Also notice that the slope of the upper half of the head becomes lower once again, which is due to the head height becoming suppressed below the upper-level shear layer. Although the region of vertical motion expands with time, it does not expand as

much as the head for weaker shear cases and the maximum magnitude is decreased owing to decreased convergence along the interface. The lowering of the head and the weakening of the upward motion along the interface continues as the shear is increased to 30 m s^{-1} (Figs. 5.6 and 5.7).

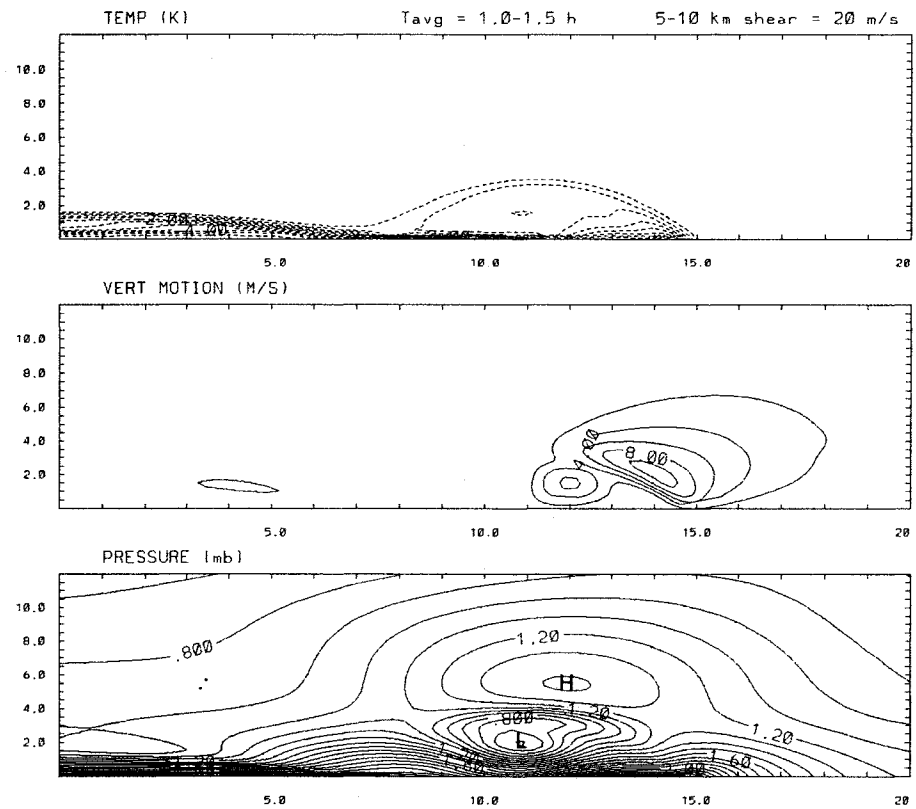


Fig. 5.10. As in Fig. 5.8, but for the case with 20 m s^{-1} of upper-level shear.

In the study by Shapiro (1992), the maximum upward motion along the interface also was found to decrease with increasing the shear throughout the troposphere. In that study, the density current morphology was fixed as a barrier, and therefore, the decrease in vertical motion was directly the result of less mass impinging on the barrier with an increase in shear. However, since the 0-5 km shear does not change in this study, the decrease in vertical motion is the result of the suppression of the density current head depth by the introduction of shear above the cold pool and the associated reduction of

mass convergence along the interface. Despite arising in different ways, this decrease in vertical motion along the interface allows a test of the hypotheses of Shapiro (1992) using these simulations.

5.4.1.1 Parcel analyses

The goal of the trajectory analyses is to examine the vertical displacement of parcels as they encounter the forced updraft along the density current interface. To account for the unsteadiness noted in the zero-to-weak upper-level shear cases, the vertical displacement of parcels is examined through a series of trajectory calculations rather than through the streamfunction for the time-averaged flow. Trajectories are made from starting positions in the undisturbed flow ahead of the gust front at each model vertical level (every 250 m) between 125 m and 1875 m. The trajectories at each starting height are calculated using model output every 30 s and are calculated every 30 s from 1800 to 2400 s, giving a total of 21 trajectories for each of the eight starting positions for each simulation.

Results show that the maximum displacement of low-level (0-2 km) parcels is larger for the 5, 10, and 15 m s^{-1} shear cases than it is for the no-shear case (Fig. 5.11). The maximum in the distribution (~9000-11000 m) occurs somewhere between 5 and 10 m s^{-1} and then decreases to displacements of only 4000 m for the 30 m s^{-1} shear case. Displacements are roughly the same for 17 m s^{-1} of upper-level shear as they are for no upper-level shear and are clearly larger for intermediate shear values. It is interesting that much of the range of the observed derecho shear profiles is contained within 5-10 km shear values of 5-20 m s^{-1} (Fig. 4.8).

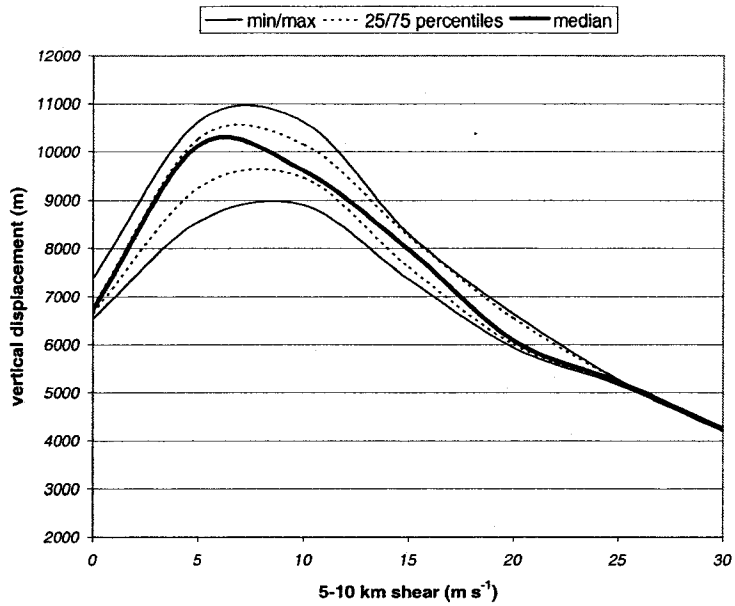


Fig. 5.11. The distribution of the maximum displacement of low-level (0-2 km) parcels (m) for various values of 5-10 km shear. Thin solid lines enclose the maximum and minimum values among the 21 trajectories, thin dashed lines enclose the 25th and 75th percentiles, and the thick solid line is the median.

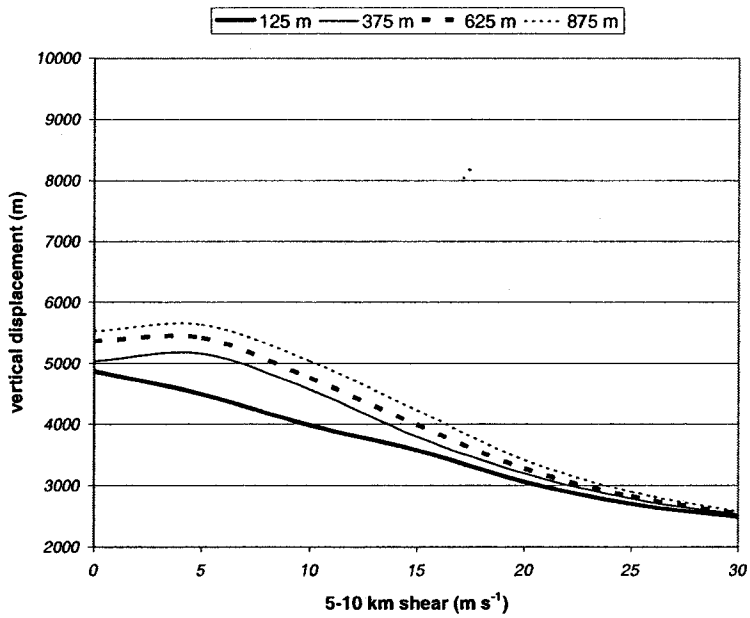


Fig. 5.12. The median of the maximum displacements of air parcels among the 21 trajectory calculations that begin in the 0-1 km layer for various values of 5-10 km shear.

Analysis of the displacements at each level reveals interesting behavior. The surface parcels (z=125 m) show maximum displacements that are largest for the no-shear

case (Fig. 5.12). For the parcels that begin at 375 m, 625 m and 875 m, the maximum displacements are virtually the same for the no-shear and 5 m s^{-1} shear cases before decreasing for the larger shears. However, the largest parcel displacements occur in the

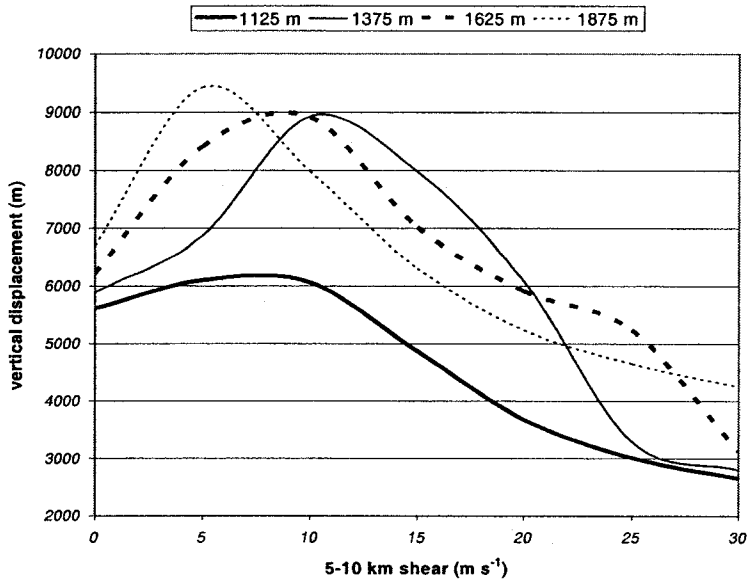


Fig. 5.13. The median of the maximum displacements of air parcels among the 21 trajectory calculations that begin in the 1-2 km layer for various values of 5-10 km shear.

1-2 km layer (the "elevated" parcels) for the profiles with weak to moderate upper-level shear (the median values show a maximum at either 5 or 10 m s^{-1}) (Fig. 5.13). It is interesting that for the parcels that begin at 1325 and 1675 m, the parcels are displaced the same amount for the 20 m s^{-1} case as for the no shear case, which clearly indicates the enhancement of the deep lifting with the addition of upper level shear for the elevated parcels.

Further insight into this behavior is gained through an illustration of the trajectory paths for the 0, 10, and 20 shear cases (Fig. 5.14). For the no shear case, the parcels rise as they encounter the upward motion and are swept rearward relative to the gust front (Fig. 5.15a) forming a jump-type updraft (Moncrieff 1992). It is interesting that, despite

the fact that the parcels are lifted to levels with no relative motion in the undisturbed environment (the midlevel wind speeds are approximately the same as the gust front motion, as shown in Fig. 5.6), the parcels continue to accelerate rearward in response to the lowered perturbation pressure in the vicinity of the head region. Although this is a dry response to the lowered pressure in the region of turbulence, a similar rearward acceleration occurs later in the 2-D and 3-D moist simulations as a response to the hydrostatic lowering of pressure within and underneath the buoyant updraft plumes (Lafore and Moncrieff 1989).

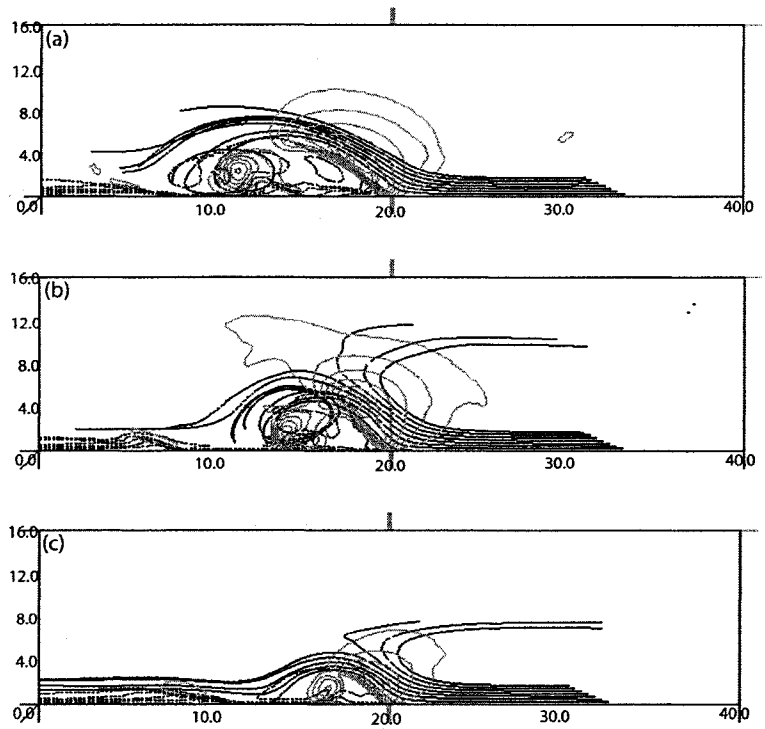


Fig. 5.14. Illustration of parcel paths in the lowest 2 km starting at 2100 s (thick solid lines) for the (a) 0 m s^{-1}, (b) 10 m s^{-1} and (c) 20 m s^{-1} shear cases. The parcel paths end at 4200 s in (a), 4500 s in (b) and at 5400 s in (c). The perturbation potential temperature (dashed lines, contoured as in Fig. 5.8) and vertical motion (thick grey lines, contoured as in Fig. 5.8) also is shown at these times.

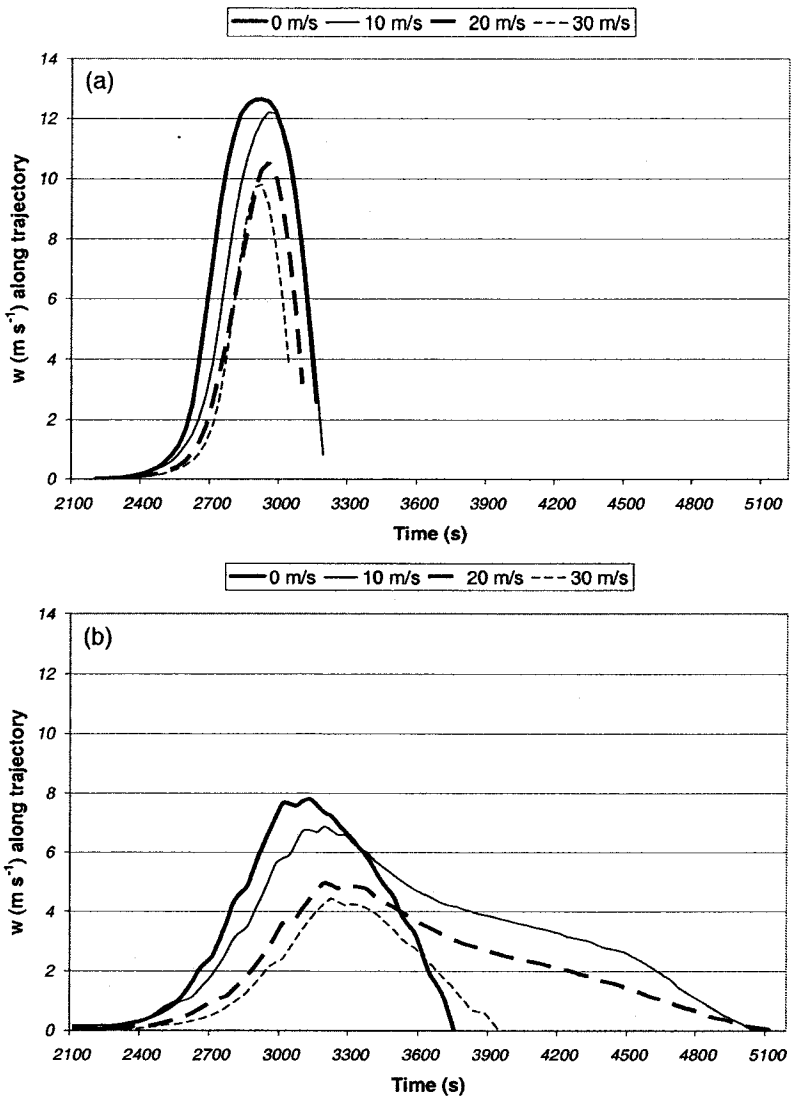


Fig. 5.15. Vertical motion (m s^{-1}) along the parcel paths for parcels starting at (a) 375 m and (b) 1625 m among the 0, 10, 20 and 30 m s^{-1} shear cases. The values are only calculated up until the point the parcel leaves the region of forced upward motion.

For the 10 m s^{-1} shear case, the low level parcels are forced over the density current as before in a jump-type updraft, to slightly lower levels than for the no-shear case. However, the parcels that begin at 1375 m, 1625 m and 1875 m overturn after they are forced upward (Fig. 5.14). The overturning results in the much larger vertical parcel displacements than for the no shear case. The flow then represents a mixed jump and overturning updraft that exists in the idealized frameworks of squall lines as summarized

by Moncrieff (1992). The overturning exists because of the existence of a critical layer in mid levels (5-7 km) for the cold pool speed and shear profiles examined in this study.

As hypothesized by Shapiro (1992), the behavior of the overturning can be explained through the time integration of the vertical velocity along the parcel paths. The low level parcels experience the strongest upward velocity (Fig. 5.15a), but the elevated parcels rise for longer periods (Fig. 5.15b). Focusing solely on the parcels that begin at 1625 m (Fig. 5.15b), even though the maximum upward velocity experienced by the parcel in the 10 m s^{-1} case is less than that experienced by the parcel in the no shear case, the parcel is eventually lifted to higher levels (c.f. Figs. 5.12 and 5.13). Therefore, the upper-level shear layer and its interaction with the forced updraft allows the elevated parcels to remain in the region of upward motion for much longer periods than both the elevated parcels for the no shear case, and for the low-level parcels for all of the shear cases (Fig. 5.15b). This shows that the hypothesis developed by Shapiro (1992) for fixed density current barriers appears to be a general result for these simulations of stratified density currents that are allowed to respond to the vertical shear in the flow.

Also notice that the elevated parcels are lifted by the overturning so that they remain close to the leading edge of the gust front, whereas, as noted before, the low-level parcels for the 10 m s^{-1} case and all the parcels for the no shear case are swept rearward (Fig. 5.14). This has important implications for the structure and maintenance of convective systems as suggested by Garner and Thorpe (1992) and later in this study.

The physical response of the parcels can be interpreted through the perturbation pressure field at the stagnation point caused by the upper-level shear. The high pressure above the cold pool accelerates the elevated parcels in the direction of the gust front

motion whereas the parcels in the no shear case continue to be swept rearward relative to the cold pool. This can be seen by examining the pressure field in the cross sections (Figs. 5.9 and 5.10) and through the calculations of the pressure gradient term along the elevated trajectories (not shown). Although this region of high perturbation pressure is produced by the upper-level shear, the high pressure also affects the reduction in parcel displacements as the upper-level shear is increased, which is not noted in Shapiro (1992) and Moncrieff and Liu (1999). This is the reason for the reduction in the displacements beyond ~10 m s^{-1} in Fig. 5.11. While the elevated parcels continue to overturn as the shear is increased to 20 and 30 m s^{-1}, the stronger perturbation pressure pushes down the cold pool which reduces the depth of convergence along the gust front. This limits the overturning to an increasingly shallower layer (Fig. 5.14c) so that only the parcel that starts at 1875 m overturns in the 30 m s^{-1} shear case. Therefore, the region of high perturbation pressure eventually counteracts the deep overturning of the elevated parcels by reducing the vertical scale of the overturning.

The results from Shapiro (1992) were for fixed density-current barriers and were designed for shear profiles that increase the shear throughout the depth of the troposphere (see Fig. 2.5). Therefore, the relative importance of the low-level versus the upper-level shear could not be gauged in that study. Additionally, the conceptual model of RKW revisted by WR, by their definition, can not be directly applied to these results since the shear is held constant below 5 km in all of the simulations. At least for the low-level shear profile and the cold pools examined in this study, the important result from this portion of the study is that *shear added entirely above the cold pool (as long as it is not*

too strong) can accomplish the increase in lifting within deep tropospheric shear. The following sections examine this result in more complex frameworks.

5.4.2 2-D moist simulations

The previous section provides an explanation for how shear elevated above the cold pool can enhance the lifting of low-level (1-2 km) parcels in an environment with modest shear in low levels. While the model design allowed for the simulation of density currents with strengths and depths similar to what is observed in the atmosphere, the dynamics are constrained by neutral stability, dry dynamics and two dimensions. This subsection qualitatively examines the consistency of the results from section 5.2.1 to 2-D simulations that include a stratified environment and moist microphysics.

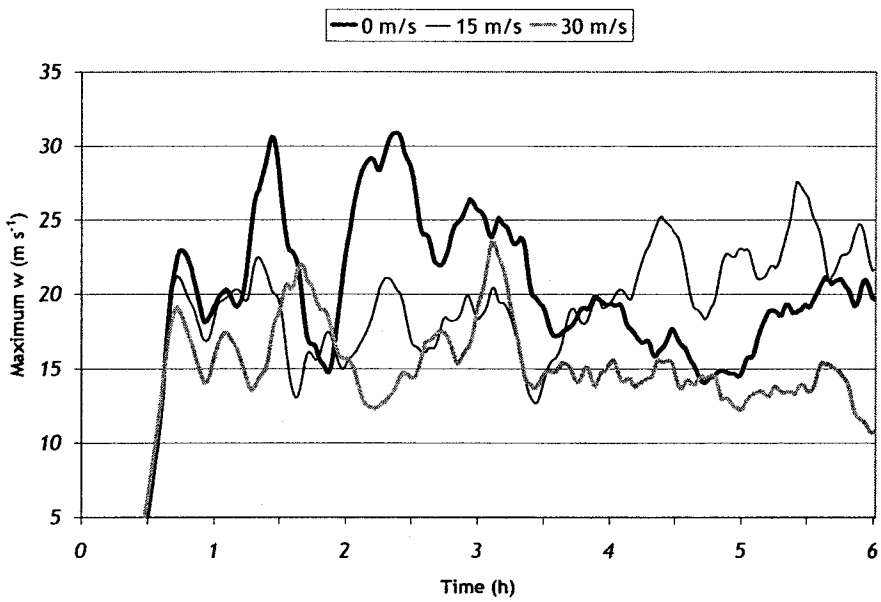


Fig. 5.16. The evolution of the maximum vertical velocity for the 0, 15, and 30 m s^{-1} 2-D moist simulations.

The behavior of the simulations will first be presented with measures of system strength between the 0, 15, and 30 m s^{-1} shear cases. Guided by these results, time averaged fields in cross sections will be presented that explore the evolution of the

convective systems. In all of the simulations, the cold pool introduced by the cooling function develops convection about 20 minutes into the simulation. The initial convective cells deposit their rain and develop a cold pool that acts to initiate further convection, which allows the cooling function to be removed after this time.

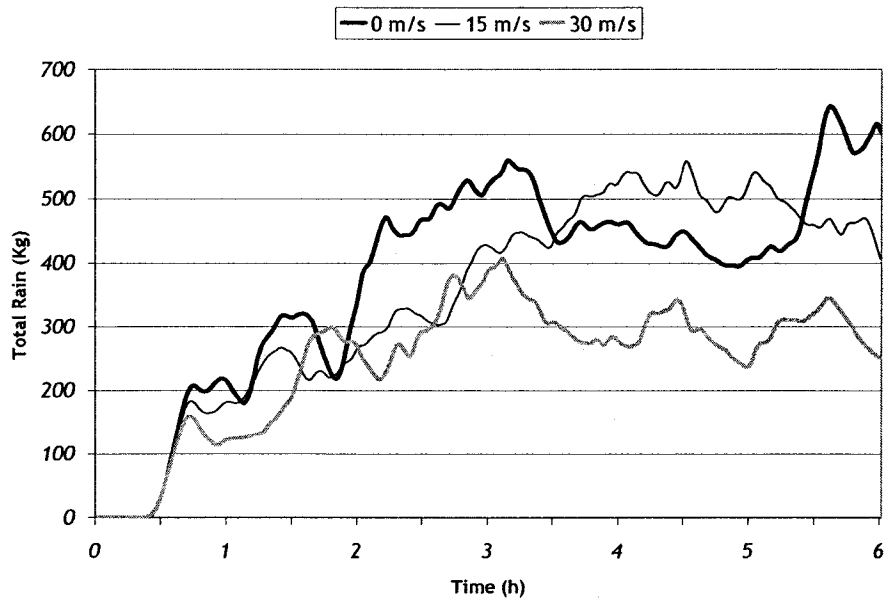


Fig. 5.17. The evolution of the domain-integrated rainwater for the 0, 15, and 30 m s^{-1} 2-D moist simulations.

The evolution of the maximum surface wind is similar for all three simulations (not shown). However, interesting differences are found when examining the evolution of the maximum updraft strength (Fig. 5.16). From 1 – 3 h, the case with no shear aloft produces the strongest updrafts. The updrafts generally become weaker in this time period as the shear is increased from 15 to 30 m s^{-1}. Additionally, the amplitude of the updraft oscillations appears to be largest for the case with no shear aloft. This behavior was noted in RKW for the simulated squall lines that appeared to be close to the optimal condition and represents the retriggering of cells along the gust front. After about 3 h, a transition occurs where the maximum updrafts for the case with no shear aloft lose their

amplitude. In contrast, the maximum updrafts for the 15 m s^{-1} shear case retain the amplitude oscillations from the first few hours of the simulation and become stronger than the updrafts for the no shear case. This difference is most apparent in the period between 4 and 5.5 h and also is apparent for the evolution in the strongest downdrafts. The updrafts for the 30 m s^{-1} simulation, however, remain the weakest of the three cases in all time periods and also appear to lose amplitude with time.

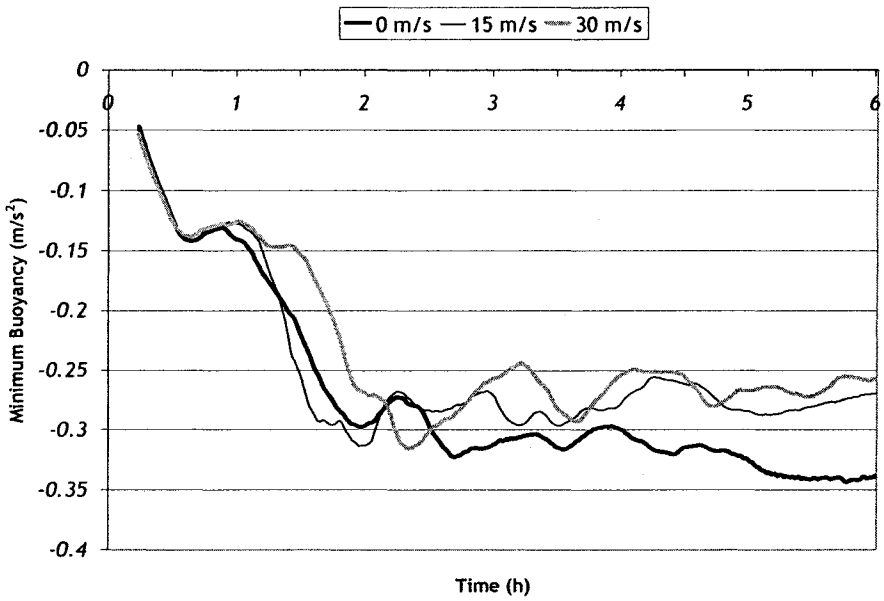


Fig. 5.18. The evolution of the minimum buoyancy acceleration (m s^{-2}) for the 0, 15, and 30 m s^{-1} 2-D moist simulations.

The domain-integrated rainfall shows behavior similar to that for the updrafts and downdrafts, with the no shear case producing the most rainfall in the early periods, and the 15 m s^{-1} shear case producing the most rainfall in the later periods (Fig. 5.17). The 30 m s^{-1} case consistently produces the least amount of rainfall among the three cases. However, it is interesting that the no shear case produces the largest values of negative buoyancy from 2.5 h to the end of the simulation (Fig. 5.18), but this does not necessarily translate into a faster cold pool motion (Fig. 5.19). The no shear case appears to show the

most increase in gust front speed from 1.5 to 5 h, but the 15 and 30 m s^{-1} cases also show a general trend to produce a slightly faster cold pool with time. In the period when the 15 m s^{-1} case is producing the strongest updrafts, the strongest downdrafts and the most rainfall (after ~ 3.5 h), the 15 m s^{-1} case shows the fastest cold pool motion, but the differences are relatively small.

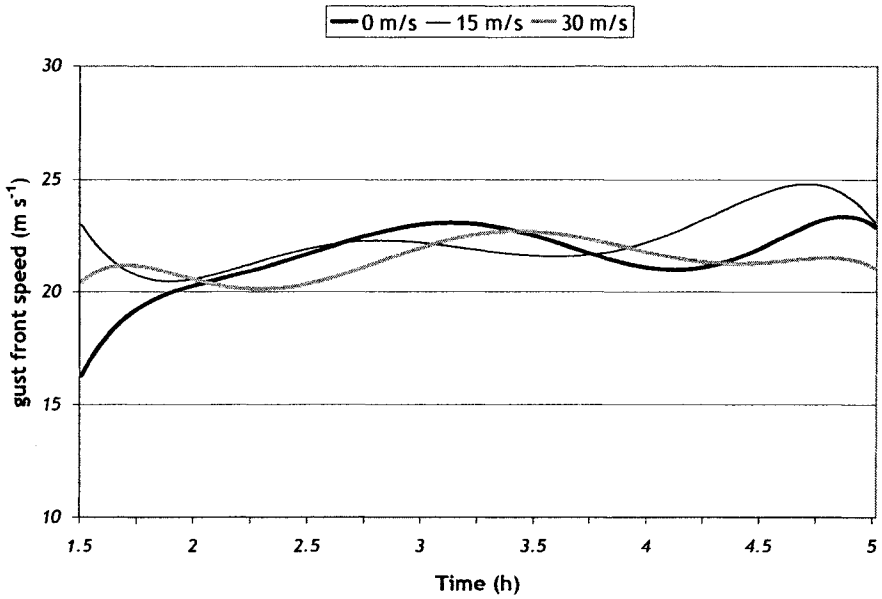


Fig. 5.19. The evolution of the domain-integrated rainwater for the 0, 15, and 30 m s^{-1} 2-D moist simulations.

To understand the significance of these differences between the three simulations, fields of buoyancy, upward vertical motion and rainwater mixing ratio are time-averaged with the gust front positioned at the center of the domain for two periods. The time-averaged fields are first presented for the period from 2-3 h; the period when the no shear case appeared to be the strongest case, and then for the period from 4 -5 h; the period when the 15 m s^{-1} shear case appeared to be the strongest case. As in many past 2-D simulations of convection, cells periodically generate and decay in the vicinity of the cold pool leading edge and are swept rearward in low-levels relative to the gust front leading

edge. Although these cells can alter characteristics of the forced updraft and low-level inflow through buoyancy induced circulations and pressure perturbations (Fovell and Tan 1998), the time averaged fields are useful for displaying the general circulation features contained in the system-scale structure that support the transient development of the convection (Xue et al. 1997).

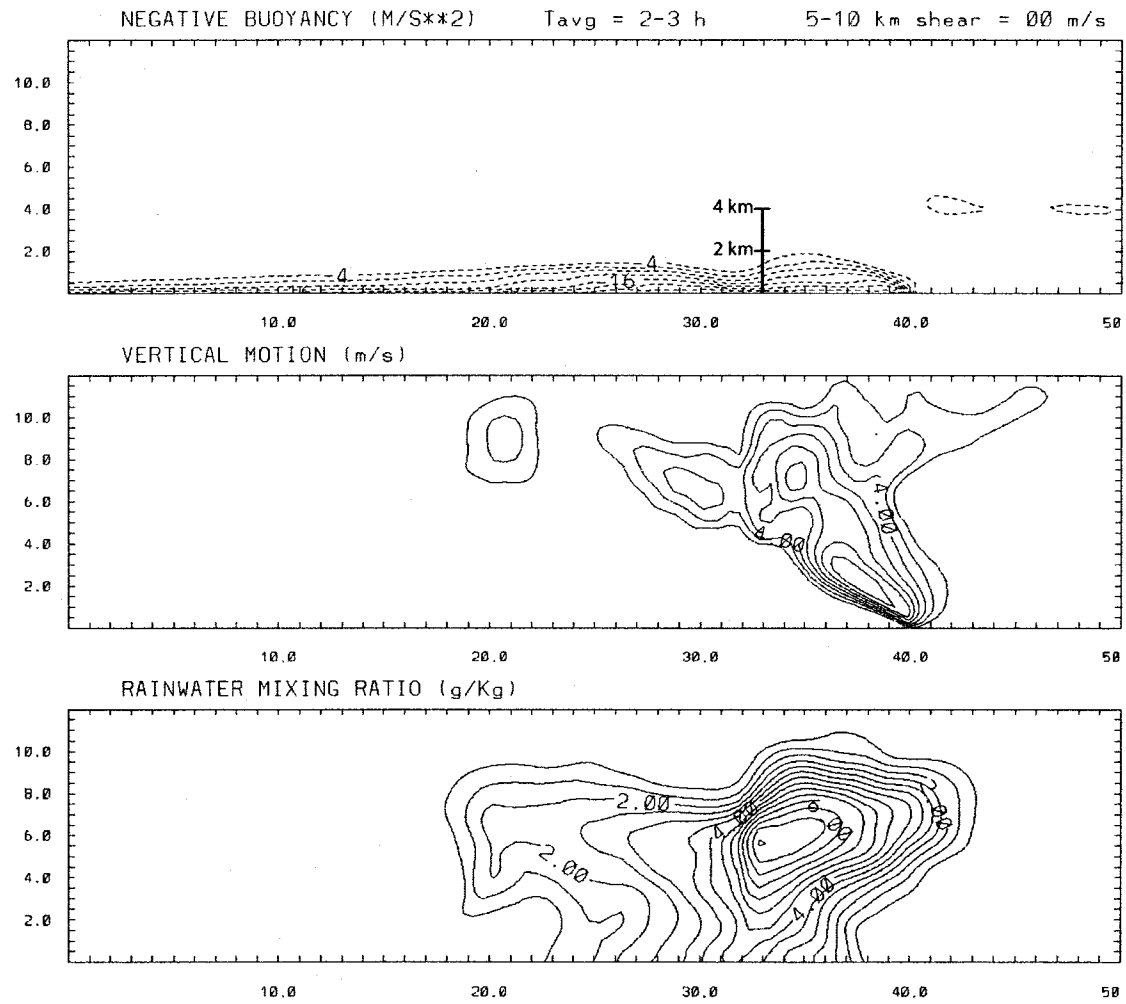


Fig. 5.20. Time-mean (2-3 h) values of negative buoyancy (contours every 0.03 m s^{-2} starting at -0.02 m s^{-2}), upward vertical motion (contours every 1 m s^{-1} starting at 2 m s^{-1}) and rainwater mixing ratio (contours every 0.5 g kg^{-1} starting at 1 g kg^{-1}) for the case with no shear in the 5-10 km layer. Only a 50 km by 12 km portion of the domain is shown with the gust front centered at 40 km.

For the no shear case, the cells are actively generated within a few km of the gust-front leading edge during the 2-3 h period (Fig. 5.20). The cells become loaded with

precipitation, weaken and deposit their rain generally within 10 km behind the gust front. The leading edge of the cold pool is deepest in this region and has a mean depth of about 2 km. The forced updraft is sloped along the cold pool with a magnitude of about 8 m s^{-1}. The time-averaged region of upward motion of 3-6 m s^{-1} in mid levels reflects the collection of the convective updrafts in this region.

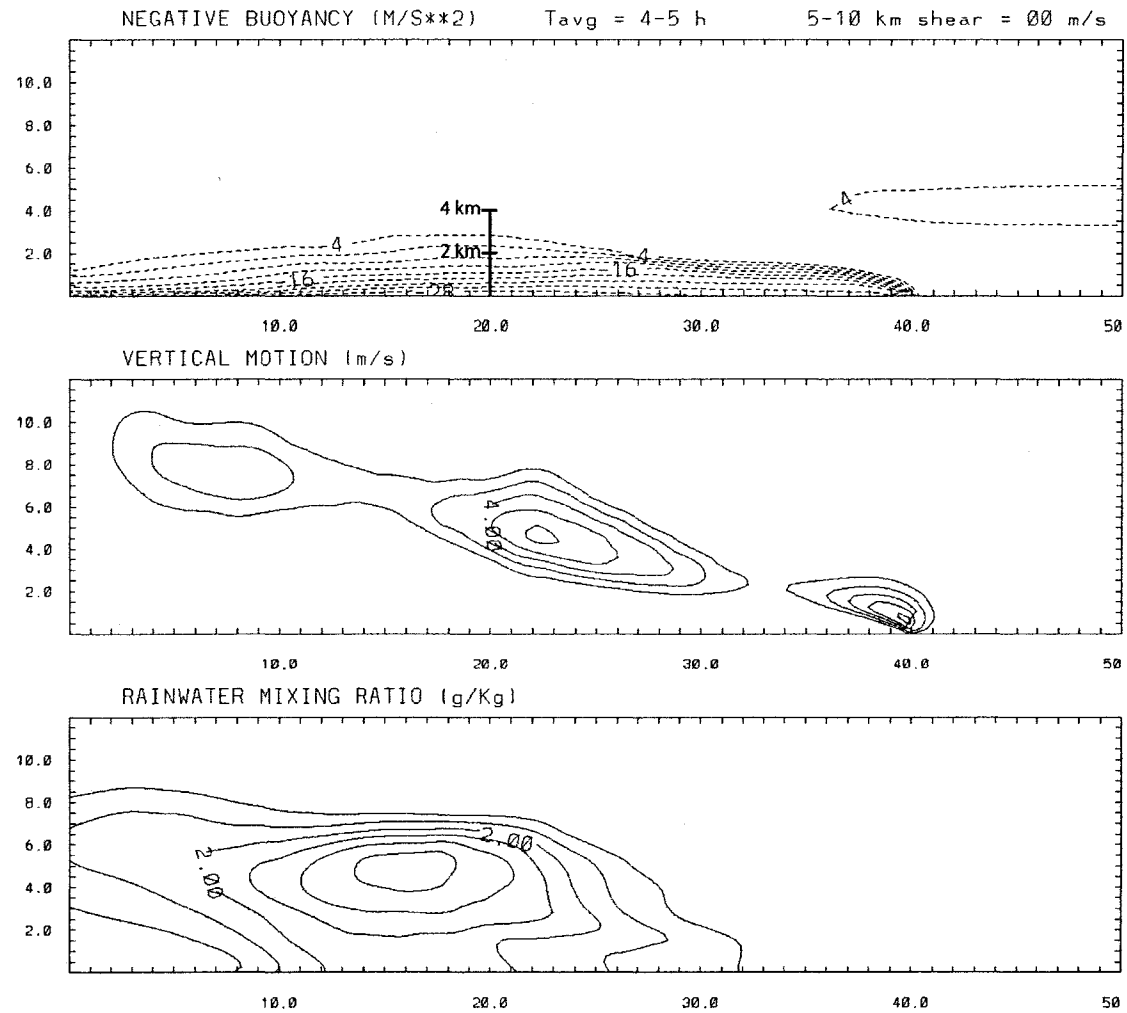


Fig. 5.21. As in Fig. 5.20 but averaged for the period of 4-5 h.

For the latter period (4-5 h), convective cells continue to be generated, but do not occur with as much frequency and are swept further rearward relative to the gust front (Fig. 5.21). There is now a clear separation between the forced updraft (near 40 km in

Fig. 5.21) and the time-averaged collection of the convective updrafts, which are now found 10-30 km behind the gust front leading edge. In response to this rearward shift in

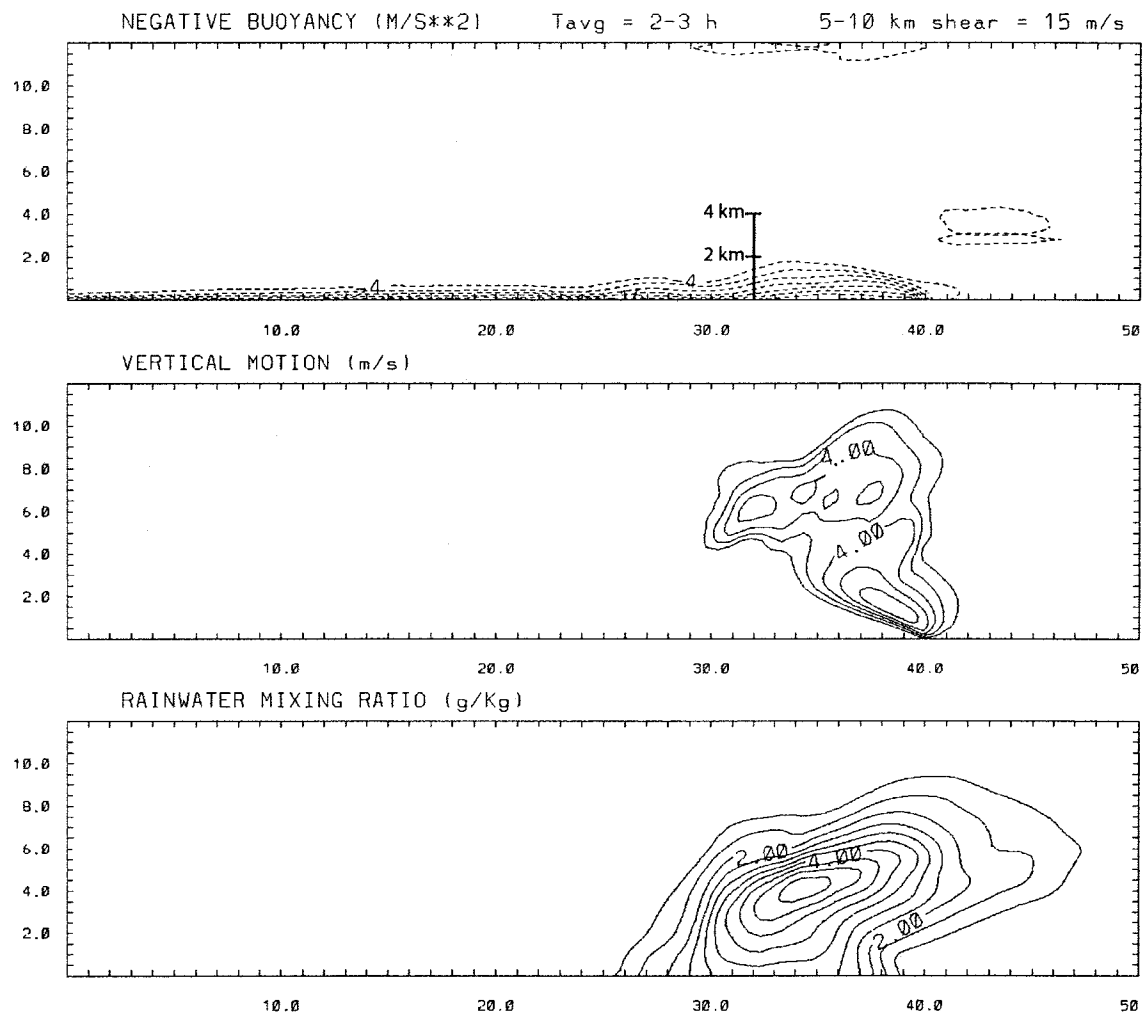


Fig. 5.22. As in Fig. 5.20 but for the case with 15 m s^{-1} of 5-10 km shear.

convective cells and rainfall, the cold pool is deepest about 20 km behind the gust front and is over 2.5 km deep in the time-averaged fields. This region is responsible for the largest values of negative buoyancy among all three of the simulations (Fig. 5.18). The cold pool depth closest to the surface gust front position shows a decrease to about 1 km, which is responsible for the weakened forced updraft magnitude. This behavior in the latter period resembles the decaying phase of the squall lines as discussed in RKW, in

which the gust front surges ahead of the updrafts and the convection continues to weaken with time. However, as in Fovell and Ogura (1989) and in the updated simulations of WR that use larger domains, the state of the convective system shown in Fig. 5.21 represents an equilibrium state in which the thermodynamics adjust to the wind profile. Although in a weakened state, convection continues to develop throughout the 6 h simulation time.

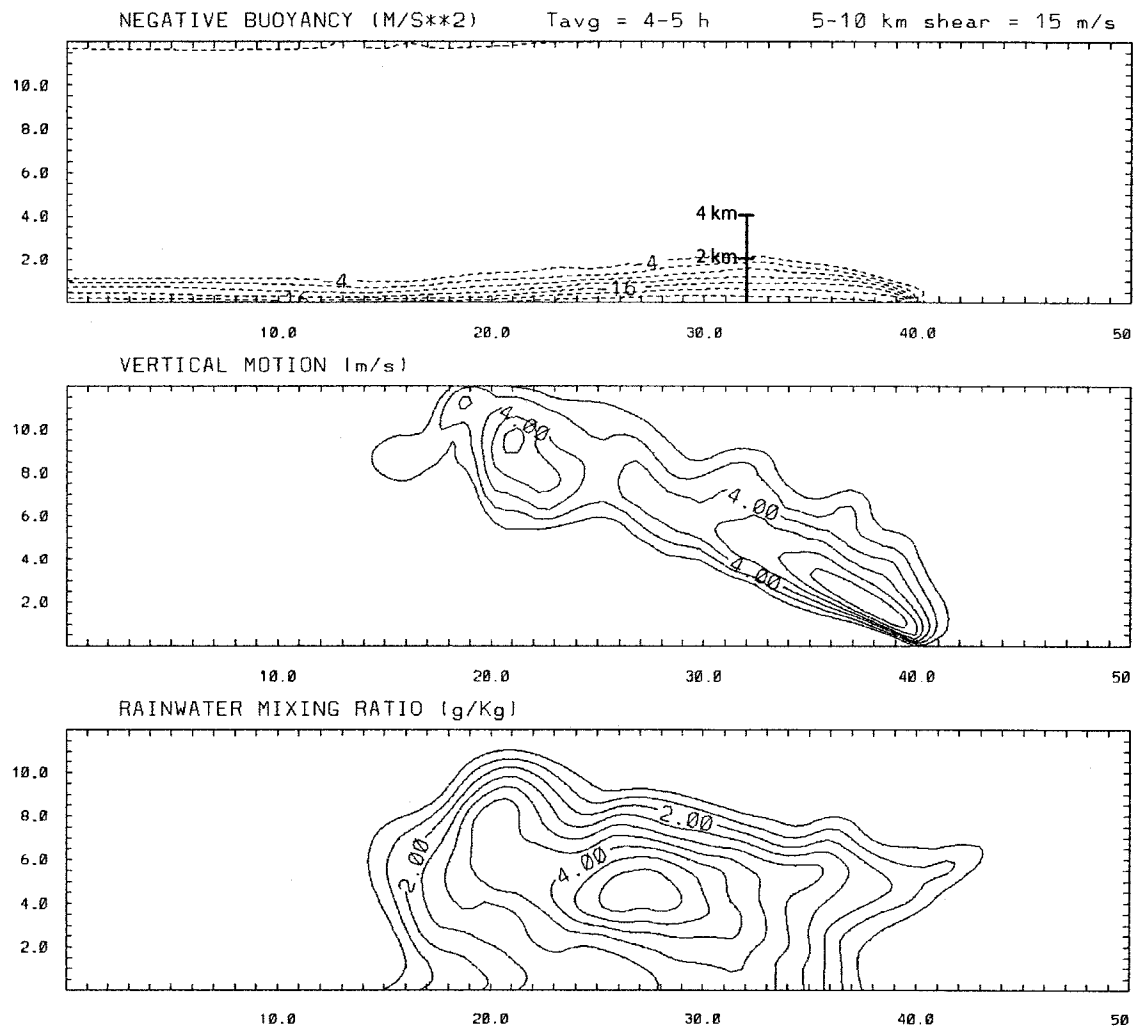


Fig. 5.23. As in Fig. 5.20 but for the case with 15 m s^{-1} of 5-10 km shear averaged in the 4-5 h period.

For the 15 m s^{-1} case, the cells actively develop within a few km of the gust front during the 2-3 h period (Fig. 5.22), as for the no shear case. The maximum cold pool

depth near the leading edge is slightly smaller for the 15 m s^{-1} case (~1.8 km) as compared to the no shear case (~2.1 km) and is located a few more kilometers behind the gust front. These subtle differences in the time averaged fields are more noticeable when viewing the model output at 2 min intervals (not shown). The result in the time-averaged fields is a weaker forced updraft (~ 6 m s^{-1}) and weaker convective cells (Fig. 5.22) as compared to the no shear case, although the convective cells generate and decay within 10 km of the gust front leading edge. The most apparent differences in the time-averaged fields between the no shear and 15 m s^{-1} cases are found for the latter period (Fig. 5.23). In the 15 m s^{-1} case, the core of the convective cells remains positioned about 10 km behind the gust front (Fig. 5.23), as opposed to expanding rearward with time for the no shear case (Fig. 5.21). This results in the deepening of the cold pool within 10 km of the gust front to over 2 km in depth and the subsequent strengthening of the forced updraft, which now has a maximum strength between 7 and 8 m s^{-1}. In the 15 m s^{-1} case, there is no longer a clear separation between the forced updraft and the convective updrafts and the overall slope of the system is more upright (Fig. 5.23). This same evolution is noted for the 30 m s^{-1} case, but the forced and convective updrafts, as well as the cores of convective rainfall, are clearly weaker in the time-averaged fields in response to the significantly shallower cold pool, especially in the earlier period (not shown).

The above analysis shows that the arguments and physical responses garnered from the dry, neutral stability simulations agree qualitatively with the response noted in the moist simulations within a thermally stratified environment. The system that develops in no upper-level shear is initially stronger than the system that develops in moderate upper-level shear due to the deeper convergence and stronger forced lifting

along the cold pool. However, without the overturning of the elevated parcels in the no shear case, the cells continue to be swept rearward by the front-to-rear flow in all levels (the gust front moves at 20-23 m s^{-1} seen in Fig. 5.19).

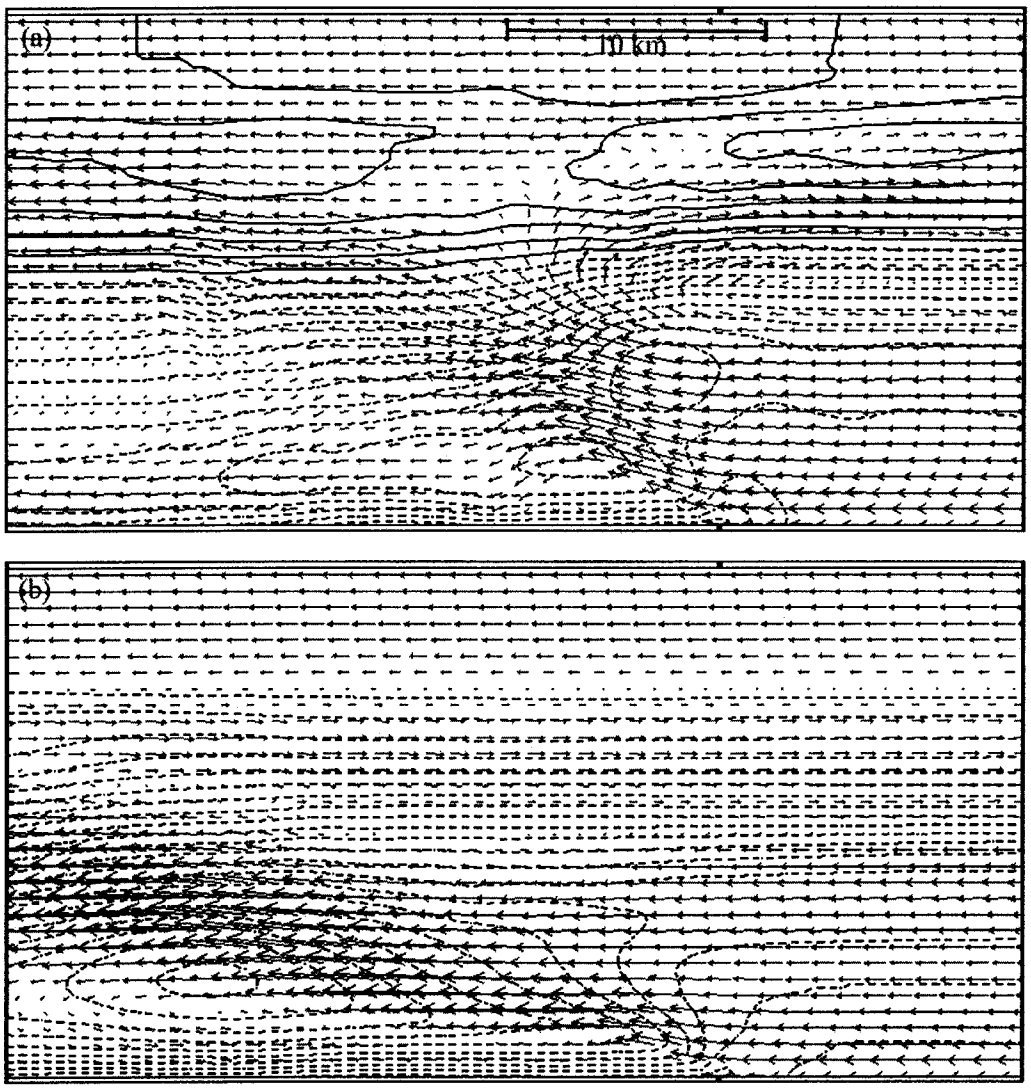


Fig. 5.24. Perturbation pressure (contours every 0.4 h Pa with negative values dashed) and gust-front relative winds in a 40 km cross section through the gust front averaged from (a) 2-3 h and (b) 4-5 h for the case with no shear aloft.

Cross sections of pressure perturbation and gust front-relative winds show evidence of this behavior (Fig. 5.24-5.26). The overturning noted in the earlier period in the no shear case (Fig. 5.24a) does not affect the tilt of the subsequent updrafts in the

later time period (Fig. 5.24b). The lowered pressure created by the buoyant updrafts accelerates the flow and the updrafts plumes rearward with time. Without the background overturning, the result is a cold pool that progressively deepens further

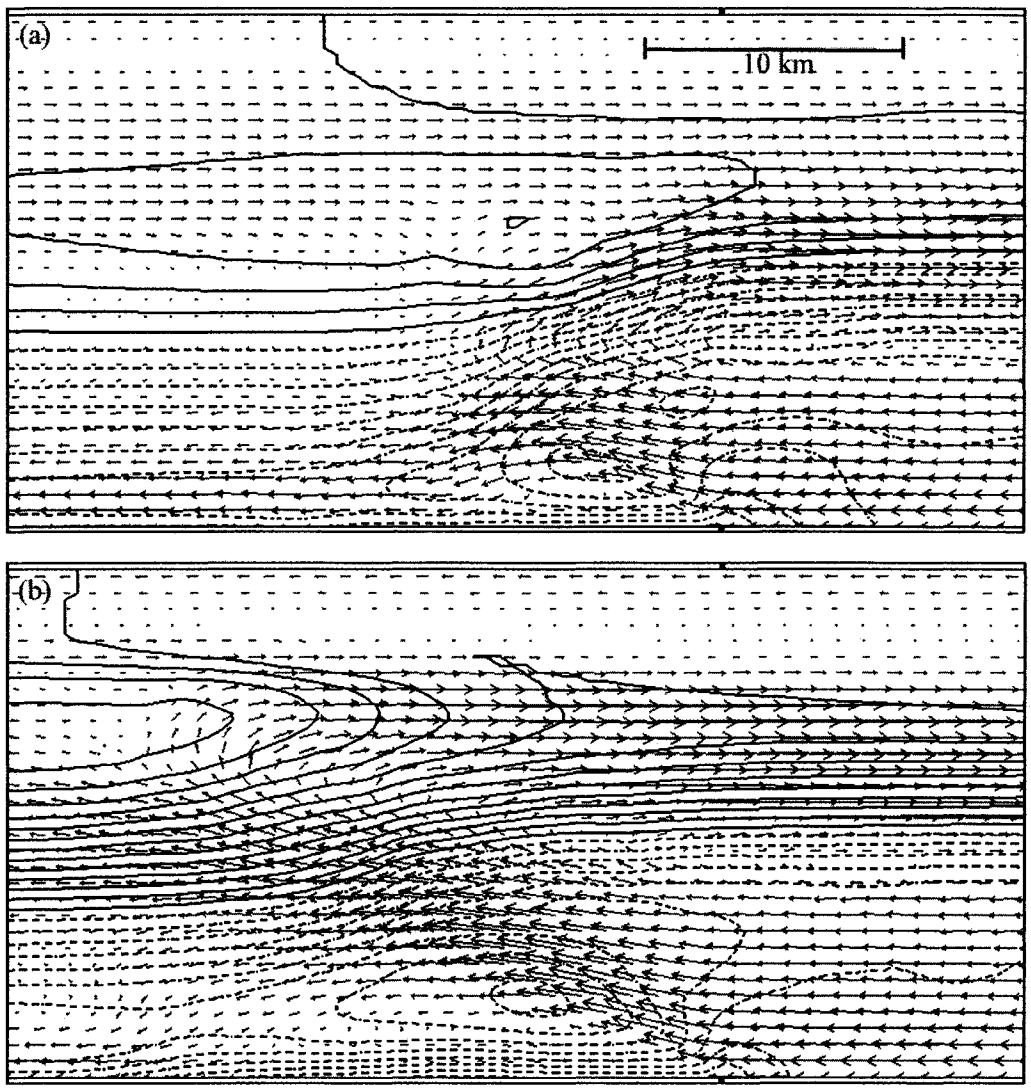


Fig. 5.25. As in Fig. 5.24 but for the case with 15 m s^{-1} of 5-10 km shear.

behind the gust front and become shallower closer to the cold pool leading edge as noted before. This feeds back into a weaker forced updraft and a succession of weakened convective updrafts that have a significant rearward slope (Fig. 5.24b). Eventually, the

system reaches an equilibrium state, as described before, with a substantial upshear tilt and weakened updrafts.

For the 15 m s^{-1} case, the upper-level shear interacts with the cold pool (and the vertical motion fields of the convective cells in the moist case) to create the perturbation high pressure noted in the 2-D dry simulations that offsets the rearward acceleration of the low-midlevel parcels and maintains the overturning of the elevated parcels (Fig. 5.25). The system maintains itself by keeping the convective cells within 10 km of the gust front, which maintains (and deepens) the cold pool in this region and promotes the continuation of the deep lifting and the overturning. Overturning still occurs in the 30 m s^{-1} case, but the vertical scale is contracted by the increased pressure perturbations and the shallower cold pool (not shown). This results in a shallower and weaker system as a whole. Overall, this shows qualitative consistency with the behavior of the 2-D dry simulations and supports the claims of Shapiro (1992), Moncrieff and Liu (1999), Xue (2000), Coniglio and Stensrud (2001) that the shear throughout the depth of the troposphere has potentially important effects on the maintenance of convection that is forced by the deep convergence along a cold pool.

5.4.3 3-D simulations

There are many important restrictions that are removed by adding a third dimension, which can alter the behavior of the simulations with the addition of upper-level shear. As previously noted, model environments with strong low-level wind shear tend to allow the development of bow echo circulations and strong asymmetries to the flow (W93). The third dimension is especially important within environments of significant deep-tropospheric shear that facilitate the development of supercells and the

associated dynamic pressure perturbations that add complexity to an assessment of the physical mechanisms at work and the perceived strength of the system (RKW, Coniglio and Stensrud 2001, WR). Therefore, it is especially important to examine the effects of the upper-level shear on simulations of linear MCSs that develop within a 3-D environment. This study uses these more complex simulations to focus on the qualitative consistency of the arguments developed in a 2-D dry, neutral environment. Adding to the complexity is the addition of ice microphysics, which can substantially alter the strength of the cold outflows and the distribution of convective cells in 3-D simulations of deep, moist convection (Gilmore et al. 2004). However, the goal is to provide an increase in realism within the class of MCS simulations that are produced within horizontally homogeneous environments and not to document the effects of the increased complexity.

5.4.3.1 System maintenance

As in the 2-D moist simulations, the behavior of the simulations is first presented with measures of system size and strength. The initial convective cells that are initiated by the warm bubbles deposit their rain and develop a cold pool that acts to initiate further convection. By approximately 2 h, the cold outflows from the individual cells expand and collect to form a cold pool on the scales of MCSs (Zipser 1982). The following material focuses on the behavior of the simulations after the development of the MCS and the primary role of the upper-level shear.

As in the 2-D moist simulations, the evolution of the maximum surface wind is similar for all three simulations (Fig. 5.26). The strongest surge and longest duration of surface winds (noted by the amplitude fluctuations in Fig. 5.26) occurs for the case with no shear aloft between 3 and 4 h, during which the peak surface winds reach 43.5 m s^{-1}

near 3.7 h. The peak surface wind for the 15 m s^{-1} case reaches about 41 m s^{-1} about a half hour later and has a narrower distribution within the period of the wind surge. A similar surge in the maximum surface winds occurs between 4.5 and 5 h for the 15 m s^{-1} case. In this later time period, the maximum surface wind speed for the no shear and 15 m s^{-1} shear cases is similar. The amplitude fluctuations for the 30 m s^{-1} case are smaller and mostly weaker than the other two cases.

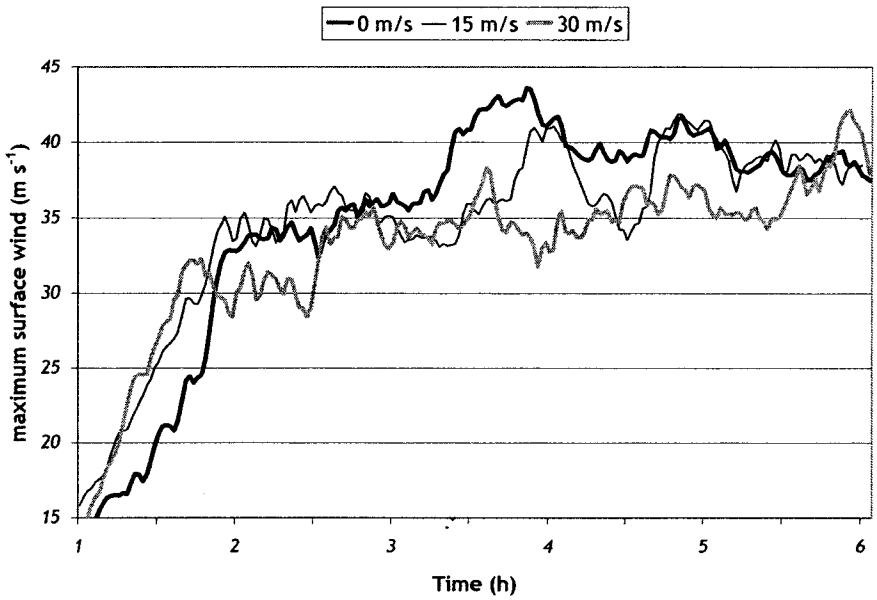


Fig. 5.26. Evolution of the maximum surface (125 m) wind for the 3-D simulations.

More pronounced differences are found when examining the evolution of the maximum updraft (Fig. 5.27) and downdraft strengths (5.28). The simulation with no shear aloft contains stronger cells initially (before 1.25 h), owing to the shearing of the updrafts in upper-levels for the cases with positive upper-level shear. As the larger scale cold pool develops after 1.5 h, new updrafts develop along the leading edge, all with similar peak magnitudes. However, closer examination of the new updrafts that are initiated along the cold outflows from the initial cells shows that the updrafts for the 15 m s^{-1} and 30 m s^{-1} shear cases are collectively stronger in the period from 1.5 h – 2 h. This

is evident somewhat in the evolution of the peak downdraft magnitudes (Fig. 5.28) and the minimum values of buoyancy (Fig. 5.29).

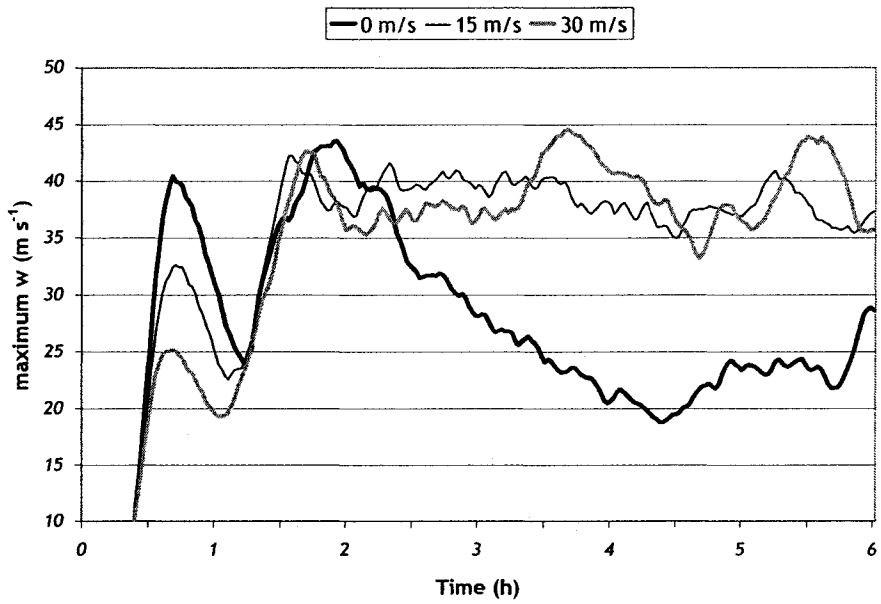


Fig. 5.27. Evolution of the maximum vertical velocity for the 3-D simulations.

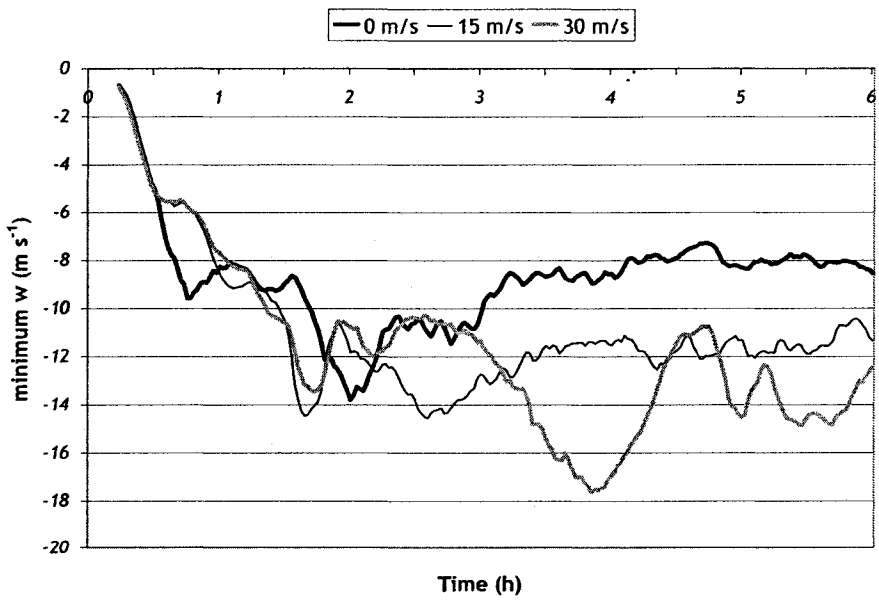


Fig. 5.28. Evolution of the minimum vertical velocity for the 3-D simulations.

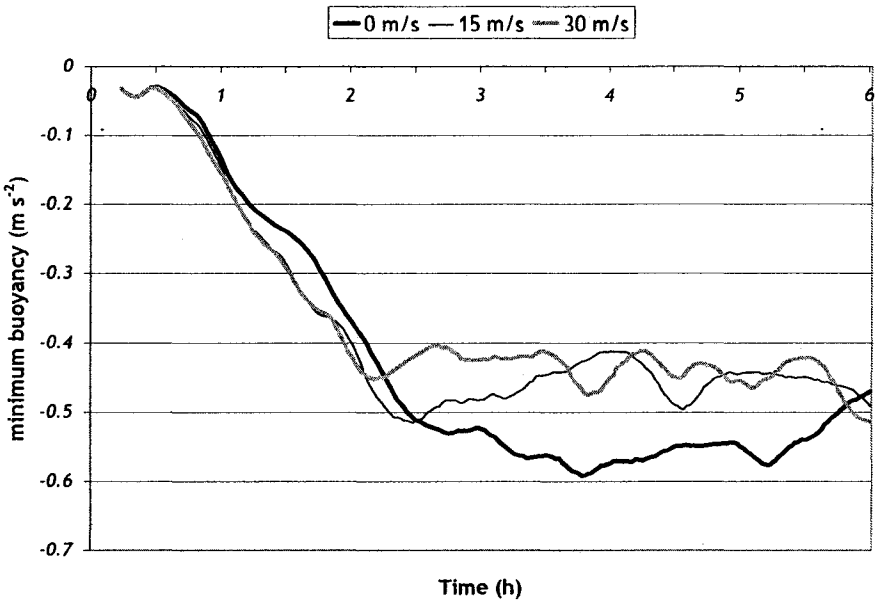


Fig. 5.29. Evolution of the minimum buoyancy acceleration for the 3-D simulations.

A clear separation in the maximum updraft/downdraft magnitudes occurs after 2 h, which coincides with the transition of the line of isolated convective cells into an organized MCS structure (displayed in Fig. 5.30). As in the 2-D moist simulations, the evolution of the maximum updrafts reveal that the case with no upper-level shear enters an upshear-tilting phase once the cold pool becomes firmly established. During this phase, the convective cells and the precipitation becomes located farther behind the surface gust front until about 4.5 h, when the maximum updrafts maintain a constant strength of 22-24 m s^{-1}. As in the 2-D simulations, the case with no shear aloft produces the largest magnitudes of negative buoyancy as the updrafts expand rearward (Fig. 5.29).

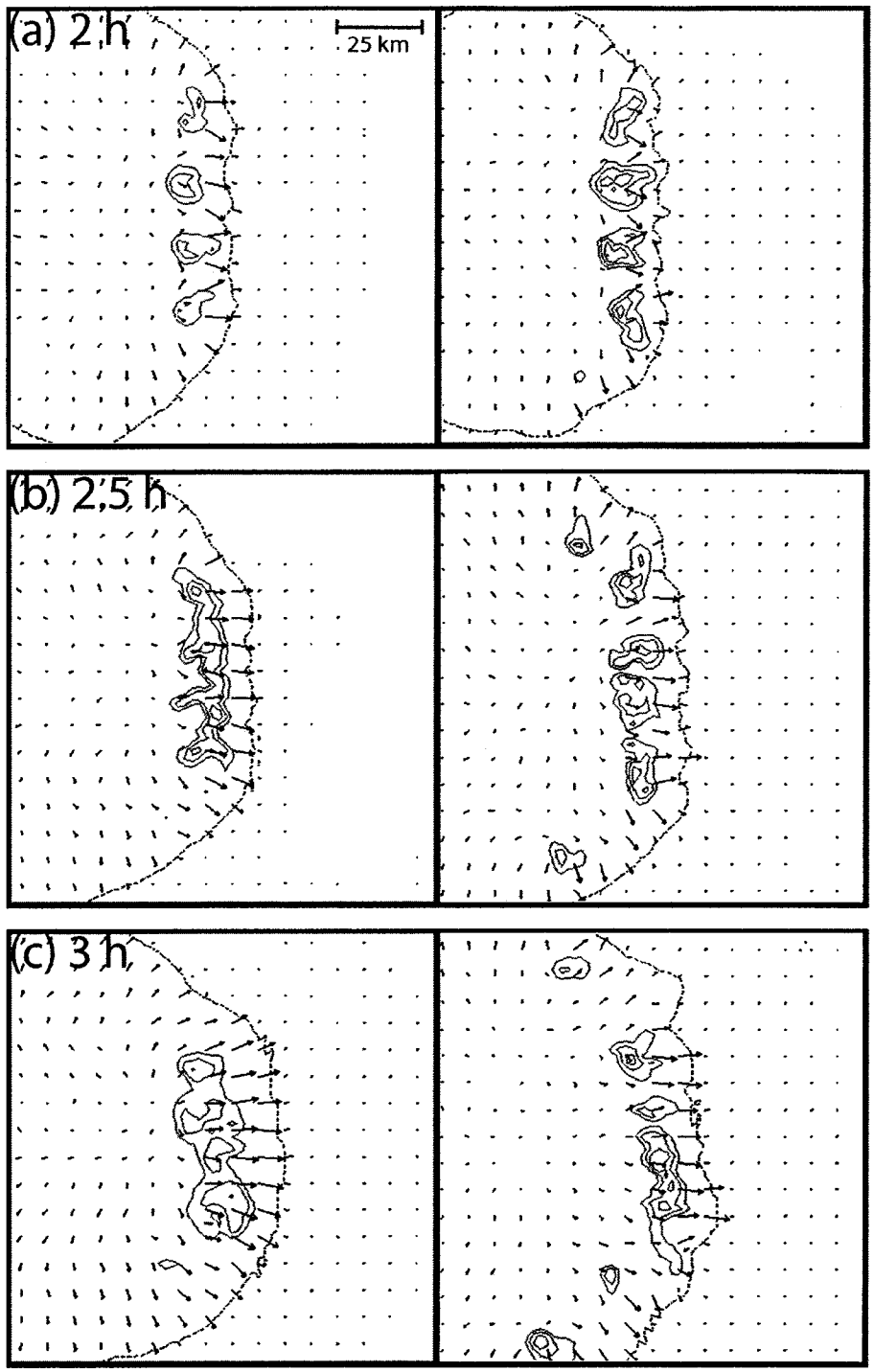


Fig. 5.30a-c. Evolution of the surface total precipitation mixing ratio (solid lines every 2 g kg^{-1} starting at 2 g kg^{-1}) that highlights the heaviest precipitation, the position of the gust front at the surface (dashed line) and the ground relative wind vectors (every 4 grid points) for a 60 km by 60 km portion of the domain at (a) 2 h, (b) 2.5 h, and (c) 3 h for the case with no upper-level shear (left panels) and the case with 15 m s^{-1} of upper-level shear (right panels).

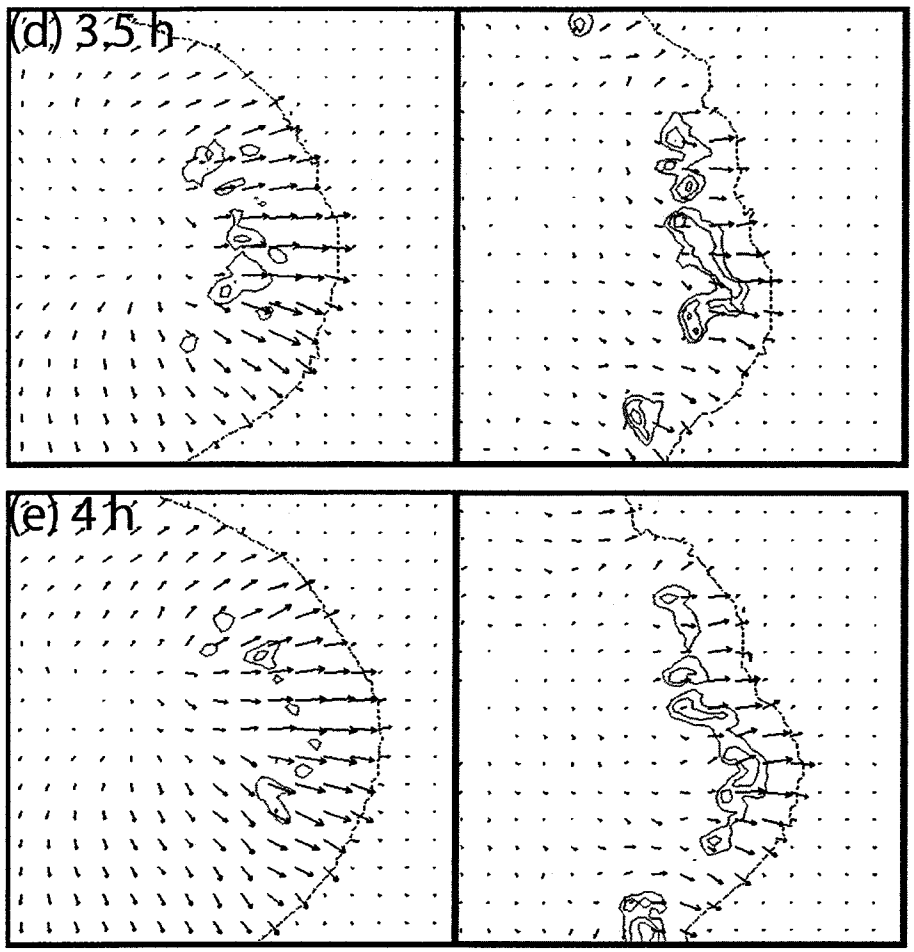


Fig. 5.30 d-e (continued). Evolution of the surface total precipitation mixing ratio (solid lines every 2 g kg^{-1} starting at 2 g kg^{-1}) that highlights the heaviest precipitation, the position of the gust front at the surface (dashed line) and the ground relative wind vectors (every 4 grid points) for a 60 km by 60 km portion of the domain at (d) 3.5 h and (e) 4 h for the case with no upper-level shear (left panels) and the case with 15 m s^{-1} of upper-level shear (right panels).

In contrast, the maximum updrafts remain strong for the cases with upper-level shear throughout the 6 h simulation time (Fig. 5.27). As discussed by WR and as shown later especially for the 30 m s^{-1} shear case (Fig. 5.37), these strong updrafts are partially related to the development of isolated supercell-like structures, but the updrafts along the center portion of the domain shown in Fig. 5.30 are non-supercellular and are significantly stronger than the updrafts along the same portion of the line for the no shear case.

The behavior of the simulations presented in Fig. 5.30 can be explained through an examination of the gust front speeds along with the evolution of the updrafts. As noted earlier, the new updrafts initiated along the cold outflow from the initial cells are slightly stronger for the case with 15 m s^{-1} of shear than for the no shear case. This is apparent in the surface precipitation at 2 h (Fig. 5.30a) and results in a slightly deeper cold pool and a slightly faster gust front motion in the 1.25 h – 2 h period (Fig. 5.31). In the ensuing period of convective cell development (2-2.5 h), the updraft strengths are similar for the no-shear and 15 m s^{-1} shear cases, which produces similar surface precipitation rates (Fig. 5.30b). However, an important difference in the structure of the simulations is seen at 2.5 h. For the no-shear case, the cells form a solid line of heavy precipitation about 50 km in length, whereas for the 15 m s^{-1} shear case, the regions of heavy precipitation are more numerous, but have more separation between them (Fig. 5.30b). As a result of the concentrated region of precipitation in the no shear case, the cold pool becomes deeper and the gust front reaches a speed of 25 m s^{-1} after 3 h (Fig. 5.31). This is accompanied by a surge in the surface wind speeds (Fig. 5.30 c). After the gust front increases in speed, the heavy surface precipitation weakens and becomes located further and further behind the gust front at later times (Fig. 5.30 d-e). In contrast, the surface precipitation remains strong for the 15 m s^{-1} shear case and remains closer behind the gust front through 4 h, which is accompanied by the solidification of the precipitation and the development of a bow echo and a surge in the surface wind speeds (Figs. 5.30 c-e). The gust front reaches a speed of 22.5 m s^{-1} for the 15 m s^{-1} shear case (Fig. 5.31), *but this surge in the gust front is not accompanied by a decrease in the surface precipitation and a weakening of the updrafts.*

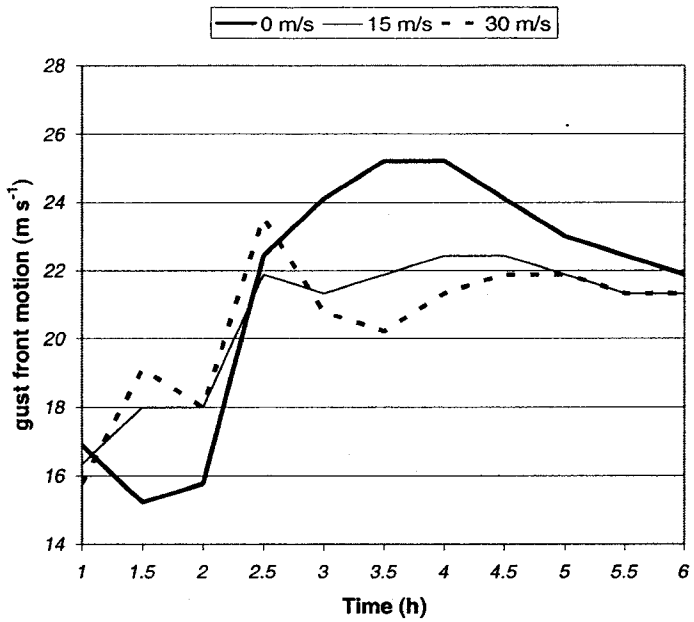


Fig. 5.31. Evolution of the gust front speed for the three simulations.

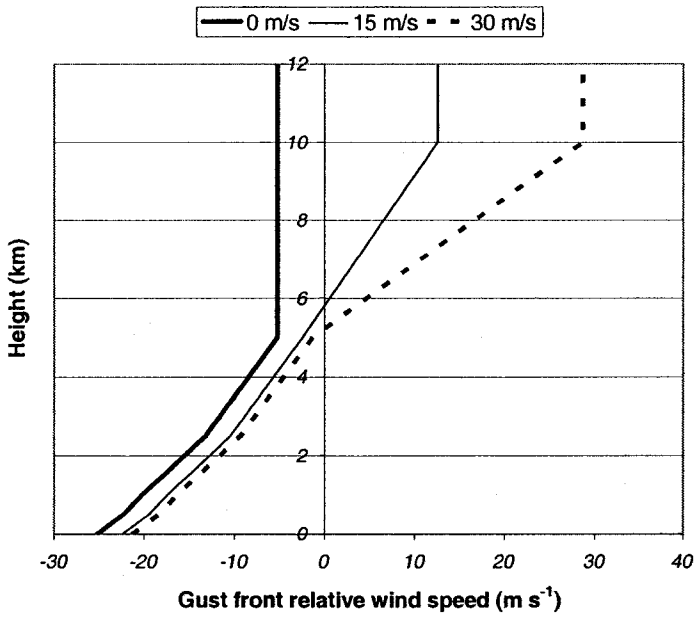


Fig. 5.32. The storm-relative wind profiles for the three simulations at 3.5 h.

The differences in the behavior of the simulations shown in Fig. 5.30 can be understood in the context of the overturning of the updrafts. With the knowledge of the gust front motions, the storm-relative wind profiles show that the case with no upper-level shear transitions to a flow that is rearward at all levels during the time that the

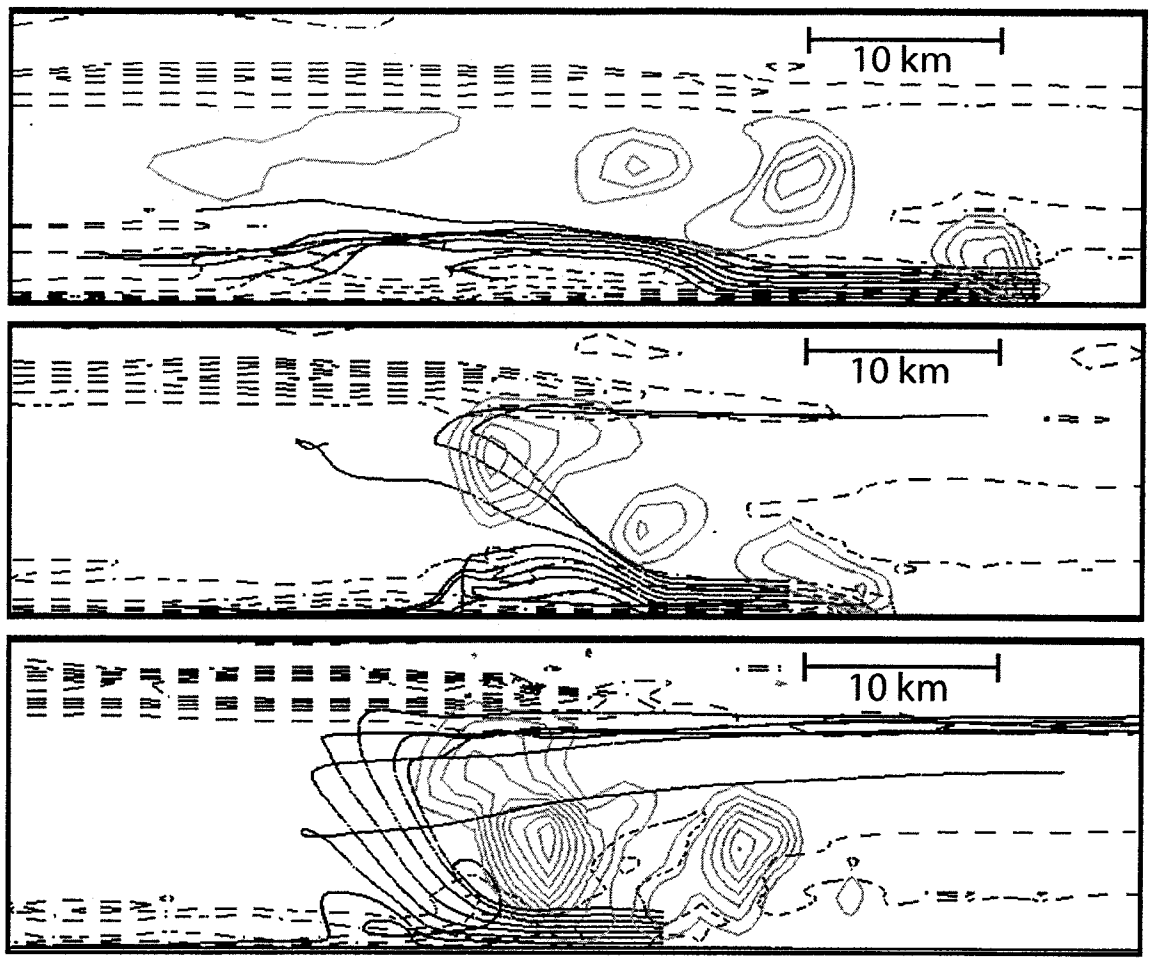


Fig. 5.33. Vertical cross sections taken along the center portion of the cold pool that trigger convections for the case with no upper level shear (top panel), the case with 15 m s^{-1} of upper-level shear (middle panel) and the case with 30 m s^{-1} of upper-level shear (bottom panel). Instantaneous values of negative buoyancy (dashed lines every 0.06 m s^{-2} starting at -0.02 m s^{-2}) and upward motion (grey solid lines every 2 m s^{-1} starting at 2 m s^{-1}) are shown at 4.33 h. The dark solid lines denote the 1 h paths of the trajectories starting at 3.33 h at the lowest 8 model levels (0-2 km). Trajectories are calculated with model output every 2 min.

updrafts and the surface precipitation weakens (Fig. 5.32). However, for the case with 15 m s^{-1} of shear, the storm-relative wind profile still contains an overturning flow with a critical layer near 6 km. Trajectory calculations along cross sections confirm that elevated parcels are overturning in the 15 m s^{-1} case and are responsible for the strong, consolidated updrafts and the subsequent bowing in the heavy precipitation through 4 h (Fig. 5.33) and beyond. The overturning helps to maintain the more upright tilt and the

strength of the convection despite the consolidation of the cells and the surge in the gust front. *This provides evidence that the deeper lifting provided by the upper-level shear contributes to the maintenance of the convection and the tilt of the updrafts in the 3-D simulations.*

Is it interesting that in the 3-D simulations, the upshear tilting of the updrafts for the case with no upper-level shear arises primarily from the increased motion of the cold pool, which creates rearward flow at all levels. In the 2-D simulations, the increased rearward flow resulted entirely from the development of the lowered perturbation pressure underneath the updraft plumes and not from the acceleration of the cold pool. The lowered hydrostatic pressure in midlevels due to the updrafts and the enhanced rearward acceleration also is found in the 3-D simulations (not shown), but the faster acceleration of the cold pool resulting from the concentration of the precipitation in the no-shear case adds to the rearward flow in the 3-D simulations.

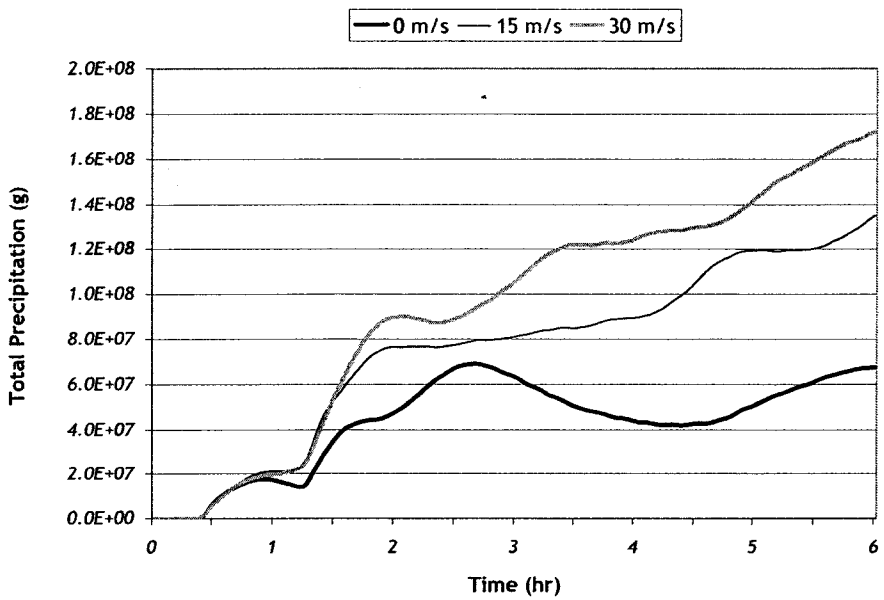


Fig. 5.34. Evolution of the domain-integrated rainwater for the 3-D simulations for the 0, 15 and 30 m s^{-1} simulations..

5.4.3.2 System size

Another interesting difference in the simulations is found when examining the evolution of the integrated rainfall (Fig. 5.34) and presents an additional effect that is only possible in 3-D. The total precipitation produced by the simulations shows a much more pronounced difference among the three simulations than for the 2-D simulations (c.f. Figs. 5.32 and 5.17). Although the convective cells are stronger and produce larger convective rainfall rates when shear is included in upper-levels (Fig. 5.27), the primary reason for this large difference in total rainfall is the differences in the sizes of the systems. Notice that the 15 m s^{-1} case is over twice as large as the case with no upper-level shear by 5 h, with an approximate horizontal length scale of 240 km (Figs. 5.35 and 5.36). The size of the 30 m s^{-1} case is even larger than the 15 m s^{-1} case, with a length scale that expands with time from approximately 150 km at 3 h, to nearly 300 km in length by 6 h (Fig. 5.37). This shows that another effect of the upper-level shear in the 3-D simulations is the enhanced ability of the cold pool to initiate and maintain convection on the outer flanks of the cold pool. It is interesting that cells have difficulty triggering on the northern and southern flanks of the initial convective line for the no shear case, whereas convective cells rapidly fill in along the northern and southern flanks of the cold pool for the cases with upper-level shear. Vertical cross sections along the southern portion of the cold pool reveal that the overturning process appears to be responsible for the convective triggering and maintenance as for the main portions of the convective line. For the no shear case, parcels are lifted as they encounter the rapidly moving ~2 km-deep cold pool but are swept rearward and do not convect because dry air above 3 km (Fig. 5.4) becomes entrained and the parcels quickly become negatively buoyant. However,

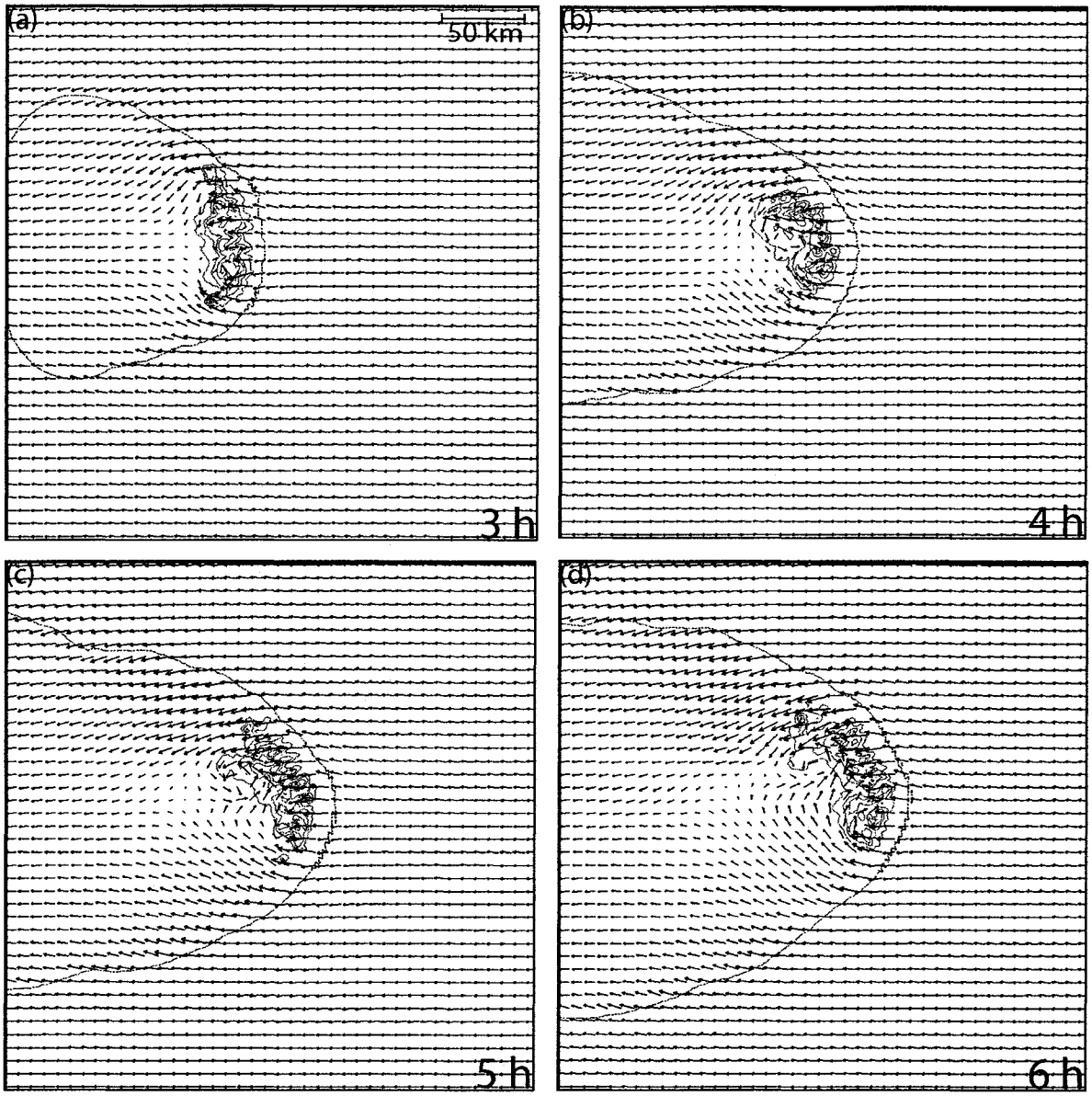


Fig. 5.35. Horizontal cross sections of the total precipitation mixing ratio at 4 km AGL (solid lines contoured every 1 g kg^{-1} starting at 1 g kg^{-1}), the position of the gust front at the surface (dashed line), and the gust-front relative wind at 3 km AGL at every other grid point at (a) 3 h, (b) 4 h, (c) 5 h and (d) 6 h for the case with no upper-level shear. Only a 320 km by 320km portion of the domain is shown.

for the 15 m s^{-1} case the elevated parcels readily convect along the slower moving cold pool and form an overturning circulation with the upward branch close to the leading edge of the gust front. This also is the case for the 30 m s^{-1} simulation (Fig. 5.37), which suggests that the effect of pushing down the cold pool by the perturbation high pressure

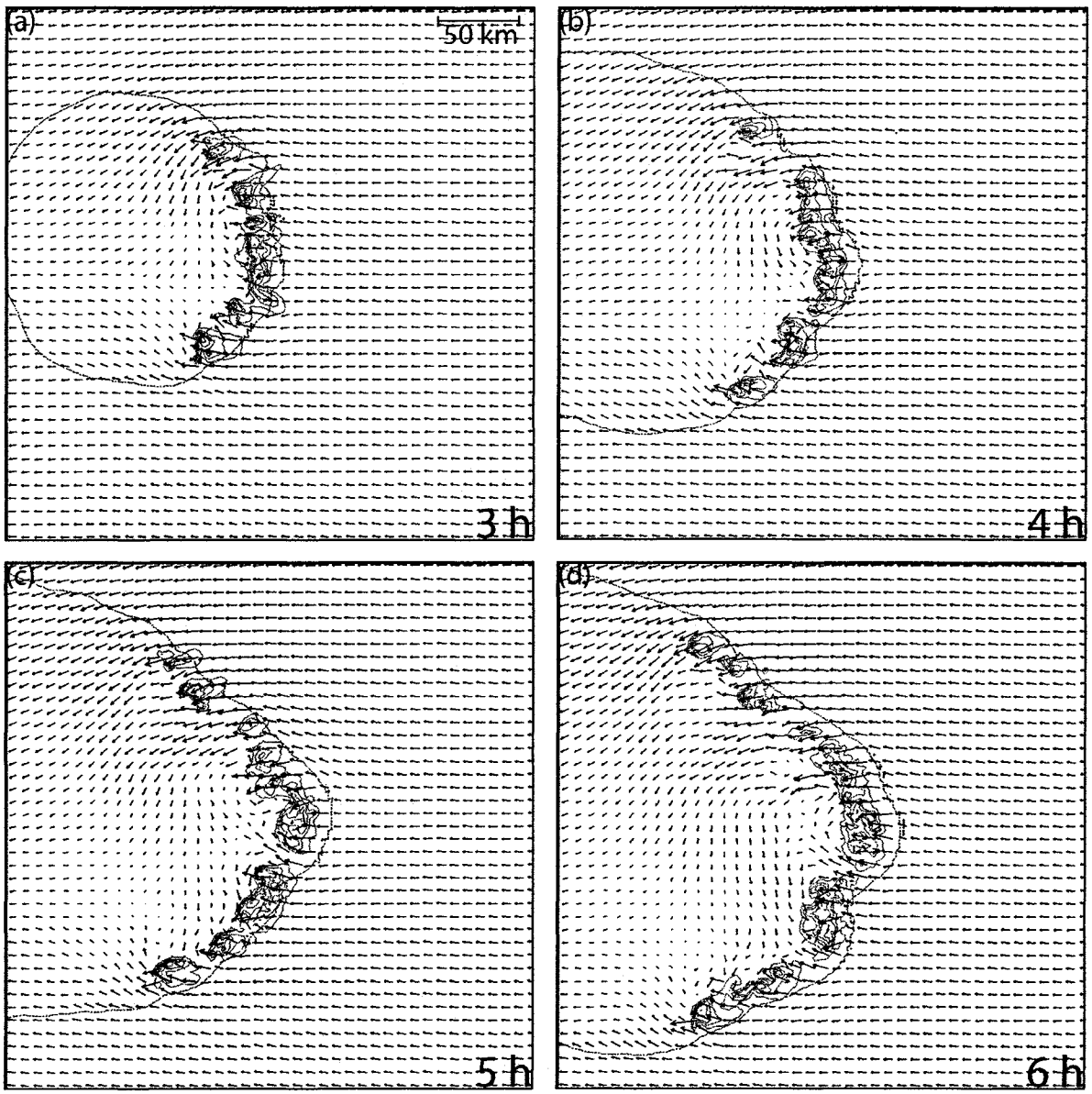


Fig. 5.36. As in Fig. 5.35 but for the case with 15 m s^{-1} of 5-10 km shear.

in the 2-D simulations is not as much as factor in the 3-D simulations for the range of realistic shear magnitudes examined in this study. This is because the leading edge of the cold pool develops along-line variability in three dimensions whose depth is more contingent upon the location and evolution of the cold downdrafts of the convective cells

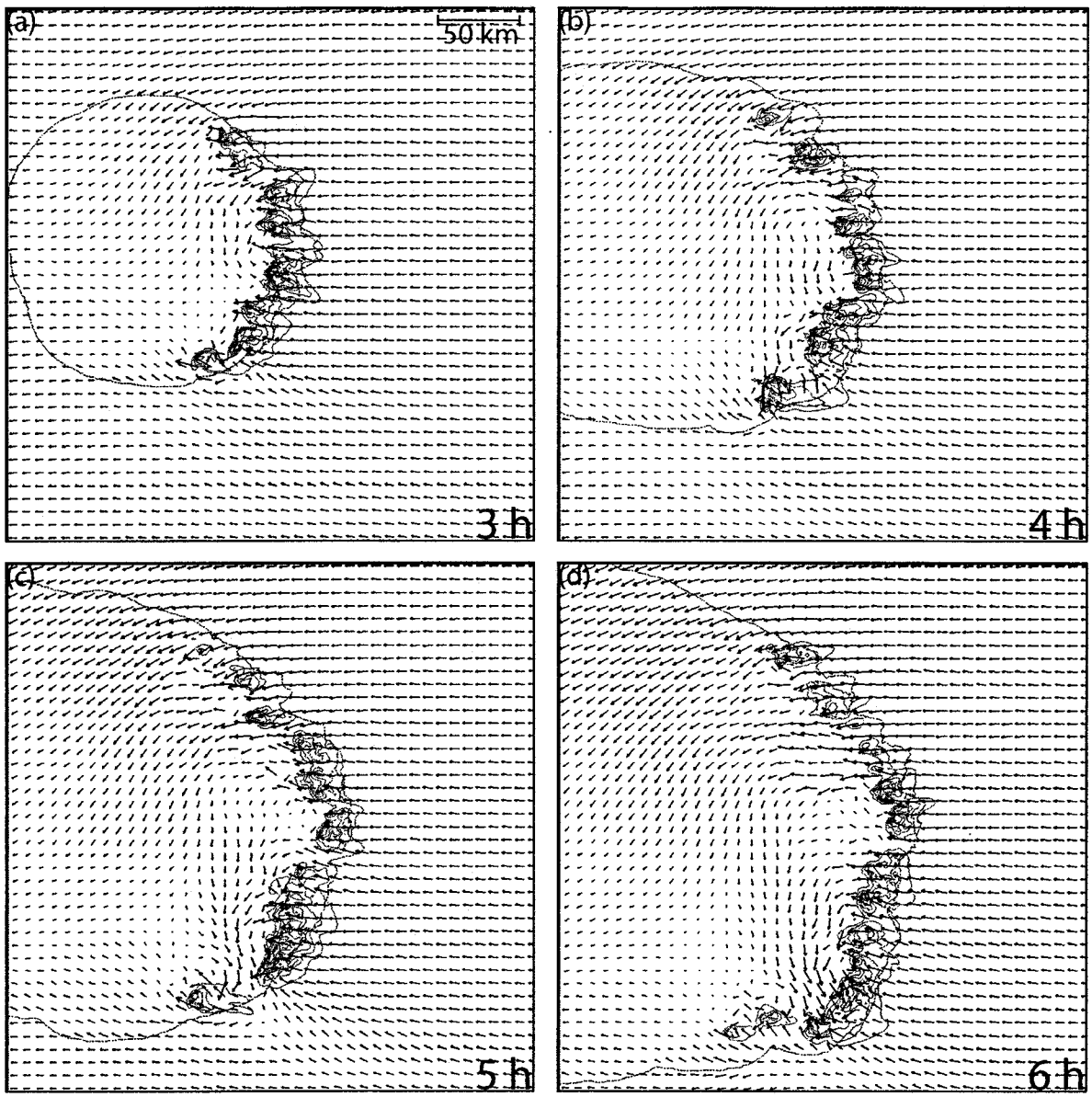


Fig. 5.37. As in Fig. 5.35 but for the case with 30 m s^{-1} of 5-10 km shear.

than the distribution of the perturbation pressure in three dimensions (which also shows along-line variability in 3-D). However, the most important result is the maintenance of the updrafts closer to the gust front and the more abundant convective triggering along the cold pool in the upper-level shear simulations as a result of the overturning process in conjunction with the slower moving cold pool, which suggests that the results of Shapiro

(1992) and Moncrieff and Liu (1999) appear to be a general result for linear MCSs that are forced along propagating cold pools.

5.4.3.3 System structure

It is interesting to discuss some of the differences in the overall structure of the MCSs as compared to past idealized simulations. The case with no upper-level shear at 3 h displays a line of convective cells about 100 km in length located about 10-30 km behind the surface gust front (Fig. 5.35a) that evolves into a broad, bowing MCS on a scale of about 100 km at later times (Figs. 5.35b-d). At 3 h, the midlevel winds reveal relative inflow into the line with anticyclonic and cyclonic vortices at the ends of the line. The cyclonic circulation is in the process of becoming stronger than its anticyclonic counterpart due to the presence of Coriolis forcing (Skamarock et al. 1994). The significant upshear slope to the system is consistent with the development of an expansive stratiform rain region (not shown) and the organized rear inflow into the system, which maintains the strong surface winds, despite the weakening of the updrafts and the precipitation (Fig. 5.26). This type of structure is similar to the type that is presented in W93 and Weisman and Trapp (2003) that develops in the environment with moderate shear confined to low-levels.

In comparison, the case with 15 m s^{-1} of shear displays a line of convective cells about 150 km in length located about 10-15 km behind the surface gust front (Fig. 5.36a). More isolated cells are found on the ends of the line, especially on the southern end where a supercell becomes separated from the main convective line, which is consistent with the simulations in deeper shears presented by W93 and WR. Cyclonic and anticyclonic vortices also are found toward the ends of the line. The cyclonic circulation

becomes stronger with time, as for the case with no shear, but is confined to a smaller horizontal scale. The smaller-scale rear-inflow contributes to the development of the smaller-scale bow echo shown earlier (Fig. 5.32) and is responsible for the surge in surface winds in the 3.5-4 h time period (Fig. 5.26). In the southern portion of the line, another bow echo feature develops from an individual cell at 3 h and surges to the south and east (Fig. 5.36b-c). This bow echo is responsible for the surge in surface winds in the 4.5-5 h time period (Fig. 5.26) and is accompanied by a surge in the gust front (Figs. 5.37c and 5.37d) toward the southeast.

The MCS-scale structure for the 30 m s^{-1} case is similar to the 15 m s^{-1} case in terms of its size and the location of the cells behind the gust front. Consistent with past simulations in very strong deep layer shear (Weisman et al. 1988, WR), the individual convective cells retain their identity for longer periods than for weaker deep layer shear. However, a portion of the line toward the southern half of the system contains a solid line of convective cells that accelerates to the south and east ahead of a region of rear inflow with a significant northerly component that is most apparent at 6 h (Fig. 5.37d).

As mentioned in the background, none of the simulations presented in WR that have shear above 5 km are reported as having organized bow echoes within the main convective line. Therefore, this study presents simulations of MCSs different than what has been reported in the context of idealized numerical simulations in the past within deep shear environments. The simulations presented herein with deep troposphereic shear combine several modes of convective evolution, including bow echoes, over the 6 h simulation time not unlike what is observed with strong MCSs (Pzybylinski 1995, Klimowski et al. 2000, Miller and Johns 2000). It is emphasized the convective

overturning process highlighted in the 2-D simulations appears to have a significant control over the structure and maintenance of the overall MCS in these simulations.

5.5 Discussion

It should be noted that, by examining the effects of upper-level shear on the simulations of strong MCSs, we do not to intend to discount the importance of low-level shear in the environment. Indeed, the observations presented in Chapters 3 and 4 and past numerical modeling work agree that some amount of environmental low-level shear is usually observed in the environment and is needed to simulate convective systems (Thorpe et al. 1982, RKW88). It also is recognized that the character of the lifting and the overall strength and structure of simulated MCSs is clearly sensitive to the magnitude of the low-level shear in past simulations and that we have not examined this sensitivity in the present study. However, the point that we want to emphasize is that the structure and maintenance of strong MCSs also is sensitive to the magnitude of the upper-level shear. While we can not compare the relative sensitivities between the addition of shear in low-levels versus upper-levels, it is shown that even a modest amount of upper-level shear, added to an environment with moderate low-level shear, can have a significant impact on the structure of the systems through the variations in the depth of the overturning updraft. Relatively small changes in the motion of the cold pool of 3-4 m s^{-1} that results from the differing amount of shear, as shown in the previous section, add to these sensitivities by altering the storm-relative wind profiles and the location of the critical level.

It also should be noted that not much has been said about the perceived strength of the systems among the simulations. Overall, the strength of the surface winds showed

less sensitivity to the changes in the upper-level shear than the updraft strength and the overall structure of the systems among the simulations presented here. However, it is found that the perceived strength of the systems is the most sensitive aspect of the simulations to changes in the experimental design, including the horizontal resolution, the initiating mechanism, and the details in the initial profiles and, especially, the parameters in the ice-microphysics scheme. The last point is illustrated in Fig. 5.38, which compares the evolution of the maximum surface winds among simulations, in which the slope-intercept parameter for hail ($n_{x0,}$) is decreased from 4 x 10^6 m^{-4} to a value of 4 x 10^4 m^{-4} and the density of hail (λ_0) is increased from 400 kg m^{-3} to 900 kg m^{-3}. These changes in parameters increase the size of the particles but lower their number concentration (Lin et al. 1983). The surface winds are significantly weaker with these changes for the simulation with no upper-level shear, especially in the 3-4 h time period (Fig. 5.38a). In contrast, the surface winds are significantly stronger at all times after 3 h for a case with 20 m s^{-1} of upper-level shear (Fig. 5.38b); as much as 10 m s^{-1} in the 3-4 h time period and around 5 h. As in the simulations with upper-level shear shown earlier, the surges in strong surface winds are produced by smaller-scale bow echoes that develop along the center portion of the line. These large sensitivities to the perceived strength of the system to details in the model design prevent a general assessment of how the upper-level shear physically affects the strength of the systems. However, the size and structure of the simulations and the tendency for the updrafts to be maintained for environments with positive upper-level shear is not as sensitive to these changes and provides confidence that the behavior of the simulations presented herein is robust.

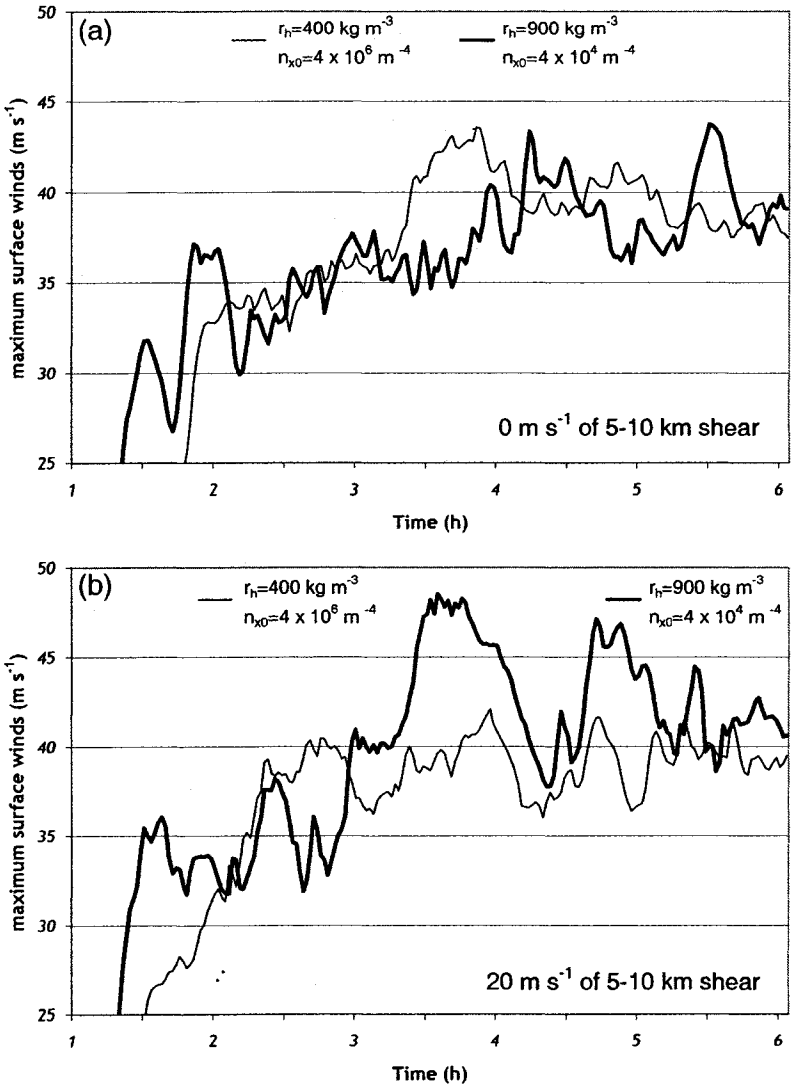


Fig. 5.38. Evolution of the maximum surface winds for specialized simulations that vary the density of hail (r_h) from 400 kg m^{-3} to 900 kg m^{-3} and the slope-intercept parameter for hail (n_{x0}) from 4 x 10^6 m^{-4} to 4 x 10^4 m^{-4} for (a) an environment with no upper-level shear and (b) an environment with 20 m s^{-1} of upper-level shear.

5.6 Application of Results

The previous section emphasizes that the convective overturning process highlighted in the 2-D simulations appears to have a significant control over the development and maintenance of the overall MCS in the 3-D simulations. This result satisfies one of the goals of this study, which is to refine the physical connection between the observed environments and the mechanisms that support strong convective systems,

especially within weakly-forced large scale environments. While the goal of improving the forecasting of strong convective systems is met through the presentation of the environments presented in Chapters 3 and 4, the numerical modeling results also can be used to improving the short-term (< 6 h) forecasting of strong convective systems.

For the application of these concepts to short-term forecasting, an important factor to consider is the motion of the cold pool relative to the deep-tropospheric wind profile. In real world situations, the propagation of the cold pool can be affected by more than the forces responsible for the motion of density currents, including the distribution of conditional instability along the gust front and variations in the low-to mid-level flow relative to the cold pool (Corfidi 2003). Knowledge of all these factors makes the prediction of the cold pool motion difficult prior to MCS initiation. Therefore, the most applicable aspect of the overturning concept may be the prediction of the overall demise of the MCS, which is examined in Gale et al. (2002). Indeed, the mean storm-relative hodographs (Fig. 4.4) show that the critical layer rises from 7 km for the beginning soundings to over 11 km for the decay soundings, which supports the concept of maintaining a deep overturning layer in upper levels to maintain the strength of the overall MCS. Preliminary tests of this concept to predicting the decay of strong convective systems are promising. Even prior to the development of the MCS, a likely range of cold pool speeds can be produced and evaluated. Thus one could develop probabilities for strong, long-lived systems as a function of the predicted cold pool speed and the predicted wind profile.

A point that is emphasized in this study is that the overturning process provides deep lifting for parcels that are elevated above the surface (1-2 km). The overturning of

elevated parcels may provide a concept for how strong convective systems may be maintained after sunset and the development of a nocturnal inversion. The conditional instability present in the residual of the convective boundary layer can persist for several hours after sunset, if not for the duration of the nighttime hours. If the development of the nocturnal inversion is not as strong as to prevent the replenishment and the propagation of the cold pool, the elevated parcels can continue to be lifted and overturn well after dark. It is well known that organized MCSs in the central United States often persist well into the nighttime hours (Fritsch and Forbes 2001). The persistence is often related to the favorable convergence pattern and the advection of heat and moisture by the nocturnal low-level jet and has been related to the presence of dynamically forced lifting by embedded storm-scale circulations (Bernardet and Cotton 1998) and the interaction of a deep stable layer with gravity waves that are favored within deep-tropospheric shear (Schmidt and Cotton 1990) in strong-wind MCS events. The overturning process may provide another conceptual model for the persistence of strong MCSs that have well developed cold pools in situations when it is not obvious that the system is being forced by the nocturnal low-level jet or by other means. To examine this hypothesis, future studies should design numerical simulations that incorporate a nonhomogeneous environment (e.g. Richardson et al. 2000) that includes the development of a nocturnal inversion in the downshear environment.

Chapter 6: Summary and Discussion

This study examines an important subset of strong windstorms produced by mesoscale convective systems known as derechos. Derechos are important because much of the damage caused by non-tornadic wind gusts has been attributed to them. While technological advances in radar observing systems and knowledge of the radar-derived storm-scale characteristics has improved the ability to warn for the potential for damaging winds, derechos remain a difficult forecasting problem at longer lead times (> 3 h). This is related to incomplete knowledge of derecho environments and an incomplete understanding of the physical mechanisms responsible for their development and maintenance.

With the ultimate goal of improving the forecasting of derechos, this study is motivated by past research that suggests a discrepancy between observed derecho environments and the environments that support strong convective systems in idealized numerical simulations. In addition, this study is motivated by past research that suggests upper-level shear is detrimental to the types of convective systems that produce derechos. The goals of this study are to, 1) document the range and structure of large-scale flow patterns associated with derechos from a large data set of events, 2) examine derecho environments in detail using an analysis of proximity soundings, paying particular attention to the vertical distribution of moisture and wind shear and 3) examine the role of upper-level wind shear, which is shown to be present in derecho environments, on the evolution of strong convective systems within 2-D and 3-D idealized numerical simulations. The results from the first portion of this study provide an observational

basis for the initial condition to be used in the numerical modeling experiments. The analysis of the numerical simulations emphasizes how upper-level wind shear (or wind shear above the cold pool) can affect the size and maintenance of the simulated convective systems.

6.1 Summary and discussion of observational analysis

This study finds that there are many types of flow patterns associated with derechos. However, from a semi-objective statistical analysis of a subset of 225 analyses of 500-mb geopotential heights associated with the development and early evolution of DCSs, the majority (72%) of the events can be categorized into three main patterns. The most prominent pattern consists of an upstream trough of varying amplitude (40% of the cases) that contains events from all times of the year and shows a qualitative resemblance to the dynamic pattern defined by Johns (1993). A ridge is defined as the primary large-scale feature in 20% of the cases, all of which are confined to the months of May-August. A zonal-flow pattern is defined in 12% of the cases, which defines an additional warm-season pattern than has not been defined in past literature. The remaining 28% of the cases form large-scale hybrid or unclassifiable patterns that contain various characteristics of the three main patterns. These results should make forecasters aware that derechos can develop under a variety of large-scale flow patterns during all months of the year and that the idealized dynamic and warm-season patterns discussed by Johns (1993) only depict a portion of the full spectrum of the possibilities of large-scale flow patterns associated with the development of DCSs.

An analysis of a large set of proximity soundings shows that DCSs tend to mature as they move into an increasingly moist low-level environment while maintaining relatively

dry conditions at midlevels. In addition, the DCSs tend to decay as they move into an environment with less CAPE and decreasing 0-5-km and 5-10 km shear, but no significant differences in the 0-1 and 0-2.5-km shear (although some of the more weakly-forced events show weaker low-level shear toward decay). Overall, this suggests that mature DCSs can be maintained by the larger-scale circulations that depend on the shear throughout the depth of the troposphere.

The strong-forcing events that typify the upstream-trough pattern show the largest vertical decrease in RH, despite only a modest CAPE and convective instability. The enhancement of downdraft production from this strong vertical RH gradient perhaps explains why derechos can persist within environments of relatively low instability.

A mean, nearly "straight-line" hodograph with shear throughout the depth of the troposphere is common to DCSs that form within all large-scale forcing regimes. The low-level shear is found to be significantly larger for the strong-forcing events (tied to strong low-level jets) than for the more weakly forced events that typify the ridge and zonal-flow patterns. Accordingly, storm-relative hodographs show relative inflow up to about 5 km for the strong-forcing soundings and relative inflow up to almost 9 km for the weak-forcing soundings. These findings add support to Evans and Doswell (2001) who suggest that strong low-level storm-relative inflow may largely impact the strength, mode, and duration of the more weakly forced DCSs.

A comparison of the results to past idealized simulations suggests a discrepancy between observations of severe, long-lived convective systems and the environments required to simulate them in some idealized numerical models. This information is pertinent to forecasters who have real-time proximity sounding information and use

results from the idealized numerical simulations as guidance. Even for the well-defined bow-echo MCSs, the observed low-level shear is usually weaker than what is required to simulate them in idealized models. These results suggest that minimum low-level shear thresholds are not useful for forecasting severe MCS-type structures, including well-defined bow echoes. The observations are more in agreement with the simulations of Weisman (1993) when the 0-5-km shear is considered, suggesting that the deep-layer shear parameters have more utility in forecasting DCSs. This is supported by the fact that substantial shear is often observed in the 5-10-km layer. Overall, this highlights the need to examine DCS simulations within deep shear environments to help reconcile these disparities in observations and idealized models and to provide improved information to forecasters.

6.2 Summary and discussion of the numerical simulations

The overturning of parcels in deep-tropospheric shear described in this study has been identified as a potential contributor to the development of linear MCSs for many years (Thorpe et al. 1982, Shapiro 1992, Moncrieff 1992, Moncrieff and Liu 1999) but has not been detailed within a context of a full set of 2-D and 3-D simulations. For cold pools within an environment of 20 m s^{-1} of bulk shear in the lowest 5 km (matching the median observed low-level shear profile) that move at speeds of 18-20 m s^{-1}, it is found that the addition of weak to moderate shear in the 5-10 km layer allows for the development of an overturning circulation that lifts parcels from the 1-2 km layer to higher levels than any parcels in the lowest 2 km without upper-level shear in the environment. The higher lifting occurs despite the reduction of vertical velocity resulting from the decrease in the head depth of the density current. For 5-10 km bulk shear values

of approximately 3-10 m s^{-1}, the overturning parcels remain close to the leading edge of the gust front, whereas all of the parcels in the low-level inflow for the no shear case are swept rearward as they are forced over the cold pool. In the 2-D simulations, as the upper-level shear becomes stronger (> 10 m s^{-1}), the high perturbation pressure that results from the stagnation region in the flow pushes down the density current head region enough so that the depth of the convergence along the cold pool is small enough to begin a decreasing trend in the vertical displacement of the overturning parcels.

This mechanism maintains the more vertical tilt of squall line simulations in a moist, stratified 2-D environment and translates into higher rainfall production and larger maximum vertical velocities for longer periods than an environment with no upper-level shear. As in the dry 2-D simulations, when the 5-10 km shear is increased to 30 m s^{-1}, the cold pool is shallow and the vertical scale of the overturning is reduced enough to decrease the overall strength of the squall line. In the 3-D simulations, little is mentioned on the relative strengths of the systems because it is found that the surface wind speeds realized in the simulations are particularly sensitive to the details in the numerical design and parameters in the ice-microphysics scheme. However, a robust result is that the overturning process maintains the overall tilt of the system and the updraft strengths and ensures that the main convective cells are maintained closer to the leading edge of the gust front. An additional effect of the overturning in 3-D is to greatly increase the size of the MCS through the combination of the slower cold pool and the overturning that increases the likelihood of convective initiation along the flanks of the cold pool. The systems that develop in upper-level shear are composed of several modes of convection, including organized bow echoes and supercells that occur throughout the 6 h simulation

time, unlike what has been presented in past simulations. Vertical cross sections reveal that the overturning of elevated parcels is responsible for the development of the convection, which qualitatively agrees with the 2-D results.

This concept at work within the 3-D simulations is summarized schematically in Fig. 6.1. In the 1-2 h period, the cells for the 15 m s^{-1} case are collectively stronger and produce slightly more rainfall than the cells for the no-shear case, which leads to a slightly faster cold pool motion for the 15 m s^{-1} case (C_{15}) than for the no-shear case (C_0). From 2-2.5 h, the updrafts strengths and the surface precipitation rates are similar, but the cells for the no-shear case consolidate earlier than for the case with 15 m s^{-1}. This leads to a faster cold pool motion for the no shear case than for the 15 m s^{-1} case at 3-4 h. This leads to a storm-relative wind profile with rearward flow at all levels in the case with no upper-level shear, which results in weaker updrafts and weaker precipitation rates. However, the somewhat slower gust front motion for the case with upper-level shear (C_{15}) helps to maintain a critical layer in mid-upper levels, which maintains the strength of the updrafts and the surface precipitation rates through the overturning of the elevated parcels throughout the 6 h simulation time. The overturning of elevated parcels may provide a concept for how strong convective systems may be maintained after sunset and the development of a nocturnal inversion in situations that are not forced by a nocturnal low-level jet. Additionally, this concept can be applied to the prediction the demise of strong, linear MCSs that have well-developed cold pools, which is supported by the observed storm-relative hodographs presented in Chapter 4.

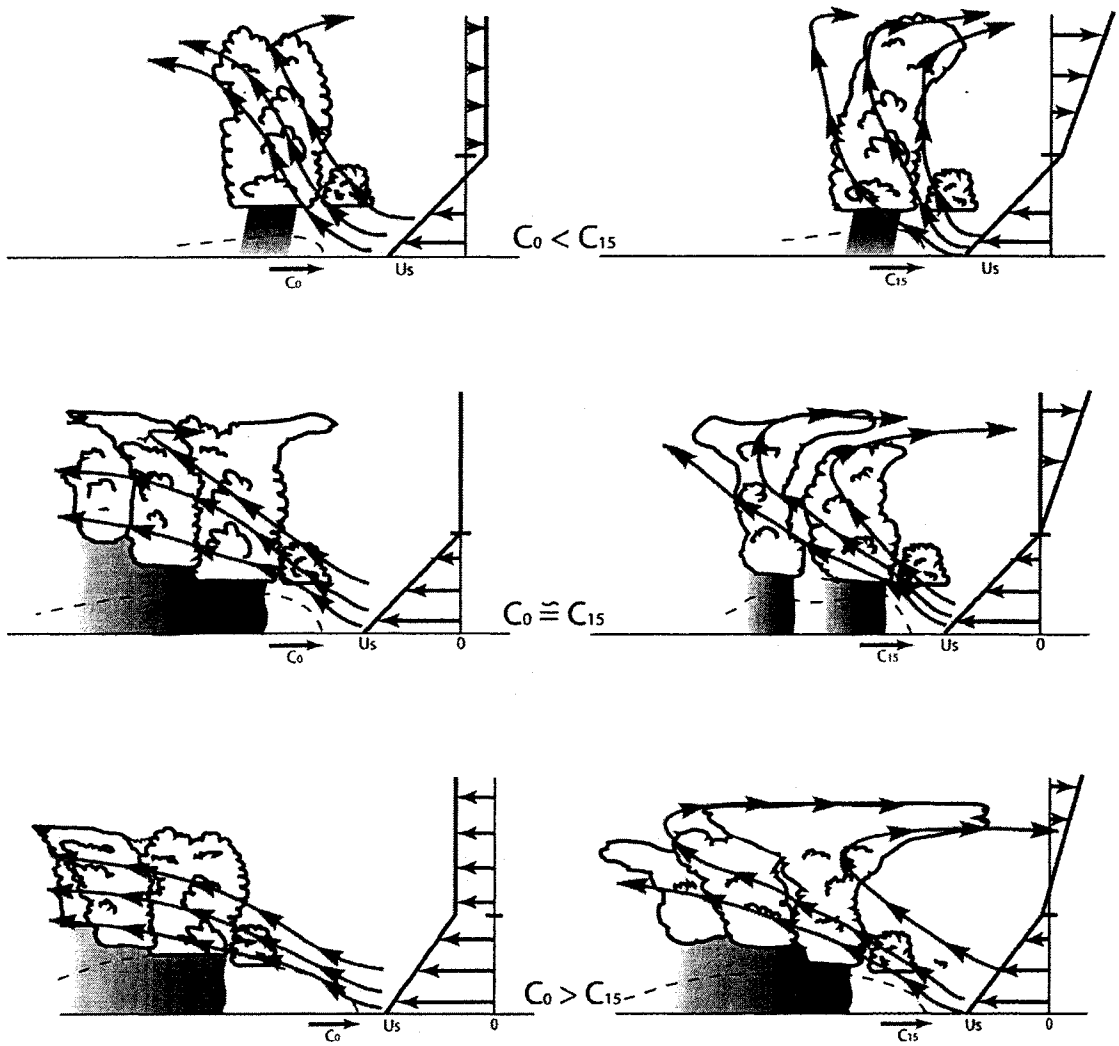


Fig. 6.1. Schematic diagram depicting the relative airflow and the evolution of the convective systems for the case with no upper-level shear (left column) and the case for 15 m s^{-1} of upper-level shear (right column) for the 1-2 h period (top row), the 2-3 h period (middle row), and the 3-4 h period (bottom row). The dashed line represents the cold pool and C_0 and C_{15} represent the cold pool motion for the no shear and 15 m s^{-1} shear cases, respectively. The darkness of the shading represents heavier precipitation rates.

REFERENCES

Atkins, N.T., and R.M. Wakimoto, 1991: Wet microburst activity over the southeastern United States: Implications for forecasting. *Wea. Forecasting*, **6**, 470-482.

Benjamin, J. B., 1968: Gravity current and related phenomena. *J. Fluid Mech.*, **31**, 209–248.

Bentley, M.L., and T.L. Mote, 1998: A climatology of derecho-producing mesoscale convective systems in the central and eastern United States, 1986-1995. Part I: Temporal and spatial distribution. *Bull. Amer. Meteor. Soc.*, **79**, 2527-2540.

--------, and --------, 2000: Reply to "Comments on a climatology of derecho-producing mesoscale convective systems in the central and eastern United States, 1986-1995. Part I: Temporal and spatial distribution". *Bull. Amer. Meteor. Soc.*, **81**, 1055-1060.

--------, and --------, and S.F. Byrd, 2000: A synoptic climatology of derecho producing mesoscale convective systems in the north-central Plains. *Int. J. Climatol.*, **20**, 1329-1349.

Bernardet, L. R., Cotton, W.R. 1998: Multiscale evolution of a derecho-producing mesoscale convective system. *Mon. Wea. Rev.*, **126**, 2991–3015.

Bluestein, H.B., 1993: *Synoptic-Dynamic Meteorology in Mid-Latitudes: Volume II.* Oxford University Press, p 392-407.

Bosart, L. F., Sanders, F. 1981: The johnstown flood of July 1977: A Long-Lived Convective System. *J. Atmos. Sci.*, **38**, 1616–1642.

Bosart, L.F., W.E. Bracken, A. Seimon, J.W. Cannon, K.D. LaPenta, and J.S. Quinlan, 1998: Large-scale conditions associated with the northwesterly flow intense derecho events of 14-15 July 1995 in the northeastern United States. Preprints, *19th Conf. on Severe Local Storms*, Minneapolis, MN, 503-506.

Brandes, Edward A., Ziegler, Conrad L. 1993: Mesoscale downdraft influences on vertical vorticity in a mature mesoscale convective system. *Mon. Wea. Rev.*, **121**, 1337–1353.

Brooks, H.E., C.A. Doswell III, and J. Cooper, 1994: On the environments of tornadic and nontornadic mesocyclones. *Wea. Forecasting*, **9**, 606-618.

Bryan, G.H., and J.M. Fritsch, 2000: The vertical distribution of humidity: A crucial factor in the organization of convection. Preprints, *20th Conf. on Severe Local Storms*, Orlando, FL, Amer. Meteor. Soc., 630-633.

Bryan, G. H., J.C. Wyngaard, and J.M. Fritsch, 2003: Resolution requirements for the simulation of deep moist convection. *Mon. Wea. Rev.*, 131, 2394–2416.

Byers, H.R., and R.R. Braham Jr., 1949: *The thunderstorm*. U.S. Government Printing Office, 287 pp.

Carpenter, R. L., Droegemeier, K. K., Blyth, A. M. 1998: Entrainment and detrainment in numerically simulated cumulus congestus Clouds. Part III: Parcel Analysis. *J. Atmos. Sci.*, **55**, 3440–3455.

Chen, C. 1995: Numerical simulations of gravity currents in uniform shear flows. *Mon. Wea. Rev.*, **123**, 3240–3253.

Coniglio, M.C., and D.J. Stensrud, 2001: Simulation of a progressive derecho using composite initial conditions. *Mon. Wea. Rev.*, **129**, 1593-1616.

Coniglio, M.C. and D.J. Stensrud, 2004: Interpreting the climatology of derechos. *Wea. Forecasting*, **19**, 595-605.

Corfidi, S. F. 2003: Cold Pools and MCS propagation: Forecasting the motion of downwind-developing MCSs. *Wea. Forecasting,* **18**, 997–1017.

Crook, N. A., Moncrieff, M. W. 1988: The effect of large-scale convergence on the generation and maintenance of deep moist convection. *J. Atmos. Sci.*, **45**, 3606–3624.

Davis, C. A., and Weisman, M. L. 1994: Balanced dynamics of mesoscale vortices produced in simulated convective systems. *J. Atmos. Sci.*, **51**, 2005–2030.

DeGaetano, A.T., 1996: Delineation of mesoscale climate zones in the northeastern United States using a novel approach to cluster analysis. *J. Climate*, **9**, 1765-1782.

Davies-Jones, R., 2002: Linear and nonlinear propagation of supercell storms. *J. Atmos Sci,* **59**, 3178–3205.

Davis, C.A., N. Atkins, D. Bartels, L.F. Bosart, M.C. Coniglio, and authors, 2004: The Bow-Echo and MCV experiment (BAMEX): Observations and Opportunities. Manuscript submitted to *Bull. Amer. Meteor. Soc.*

Droegemeier, K. K., Wilhelmson, R. B. 1987: Numerical simulation of thunderstorm outflow dynamics. Part I: Outflow sensitivity experiments and turbulence dynamics. *J. Atmos. Sci.*, **44**, 1180–1210.

Duke, J.W., and J.A. Rogash, 1992: Multiscale review of the development and early evolution of the 9 April 1991 derecho. *Wea. Forecasting*, 7, 623-635.

Evans, J.S., and S.F. Corfidi, 2000: Genesis and evolution of the 4 June 1999 derecho. Preprints, *21st Conf. on Severe Local Storms*, Orlando, FL, 405-408.

Evans, J.S., and C.A. Doswell, 2001: Examination of derecho environments using proximity soundings. *Wea. Forecasting*, **16,** 329-342.

Fankhauser, J.C., G.M. Barnes, and M.A. LeMone, 1992: Structure of a midlatitude squall line formed in strong unidirectional shear. *Mon. Wea. Rev.*, 120, 237–260.

Fovell, R. G., Ogura, Y.. 1989: Effect of vertical wind shear on numerically simulated multicell storm structure. *J. Atmos. Sci.*, **46**, 3144–3176.

Fovell, R.G., and M.Y. Fovell, 1993: Climate zones of the conterminous United States defined using cluster analysis. *J. Climate*, **6**, 2103-2130.

Fritsch, J.M., and G.S. Forbes, 2001: Mesoscale convective systems. *Severe Convective Storms, AMS Meteor. Monogr.*, C. Doswell III, Ed., **28**, Amer. Meteor. Soc., 323-357.

Fujita, T. T., 1955: Results of detailed synoptic studies of squall lines. *Tellus.*, **7**, 405–435.

-------, 1959: Precipitation and cold air production in mesoscale thunderstorm systems. *J. Atmos. Sci.*, **16**, 454–466.

--------, 1978: Manual of downburst identification for Project NIMROD. SMRP Res. Paper 156, University of Chicago, 104 pp.

--------, and R.M.Wakimoto, 1981: Five scales of airflow associated with a series of downbursts on 16 July 1980. *Mon. Wea. Rev.*, **109**, 1438-1456.

Funk, T.W., K.E. Darmofal, J.D. Kirkpatrick, V.L. DeWald, R.W. Prztbylinski, G.K. Schmocker, and Y.J. Lin, 1999: Storm reflectivity and mesocyclone evolution associated with the 15 April 1994 squall line over Kentucky and southern Indiana. *Wea. Forecasting*, **14**, 976-993.

Gale, J.J., W.A. Gallus Jr., and K.A. Jungbluth, 2002: Toward improved prediction of mesoscale convective system dissipation. *Wea. Forecasting*, **17**, 856-872.

Garner, S. J., and A. J. Thorpe, 1992: The development of organized convection in a simplified squall-line model. *Quart J. Roy. Meteor. Soc.*, **118**, 101–124.

Gilmore, M.S., and L.J. Wicker, 1998: The influence of midtropospheric dryness on supercell morphology and evolution. *Mon. Wea. Rev.*, **126**, 943-958.

--------, J.M. Straka, and E.N. Rasmussen, 2004: Precipitation and evolution sensitivity in simulated deep convective storms: Comparisons between liquid only and simple ice liquid phase microphysics. Accepted, *Mon. Wea. Rev.*

Goff, R.C., 1976: Vertical structure of thunderstorm outflows. *Mon. Wea. Rev.*, **104**, 1429-1440.

Gong, X., and M.B. Richman, 1995: On the application of cluster analysis to growing season precipitation data in North America east of the Rockies. *J. Climate*, **8**, 897-931.

Hamilton, R. E., 1970: Use of detailed intensity radar data in mesoscale surface analyses of the 4 July 1969 storm in Ohio. Preprints, *14th Conf. on Radar Meteorology,* Tucson, AZ, Amer. Meteor. Soc., 339–342.

Hane, C. E. 1973: The squall line thunderstorm: Numerical experimentation. *J. Atmos. Sci.,* **30**, 1672–1690.

Heymsfield, A.J., P.N. Johnson, and J.E. Dye, 1978: Observations of moist adiabatic ascent in northeast Colorado cumulus congestus clouds. *J. Atmos. Sci.*, **35**, 1689-1703.

Hinrichs, G., 1888: Tornadoes and derechos. *Amer. Meteor. J.,* **5**, 306–317. 341–349.

Hookings, G.A., 1965: Precipitation-maintained downdrafts. *J. Appl. Meteor.*, **4**, 190-195.

Houze Jr., R.A., S.A. Rutledge, M.I. Biggerstaff, and B.F. Smull, 1989: Interpretation of doppler weather radar displays of midlatitude mesoscale convective systems. *Bull. Amer. Meteor. Soc.*, **70**, 608-619.

Hjelmfelt, M.R., Roberts, R.D., Orville, H.D., Chen, J.P., Kopp, F.J.. 1989: Observational and numerical study of a microburst line-producing storm. *J. Atmos. Sci.,* **46**, 2731–2744.

Johns, R.H., and W.D. Hirt, 1987: Derechos: widespread convectively induced windstorms. *Wea. Forecasting*, **1**, 32-49.

-------, K.W. Howard, and R.A. Maddox, 1990: Conditions associated with long-lived derechos - An examination of the large-scale environment. Preprints, *16th Conf. on Severe Local Storms*, Kananaskis Park, Alberta, Canada, Amer. Meteor. Soc., 408-412.

--------, and C.A. Doswell III, 1992: Severe local storms forecasting. *Wea. Forecasting*, **7**, 588-612.

-------, 1993: Meteorological Conditions associated with bow echo development in convective storms. *Wea. Forecasting*, **8**, 294-299.

-------, and J.S. Evans, 2000: Comments on "A climatology of derecho-producing mesoscale convective systems in the central and eastern United States, 1986-1995. Part I: Temporal and spatial distribution". *Bull. Amer. Meteor. Soc.*, **81**, 1049-1054.

Johnson, R.H., and P.J. Hamilton, 1988: The relationship of surface pressure features to the precipitation and airflow structure of an intense midlatitude squall line. *Mon. Wea. Rev.*, **116**, 1444-1463.

Jorgensen, D. P., and B. F. Smull, 1993: Mesovortex circulations seen by airborne Doppler radar within a bow-echo mesoscale convective system. *Bull. Amer. Meteor. Soc.*, **74**, 2146–2157.

Kamburova, P.L., and F.H. Ludlum, 1966: Rainfall evaporation in thunderstorm downdrafts. *Quart. J. Roy. Meteor. Soc.*, **92**, 510-518.

Kistler, R., E. Kalnay, W. Collins, S. Saha, G. White, J. Woollen, M. Chelliah, W. Ebisuzaki, M. Kanamitsu, V. Kousky, H. van den Dool, R. Jenne, and M. Fiorino, 2001: The NCEP-NCAR 50 year reanalysis: Montly means CD-ROM and documentation. *Bull. Amer. Meteor. Soc.*, **82**, 247-267.

Klemp, J. B., and R. B. Wilhelmson, 1978: The simulation of three-dimensional convective storm dynamics. *J. Atmos. Sci.*, **35**, 1070–1096.

Klimowski, B. A. 1994: Initiation and development of rear inflow within the 28-29 June 1989 North Dakota mesoconvective system. *Mon. Wea. Rev.*, **122**, 765–779.

--------, R. Przybylinski, G. Schmocker, M.R. Hjelmfelt, 2000: Observations of the formation and early evolution of bow echoes. Preprints, *20th Conf. on Severe Local Storms*, Orlando, FL, Amer. Meteor. Soc., 44-47.

--------, Bunkers, M. J., Hjelmfelt, M. R., Covert, J. N. 2003: Severe convective windstorms over the northern high plains of the United States. *Wea. Forecasting*, **18**, 502–519.

Knupp, K. R. 1987: Downdrafts within high plains cumulonimbi. Part I: General kinematic structure. *J. Atmos. Sci.*, **44**, 987–1008.

--------, 1988: Downdrafts within high plains cumulonimbi. Part II: Dynamics and thermodynamics. *J. Atmos. Sci.*, **45**, 3965-3982.

--------, 1989: Numerical simulation of low-level downdraft initiation within precipitating cumulonimbi: Some preliminary results. *Mon. Wea. Rev.*, **117**, 1517–1529.

--------, 1996: Structure and evolution of a long-lived, microburst-producing storm. *Mon. Wea.r Rev.* **124**, 2785–2806.

Kunkel, K.E., R.A. Pielke, and S.A. Changnon, 1999: Temporal fluctuations in weather and climate extremes that couse economic and human health impacts: A review. *Bull. Amer. Meteor. Soc.*, **80**, 1077-1098.

LeMone, M. A. 1983: Momentum transport by a line of cumulonimbus. *J. Atmos Sci.*, **40**, 1815–1834.

LeMone, M. A., Barnes, G. M., Zipser, E. J. 1984: Momentum flux by lines of cumulonimbus over the tropical oceans. *J. Atmos Sci.*, **41**, 1914–1932.

Lilly, D.K., 1979: The dynamical structure and evolution of thunderstorms and squall lines. *Ann. Rev. Earth Planet Sci.*, **7**, 117-171.

Lin, Y., Farley, R. D., Orville, H. D. 1983: Bulk parameterization of the snow field in a cloud model. *J. of Appl. Meteor.*, **22**, 1065–1092.

Liu, C., Moncrieff, M. W. 1996: A numerical study of the effects of ambient flow and shear on density currents. *Mon. Wea. Rev.*, **124**, 2282–2303.

Ludlum, F.H., 1963: Severe local storms: A review. *Meteor. Monogr.*, **5**, Amer. Meteor. Soc., 1-30.

Maddox, R.A., 1980: Mesoscale convective complexes. *Bull. Amer. Meteor. Soc.*, **61**, 1374-1387.

Martinelli, J.T., R.W. Przybylinski, and Y.J. Lin, 2000: Observational study of a midwestern severe wind mesoscale convective system (MCS) on 29 June 1998: A single doppler analysis study. Preprints, *20th conf. on Severe Local Storms*, Orlando, FL, Amer. Meteor. Soc., 382-385.

Miller, D.J., R.H. Johns, 2000: A detailed look at extreme wind damage in derecho events. Preprints, *20th Conf. on Severe Local Storms*, Orlando, FL, Amer. Meteor. Soc., 52-55.

--------, D.L. Andra, Jr., and, J.S. Evans, 2002: Observations of the 27 May 2001 high-end derecho event in Oklahoma. Preprints, *21st Conf. on Severe Local Storms*, San Antonio, TX, Amer. Meteor. Soc., 13-16.

Moncrieff, M.W., 1978: The dynamical structure of two-dimensional steady convection in constant vertical shear. *Quart. J. Roy. Meteor. Soc.*, **104**, 543-567.

--------, 1992: Organized convective systems: Archetypal dynamical models, mass and momentum flux theory, and parameterization. *Quart. J. Roy. Meteor. Soc.*, **118**, 819-850.

--------, and C. Liu, 1999: Convection initiation by density currents: Role of convergence, shear, and dynamical organization. *Mon. Wea. Rev.*, **127**, 2455-2464.

Newton, 1966: Circluations in large sheared cumulonimbus. *Tellus*, **18**, 699-713.

Nolan, R.H., 1959: A radar pattern associated with tornadoes. *Bull. Amer. Meteor. Soc.*, **40**, 277-279.

Parker, M.D., and R.H. Johnson, 2000: Organizational modes of midlatitude mesoscale convective systems. *Mon. Wea. Rev.*, **128**, 3413-3436.

Proctor, F.H., 1989: Numerical simulation of an isolated microburst. Part II: Sensitivity experiments. *J. Atmos. Sci.*, **46**, 2143-2165.

Przybylinski, R.W., 1995: The bow echo: Observations, numerical simulations, and severe weather detection methods. *Wea. Forecasting*, **10**, 203-218.

Richardson, Y.P., K.K. Droegemeier, and R.P. Davies-Jones, 2000: The influence of horizontal variations in vertical shear and low-level moisture on numerically simulated convective storms. Preprints, *20th Conf. on Severe Local Storms*, Orlando, FL, Amer. Meteor. Soc., 599-603.

Rotunno, R., and J.B. Klemp, 1985: On the rotation and propagation of simulated supercell thunderstorms. *Mon. Wea. Rev.*, **110**, 136-151.

--------, J.B. Klemp, and M.W. Weisman, 1988: A theory for strong, long-lived squall lines. *J. Atmos. Sci.*, **45**, 463-485.

Rutledge, S. A., Hobbs, P. V. 1984: The mesoscale and microscale structure and organization of clouds and precipitation in midlatitude cyclones. XII: A diagnostic modeling study of precipitation development in narrow cold-frontal rainbands. *J. Atmos. Sci.*, **41**, 2949–2972.

Schmidt, J.M., and W.R. Cotton, 1989: A high plains squall line associated with severe surface winds. *J. Atmos. Sci.*, **46**, 281-302.

--------, and --------, 1990: Interactions between upper and lower tropospheric gravity waves on squall line structure and maintenance. *J. Atmos. Sci.*, **47**, 1205-1222.

Seibert, P., 1993: Convergence and accuracy of numerical methods for trajectory calculations. *J. of Appl. Meteor.*, **32**, 558–566.

Seitter, K. L., 1986: A numerical study of atmospheric density current motion including the effects of condensation. *J. Atmos. Sci.*, **43**, 3068–3076.

Shapiro, A., 1992: A hydrodynamical model of shear flow over semi-infinite barriers with application to density currents. *J. Atmos. Sci.*, **49**, 2293-2305.

Skamarock, W. C., M. L. Weisman, and J. B. Klemp, 1994: Three-dimensional evolution of simulated long-lived squall lines. *J. Atmos. Sci.*, **51**, 2563–2584.

Smull, B. R., and R. A. Houze Jr., 1987: Rear inflow in squall lines with trailing stratiform precipitation. *Mon. Wea. Rev.*, **115**, 2869–2889.

Soong, S., Ogura, Y., 1973: A comparison between axisymmetric and slab-symmetric cumulus cloud models. *J. Atmos. Sci.*, **30**, 879–893.

Spoden, P.J., C.N. Jones, J. Keysor, and M. Lamm, 1998: Observations of flow structure and mesoscale circulations associated with the 5 May 1996 asymmetric derecho in the lower Ohio valley. Preprints, *19th Conf. on Severe Local Storms*, Minneapolis, MN, Amer. Meteor. Soc., 514-517.

Srivastava, R.C., 1985: A simple model of evaporatively driven downdraft: Application to microburst downdraft. *J. Atmos. Sci.*, **42**, 1004-1023.

Staniforth, A., Côté, J., 1991: Semi-lagrangian integration schemes for atmospheric models—A review. *Mon.y Wea.r Rev.*, **119**, 2206–2223.

Stensrud, D. J., Maddox, R. A., Ziegler, C. L. 1991: A sublimation-initiated mesoscale downdraft and its relation to the wind field below a precipitating anvil cloud. *Mon. Wea. Rev.*, **119**, 2124–2139.

Straka, J. M., Anderson, J. R. 1993: Numerical simulations of microburst-producing storms: some results from storms observed during COHMEX. *J. of the Atmos. Sci.*, **50**, 1329–1348.

Thorpe, A. J., M. J. Miller, and M. W. Moncrieff, 1982: Two-dimensional convection in non-constant shear: A model of mid-latitude squall lines. *Quart. J. Roy. Meteor. Soc.*, **108**, 739–760.

Trapp, R. J., Weisman, M. L. 2003: Low-level mesovortices within squall lines and bow echoes. part ii: their genesis and implications. *Mon. Wea.r Rev.*, **131**, 2804–2823.

Trier, S. B., LeMone, M. A., Skamarock, W. C. 1998: Effect of three-dimensional structure on the stormwide horizontal accelerations and momentum budget of a simulated squall line. *Mon. Wea. Rev.*, **126**, 2580–2598.

Uccellini, L.W., 1980: On the role of upper tropospheric jet streaks and leeside cyclogenesis in the development of low-level jets in the Great Plains. *Mon. Wea. Rev.*, 108, 1689–1696.

--------, and D.R. Johnson, 1979: The coupling of upper and lower tropospheric jet streaks and implications for the development of severe convective storms. *Mon. Wea. Rev.*, **107**, 682-703.

Wakimoto, R.M., 1982: The life cycle of thunderstorm gust fronts as viewed with Doppler radar and rawinsonde data. *Mon. Wea. Rev.*, **110**, 1060-1082.

--------, 2001: Convectively driven high wind events. *Severe Convective Storms, AMS Meteor. Monogr.*, C. Doswell III, Ed., **28**, Amer. Meteor. Soc., 255-298.

--------, and Bringi, V.N.. 1988: Dual-polarization observations of microbursts associated with intense convection: The 20 July storm during the MIST project. *Mon. Wea. Rev.*, **116**, 1521–1539.

Walter, K., 1987: The southern oscillation in surface circulation and climate over the tropical Atlantic, eastern Pacific, and Indian oceans as captured by cluster analysis. *J. Clim. Appl. Meteor.*, **26**, 541-558.

Weisman, M.L., 1992: The role of convectively generated rear-inflow jets in the evolution of long-lived mesoconvective systems. J. Atmos. Sci., **49**, 1826-1847.

--------, 1993: The genesis of severe, long-lived bow echoes. *J. Atmos. Sci.*, **50**, 645-670.

--------, 2001: Bow echoes: A tribute to T.T. Fujita. *Bull. Amer. Meteor. Soc.*, **82**, 97-116.

--------, and J.B. Klemp, 1982: The dependence of numerically simulated convective storms on vertical wind shear and buoyancy. *Mon. Wea. Rev.*, **110**, 504-520.

——, and Davis, C. A., 1998: Mechanisms for the generation of mesoscale vorticies within quasi-linear convective systems. *J. Atmos. Sci.*, **55**, 2603–2622.

--------, Trapp, R. J. 2003: Low-level mesovortices within squall lines and bow echoes. Part I: Overview and dependence on environmental shear. *Mon. Wea. Rev.*, **131**, 2779–2803.

--------, and R. Rotunno, 2004: 'A theory for strong, long-lived squall lines' revisited. *J. Atmos. Sci.*, **61**, 361-382.

——, Klemp, J. B., and R. Rotunno, 1988: Structure and evolution of numerically simulated squall lines. *J. Atmos. Sci.*, **45**, 1990–2013.

--------., Skamarock, W. C., Klemp, J. B. 1997: The resolution dependence of explicitly modeled convective systems. *Mon. Wea,r Rev.*, **125**, 527–548.

Weiss, S.J., J.A. Hart, and P.R. Janish, 2002: An examination of severe thunderstorm wind report climatology: 1970-1999. Preprints, 21st Conf. Severe Local Storms, San Antonio, TX, Amer. Meteor. Soc., 446-449.

Wicker, L.W., 1996: The role of near surface wind shear on low-level mesocyclone generation and tornadoes. Preprints, *18th Conf. on Severe Local Storms*, San Francisco, CA, Amer. Meteor. Soc., 115-119.

--------, and Wilhelmson, R. B. 1995: Simulation and analysis of tornado development and decay within a three-dimensional supercell thunderstorm. *J. Atmos. Sci.*, **52**, 2675–2704.

--------, and --------, 2002: Time-splitting methods for elastic models using forward time schemes. *Mon. Wea. Rev.*, **130**, 2088–2097.

Wilks, D.S., 1995: *Statistical methods in the atmospheric sciences.* Academic Press, p 419-428.

Wilson, J. W., and Wakimoto, R. M. 2001: The discovery of the downburst: T. T. Fujita's contribution. *Bull. Amer. Meteor. Soc.*, **82**, 49–62.

Xu, Q., 1992: Density Currents in shear flows-a two-fluid model. *J. Atmos. Sci.*, **49**, 511–524.

Xu, Q., Moncrieff, M. W. 1994: Density current circulations in shear flows. *J. Atmos. Sci.*, **51**, 434–446.

Xue, M., 2000: Density currents in two-layer shear flows. *Quart. J. Roy. Atmos. Sci.*, **126**, 1301–1320.

--------, Xu, Q., Droegemeier, K. K. 1997: A theoretical and numerical study of density currents in nonconstant shear flows. *J. Atmos.c Sci.*, **54**, 1998–2019.

Yang, M., Houze, R. A. 1995: Sensitivity of squall-line rear inflow to ice microphysics and environmental humidity. *Mon. Wea. Rev.* **123**, 3175–3193.

--------, 1996: Momentum budget of a squall line with trailing stratiform precipitation: calculations with a high-resolution numerical model. *J. Atmos. Sci.*, **53**, 3629–3652.

Zipser, E.J., 1982: Use of a conceptual model of the life cycle of mesoscale convective systems to improve very-short-range forecasts. *Nowcasting*, K. Browning, Ed., Academic Press, 191-221.

APPENDIX

Parameters used to construct the idealized sounding:

v at all levels	0 m s^{-1}
u at lowest model level	0 m s^{-1}
u at 0.5 km	3 m s^{-1}
u at 1 km	5 m s^{-1}
u at 2.5 km	12 m s^{-1}
u at 5 km	20 m s^{-1}
u at the highest model level	10 m s^{-1}
Initial lifting condensation level (LCL)	1530 m
θ at the surface	303.16 K
p at the surface	1000 h Pa
surface to LCL temperature lapse rate	-8.8 K km^{-1}
LCL to 6 km temperature lapse rate	-6.5 K km^{-1}
6 km to 12 km temperature lapse rate	-7.0 K km^{-1}
relative humidity at the LCL	93%
relative humidity between LCL and 2500 m	93%
relative humidity at 3000 m	40%
relative humidity at 7 km	50%
relative humidity at 12 km and above	40%

Key parameters used in the 3-D simulations:

Horizontal domain length	400000 m
Vertical domain height	16000 m
Horizontal grid point spacing	2000 m
Vertical grid point spacing below 1250 m	250 m
Large time step	6 s
Small time step	1 s
u grid motion	18 m s^{-1}
Maximum θ' in warm bubbles	2 K
Number of warm bubbles	5
x-radius of each warm bubble	10000 m
y-radius of each warm bubble	10000 m
z-radius of each warm bubble	1500 m
x-center of warm bubbles	200000 m
y-center of warm bubbles	230000 m
z-center of warm bubbles	1500 m
Coriolis parameter	10^{-4} s^{-1}
Height to begin vertical Rayleigh damper	13500 m
Vertical Rayleigh damper magnitude	0.001
Slope intercept parameter for rain	8.0×10^{-6} m^{-4}
Slope intercept parameter for snow	3.0×10^{-6} m^{-4}
Slope intercept parameter for hail/graupel	4.0×10^{-6} m^{-4}
Density of snow	100 kg m^{-3}
Density of hail/graupel	400 kg m^{-3}